LUND UNIVERSITY

Antenna Analysis and Design Using Stored Energies and Physical Limitations

Cismasu, Marius

2014

[Link to publication](#)

Total number of authors:
1

LUND UNIVERSITY

PO Box 117
221 00 Lund
+46 46-222 00 00

Antenna Analysis and Design Using Stored Energies and Physical Limitations

Marius Cismasu

Doctoral Dissertation
Electromagnetic Theory

Lund University
Lund, Sweden
2014

Doctoral dissertation which, by due permission of the Faculty of Engineering, Lund University, will be publicly defended on October 27, 2014, at 10.15 a.m. in lecture hall E:1406, Ole Römers väg 3, Lund, for the degree of Doctor of Philosophy in Engineering.

Abstract

A method to estimate Q and $Q_{Z'}$ of antennas from single-frequency current distributions is described. This single-frequency method and the concepts of physical bounds on antenna parameters and optimum current distributions are applied to different analysis and design situations of two-dimensional and three-dimensional radiating structures (*i.e.*, antennas). The situations considered are: antenna optimization using a genetic algorithm and the single-frequency Q computation for single or multi-band operation, antenna placement optimization in a wireless device using physical bounds, and antenna optimization that includes $Q_{Z'}$ in the objective function. Antenna performance is compared with physical bounds or optimum-current performance in the situations studied.

The results presented in this thesis suggest that single-frequency methods may reduce the time necessary to optimize automatically, *e.g.*, using a computer, some antenna parameters such as bandwidth. Furthermore, physical bounds and optimum current distributions are tools that provide valuable information for the processes of antenna analysis and design.

Populärvetenskaplig sammanfattning

Antenner finns idag nästan överallt: i mobiltelefoner, bärbara datorer, surfplattor, kameror, skrivare, klockor och armbandsur, o.s.v. De används för att överföra information trådlöst mellan enheter med hjälp av elektromagnetiska vågor (som har egenskapen att utbreda sig, ungefär på samma sätt som vågorna rör sig på en vattenyta när man kastar en liten sten).

Ju mer avancerad teknologin blir, desto hårdare krav ställs på antenndesignen. I det här sammanhanget föreslår denna avhandling en metod som kan användas för att förbättra antenndesignprocessen. Den här metoden kan användas för att få antenner som uppfyller kraven snabbare. Den kan också användas som hjälpverktyg för antennkonstruktören som, med hjälp av datorn, designar antenner.

I antenndesign är det ibland viktigt att veta fysikaliska begränsningarna som gäller för det analyserade problemet. I den här avhandlingen används fysikaliska begränsningar härledda från optimala strömsfördelningar för antenndesign och -analys.

Preface

This doctoral dissertation in Engineering summarizes the research I have carried out at the Department of Electrical and Information Technology, Lund University, Sweden. The first part consists of a General Introduction followed by the scientific papers as listed below.

List of included papers

I. M. Cismasu and M. Gustafsson,
"Antenna Bandwidth Optimization with Single Frequency Simulation"
IEEE Transactions on Antennas and Propagation, Vol. 62, No. 3, pp. 1304-1311, 2014
Contributions of the author: The author of this thesis is the main contributor to this paper. He has setup all simulations involved, obtained the results, and written the paper. The work has been carried out under the supervision of the second author.

II. M. Cismasu and M. Gustafsson,
"Multiband Antenna Q Optimization using Stored Energy Expressions"
IEEE Antennas and Wireless Propagation Letters, Vol. 13, No. 2014, pp. 646-649, 2014
Contributions of the author: The author of this thesis is the main contributor to this paper. He has setup all simulations involved, obtained the results, and written the paper. The work has been carried out under the supervision of the second author.

III. M. Cismasu, D. Tayli, and M. Gustafsson,
"Stored Energy Based 3D Antenna Analysis and Design"
Submitted to: *IEEE Transactions on Antennas and Propagation*, 2014
Contributions of the author: The author of this thesis is the main contributor to this paper. He has setup all simulations involved, obtained the results, and written the paper. The work has been carried out under the supervision of the third author.

IV. M. Gustafsson, M. Cismasu and B.L.G. Jonsson,
"Physical bounds and optimal currents on antennas"
IEEE Transactions on Antennas and Propagation, Vol. 60, No. 6, pp. 2672-2681, 2012
Contributions of the author: The author of this thesis has derived the numerical results for practical antennas, and those used to illustrate the negative stored electric energy.

V. M. Gustafsson, M. Cismasu and S. Nordebo,
"Absorption Efficiency and Physical Bounds on Antennas"

Contributions of the author: The author of this thesis has obtained the numerical results included in the paper and written the section presenting those results.

Acknowledgments

First and foremost, I would like to express my deepest gratitude to my supervisors Prof. Mats Gustafsson and Prof. Gerhard Kristensson for offering me the chance of a wonderful learning and scientific journey. I am particularly grateful for their patience, time, knowledge, guidance and all the rest they provided. Their positive thinking and enthusiasm helped me along the way.

I would also like to thank my wife Ana and cousin Mikaela for supporting and believing in me. My parents and brother are not forgotten for all the things they have done and will do for me throughout their lives; these things have helped me on my way.

I am grateful to the personnel at the department for the support they always provided.

I am thankful to my fellow PhD student colleagues and the rest of the department personnel for providing a pleasant work environment.

Lund, September 2014

Marius Cismasu

---

[1]MNW Scan, Singapore, http://www.mnw-scan.com/ — BetaMatch, Software for antenna component matching.

Acronyms and Abbreviations

2D two-dimensional

3D three-dimensional

AR antenna region

EFIE electric field integral equation

EM electromagnetic

FBW fractional bandwidth

GA genetic algorithm

MATLAB® matrix laboratory; registered trademark of The MathWorks, Inc.

MoM method of moments

PEC perfect electrical conductor

PIFA planar inverted-F antenna

RLC/RCL resistor-inductor-capacitor

SMD surface-mount device

TE transverse electric

TM transverse magnetic

UWB ultra wideband

Contents

V   Absorption Efficiency and Physical Bounds on Antennas   135

Research Overview

Marius Cismasu

1 Motivation

Antennas are vital parts of wireless communication devices. These devices have various sizes, forms and specifications, such that more or less stringent constraints act on the antennas integrated in devices. Antenna analysis and design tools and methods aim at finding solutions to such constraints. These solutions have, in their turn, different forms. They may be improvements of the design process, antennas with improved performance, new analysis and design methods and tools, *etc.*

An antenna designer benefits significantly from knowledge of the physical limitations of the structure designed. Such limitations can be determined using the concept of optimum antenna current distributions. This concept is applied to realistic design situations presented in this thesis. The main advantage of the physical limitations derived from optimum currents is the possibility to study structures as they are, without making assumptions such as bounding geometry, electrical size, or symmetries.

Physical limitations customized for specific applications allow assessing some aspects of antenna design, including feasibility and performance of designs, and compromises to be made. For example, a designer may stop the design process if his/her design meets the specifications with 80 % of the maximum achievable performance. One way to obtain this maximum achievable performance is current optimization.

One method that appears useful in the process of antenna design is the single frequency antenna Q and $Q_{Z'}$ estimation. This method is based on the discrete nature of the analysis performed during the design of practical antennas. The method can be used in an initial automated antenna design stage, as a tool that saves the designer's time, *etc.* Examples of how this method can be integrated in the antenna analysis and design process are described in this thesis.

2 Background

2.1 *Q*-Factor and Stored Energy for Antenna Analysis

The Q-factor is a ubiquitous parameter in electrical engineering, propelled by its usefulness to other fields [33]. In general, the Q-factor is a measure of losses in oscillating and resonance phenomena. This is also the accepted interpretation of the Q-factor for antennas and high-frequency devices, *i.e.*, [21, 61, 75],

$$Q = \omega \frac{\text{average energy stored}}{\text{energy lost per unit time}}, \qquad (2.1)$$

where ω is the angular frequency of the oscillations. Energy is stored in the fields created by an antenna, and lost due to heating (ohmic losses) and radiation in (2.1). The surveys of Secs 2.2 and 2.3 present some of the work where the Q-factor is applied to the study of antennas.

The methods and derivations presented in this thesis are applicable, in principle, to all ranges of frequencies where antennas operate, unless otherwise stated. One of the fields where these methods appear to be useful is the estimation of antenna Q. In this context, there are situations where the Q-factor may bring little information to antenna analysis. An example of such a situation is the case of electrically large antennas where multiple, closely-spaced resonances exist in the frequency range of interest. In this case the commonly-accepted inverse proportionality of the Q-factor to the bandwidth of the antenna, [61, 75], may not hold [35, 110]. In addition, the Q-factors of some electrically large radiating structures are small, *e.g.*, $Q \lesssim 5$, which may question the use of Q for antenna analysis in this range of frequencies. However, many electrically small antennas can be modeled using the single resonance assumption [35, 110]. In this situation the Q-factor is commonly accepted as a parameter describing antenna performance, *i.e.*, smaller Q-values correspond to wider frequency bands of operation.

Electrically small antennas have been studied throughout the history of electrical engineering: some of the references presented in Secs 2.2 and 2.3 are focused on small antennas; text books are available on the topic of electrically small antennas [43, 44, 53, 102]. Solutions have been proposed to problems related to physical antenna miniaturization that leads to electrically small antennas, see *e.g.*, [1, 2, 7, 43, 77, 84, 85, 90, 93, 108, 112, 113]. Attempts have been made to obtain antennas that have performance reaching for the physical limitations corresponding to the radiating structures, including those presented in [6, 45, 58–60, 83, 88, 91, 92].

The remainder of this section presents a more detailed overview of the work in the fields of physical limitations on antenna Q and directivity, Sec. 2.2, and approaches to compute the electric and magnetic energies stored in the fields created by a radiating structure, Sec. 2.3. These quantities are frequently used throughout this thesis.

2.2   Fundamental Limitations on Antenna Q and Directivity

The necessity to study fundamental limitations on antenna parameters appeared naturally as radio technology advanced. The first publications in the field of fundamental limits on antenna parameters date back to the 1940s. A short, non-exhaustive historical overview of the progress in this field is presented in the following. This overview is based on the surveys presented in [102] and [86].

Wheeler introduced a simplified circuit model of an antenna in [104]. He used this model, consisting of a lumped capacitance or inductance and a radiation resistance, to derive fundamental limitations on the bandwidth and practical efficiency of small antennas.

Chu derived physical bounds on the gain, Q-factor and G/Q quotient of omnidirectional, lossless, electrically small antennas in [16]. He used the concept of smallest circumscribing sphere to divide the space into an interior region, with

unknown current distributions, and an exterior region, with known spherical wave distributions. Spherical wave theory was employed to study the maximum attainable gain of an antenna. Lumped-element circuit models were developed for the spherical waves. These models were used to compute the Q-factor of an electrically small antenna. Physical limitations on the minimum Q-factor and maximum G/Q ratio were derived using the circuit-based expressions for the Q-factor. Chu states that he approximates the equivalent circuits of spherical waves with simple series RLC circuits having the same behavior in the neighborhood of the operating frequency, except for the first mode (the electric dipole), [16]. A similar approach as Chu's was taken by Harrington in [46]. Chu's work was revisited by Hansen in [42] who reviewed the performance of many practical small antennas in [43].

Collin and Rothschild, [20], computed the Q-factor of antennas by subtracting the radiated energy density from the total energy density produced by a radiator. This subtraction yields the energy density associated with the reactive fields generated by an antenna, *i.e.*, the stored energy. This stored energy is used to compute antenna Q for spherical and cylindrical modes excited by sources placed on the surfaces of a sphere and infinite cylinder, respectively. The results obtained by these authors are the same as Chu's. Fante, [25], used the method proposed by Collin and Rothschild, [20], to study ideal antennas enclosed in imaginary spheres exciting both TE and TM modes. He found that a new Q-factor, apart from the Q-factors associated with spherical modes, has to be considered for describing such situations.

Another derivation of the energy stored in the fields created by a small antenna was proposed by McLean in [67]. This derivation allows the computation of the Q-factor with deeper physical insight. The author studies the first TM spherical mode and circular polarization consisting of the first TM and TE modes (properly weighted). The results obtained in this paper are in agreement with Chu's circuit-model based results without approximations, [16], and with those obtained with the theory derived by Collin and Rothschild, [20]. When the approximations indicated by Chu are made, the results obtained by McLean differ slightly from Chu's.

Prolate spheroidal radiating structures were considered by Foltz and McLean in [28]. Sten, Koivisto and Hujanen considered prolate and oblate spheroidal antennas in [87]. These papers appeared as a result of the necessity to study geometries closer to those of practical radiators. Some researchers had noted previously that many practical antennas do not occupy efficiently a spherical volume. Furthermore, it had been observed that such antennas perform rather far from the fundamental limitations derived for structures enclosed in spheres. In the former paper, the authors derived a more restrictive limit on the minimum Q of prolate spheroidal antennas. They used an equivalent circuit for the spheroidal functions describing the modes radiated by such antennas. The latter paper contains a detailed spherical-wave-function description of the fields radiated by prolate and oblate spheroidal structures. Based on this theory, the

authors derived approximate expressions for the minimum Q-factor in terms of the axial ratios of the spheroids.

Thiele, Detweiler and Penno computed the Q-factor of small antennas using the far field in [97]. They used the concept of visible and invisible space and integrated the far field in these regions. Based on these integrations and the properties of the superdirective ratio, the authors derived physical limitations on the minimum Q that were less optimistic compared to previous bounds.

Geyi derived fundamental limits on the Q-factor of omnidirectional and directional electrically small antennas in [30]. He used a straightforward approach based on spherical wave theory.

Thal [94] used an approach similar to Chu's, [16], to derive stricter limitations on Q that are more appropriate for realistic antennas. In addition, Thal included circuit models for the interior of the sphere bounding the antenna in order to take into account the energy stored in the fields excited inside the radiating structure. His examples are spherical wire antennas—structures that use more efficiently a spherical volume bounding the antennas than, *e.g.*, simple dipoles. In reference [95], Thal studies the relationship between orthogonal mode phases and antenna gain and Q limitations. He used a time domain analysis of Chu's lumped circuit models of radiating structures. In the more recent article [96], Thal derived circuit models for the first spherical modes based on scattering properties. He then used these models to express bounds on the Q-factor of electrically small antennas consisting of spherically arranged conductors.

An approach, entirely different compared to previous work, to derive physical bounds on the D/Q-ratio of arbitrary shape antennas was proposed by Gustafsson, Sohl and Kristensson in [37, 38]. This approach is based on the forward scattering properties of an antenna, described by the electric and magnetic polarizability dyadics of the radiating structure. These dyadics are considered in the low-frequency limit, *i.e.*, they quantify the electrostatic and magnetostatic behavior of the antenna. Mathematical properties of the polarizability dyadics and the optical theorem are used to relate scattering quantities of an antenna to its electrostatic and magnetostatic properties. These relations are further used to derive physical bounds on different antenna parameters, including the D/Q-ratio and gain-bandwidth product.

Yaghjian and Stuart, [109], used surface current equivalent principles to derive bounds on the Q-factor of electrically small lossless antennas of arbitrary shape radiating as either electric or magnetic dipoles. This work provides a connection between the concepts of general source and global electric-current source and the polarizability dyadics (used by Gustafsson *et al.*, [37, 38]). The derivation uses direct methods based on electromagnetic field theory in quasi-static conditions. These bounds are generalized to lossy electric and magnetic dipole antennas by Yaghjian, Gustafsson and Jonsson in [108].

Vandenbosch, [101], derived physical bounds on the arbitrary-shape, electrically small, antenna Q-factor for the first TE and TM modes. He used a new derivation of the energy stored in the fields created by an antenna in terms of

the current density excited in the radiating structure, [100]. A Taylor series expansion of the current density was used to approximate the Q-factor of small antennas that radiate as electric and magnetic dipoles.

2.3 Energies in the Fields Created by a Radiating Structure

The concept of electromagnetic wave energy is present in many of the publications on antenna Q fundamental limitations (Sec. 2.2). This energy is a key quantity in the definition (2.1) of the quality factor of antennas. Q-factors obtained using this energy-based definition have not been observed to have arbitrarily small values, as is the case for the input-impedance approximation [35, 66, 110].

Chu [16], Harrington [46], Hansen [42], Sten *et al.* [87], and Thal [94, 96] used the theory of spherical waves to estimate the electromagnetic propagating and non-propagating energy of the fields created by a radiating structure. This theory was combined by some of the authors with electrical network synthesis methods to obtain equivalent lumped-element circuit models associated with spherical modes. These models provided a deeper physical insight into the energy concept.

Fundamental electromagnetic theory, *e.g.*, Maxwell's equations, Poynting theorem, *etc.*, combined with spherical TE and TM mode theory was used to compute energies in a radiating system by Collin and Rothschild [20], Fante [25], McLean [67], and Geyi [30]. In reference [29] Geyi proposes a method to evaluate the Q-factor of small antennas based on the Poynting theorem in the time and frequency domain. Yaghjian *et al.*, [108, 109], approximated the energies in electrically small dipole antennas in terms of general and global electric-current sources using quasi-static electromagnetic theory. Vandenbosch, [100], expressed the energies in the fields created by an antenna in terms of the current density excited in the radiating structure using fundamental concepts of electromagnetism. Vandenbosh's results resemble partially Geyi's, [29].

3 Antenna Terms and Definitions

The time convention associated with complex quantities appearing throughout this thesis is $\mathrm{e}^{\mathrm{j}\omega t}$. The value of a time-varying harmonic field $\boldsymbol{E}(\boldsymbol{r}, \omega)$ is

$$\mathcal{E}(\boldsymbol{r}, t) = \mathrm{Re}\{\boldsymbol{E}(\boldsymbol{r}, \omega)\mathrm{e}^{\mathrm{j}\omega t}\}. \tag{3.1}$$

Electrically small antennas have dimensions such that they can be contained within a sphere whose diameter is small compared to a wavelength at the frequency of operation [3]. A precise borderline between electrically small and large antennas is rather hard to draw according to the previous definition. However, a widely accepted measure of electrical smallness is the radian sphere, [104, 105]. Electrically small antennas can be circumscribed by a sphere with the radius
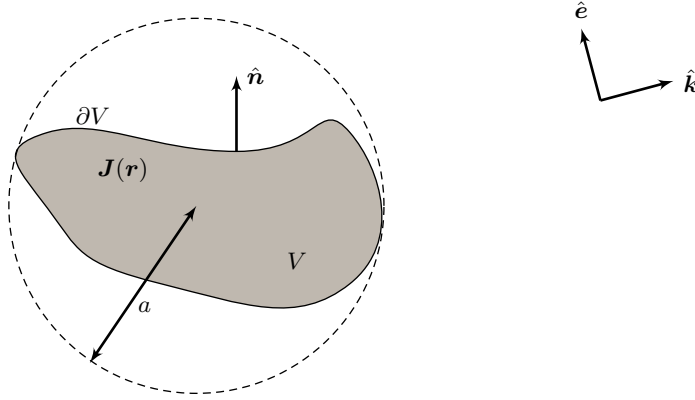
Figure 1: Illustration of radiating structure occupying a volume V which has the bounding surface ∂V with the outward pointing normal vector $\hat{\boldsymbol{n}}$. The smallest sphere that can enclose the antenna, *i.e.*, the smallest circumscribing sphere, has the radius a. The wave and polarization vectors, $\hat{\boldsymbol{k}}$ and $\hat{\boldsymbol{e}}$, respectively, are sketched for the far field region.

smaller than the radian length,

$$ka < 1, \tag{3.2}$$

where k is the wave number at the frequency of operation, and a is the radius of the smallest circumscribing sphere, see Fig. 1. The wave number can be expressed in terms of angular frequency, ω, ordinary frequency, f, and wavelength, λ, as

$$k = \frac{\omega}{c_0} = \frac{2\pi f}{c_0} = \frac{2\pi}{\lambda}, \tag{3.3}$$

where c_0 is the speed of light in free space.

The Q-factor (quality factor) of a resonant, lossless antenna is, [3],

$$Q = \frac{\omega W}{P_{\mathrm{r}}} = \frac{\omega(W_{\mathrm{e}} + W_{\mathrm{m}})}{P_{\mathrm{r}}}, \tag{3.4}$$

where W, W_{e} and W_{m} are respectively the total, electric and magnetic energies stored in the fields created by the antenna, and P_{r} is the power radiated by the antenna. Equation (3.4) is the lossless case of (2.1). For electrically small antennas the Q-factor is approximated by, [3, 35, 110],

$$Q \approx Q_{\mathrm{Z}'} = \frac{\omega_0 |Z'_{\mathrm{in,t}}(\omega_0)|}{2R_{\mathrm{in}}(\omega_0)}, \tag{3.5}$$

where ω_0 is the angular frequency at the resonance frequency, $Z'_{\mathrm{in,t}}$ is the first derivative of the input impedance of the antenna, tuned to resonate at ω_0, with respect to angular frequency, and R_{in} is the input resistance of the antenna. Note

that (3.4) and (3.5) are valid if the input impedance of the analyzed antenna can be modeled as a simple resistor-capacitor-inductor (RCL) circuit in the resonance frequency region [35, 110].

An alternate definition of *the Q-factor of lossless antennas*, valid both for resonant and non-resonant antennas, is [110]

$$Q = \frac{2\omega \max\{W_e, W_m\}}{P_r}.$$
(3.6)

This definition is equivalent to (3.4) for resonant antennas.

The bandwidth of an antenna, in the context of this thesis, represents the range of frequencies $[\omega_1, \omega_2]$ within which the antenna has a reflection coefficient with the magnitude less than or equal to Γ_0 [3]. The bandwidth is used, in general, as *fractional bandwidth*, *i.e.*, bandwidth divided by the center frequency of the band. The fractional bandwidth, B, is related to the Q-factor by, [110],

$$B = 2\frac{\omega_2 - \omega_1}{\omega_2 + \omega_1} \approx \frac{2}{Q} \frac{\Gamma_0}{\sqrt{1 - \Gamma_0^2}}.$$
(3.7)

This relation is valid when a simple resonance model can be used to describe the input impedance of the antenna.

The radiation intensity, $P(\hat{\boldsymbol{k}})$, is the power radiated from an antenna in a given direction, $\hat{\boldsymbol{k}}$, per solid angle.

The electric field polarization vector is a unitary vector, $\hat{\boldsymbol{e}}$, that describes the state of polarization of this field [3]. For example, a linearly polarized field has $|\hat{\boldsymbol{e}} \times \hat{\boldsymbol{e}}^*| = 0$ whereas a circularly polarized one has $|\hat{\boldsymbol{e}} \times \hat{\boldsymbol{e}}^*| = 1$, where the asterisk, $*$, denotes complex conjugation.

The partial directivity of an antenna is the ratio of that part of the radiation intensity corresponding to a given polarization, $\hat{\boldsymbol{e}}$, to the radiation intensity averaged over all directions, [3]:

$$D(\hat{\boldsymbol{k}}, \hat{\boldsymbol{e}}) = \frac{4\pi P(\hat{\boldsymbol{k}}, \hat{\boldsymbol{e}})}{P_r}.$$
(3.8)

If the direction is not specified, the direction of maximum radiation intensity is implied. *The gain* is equal to the directiviy for a lossless antenna.

4   Electromagnetic Energies and Physical Bounds

4.1   Stored and Radiated Energy Expressions

Antenna parameters quantify performance of radiating structures. Some of these parameters, often used in the design process of antennas, are defined in terms of

energy quantities of the field created by a radiating structure. Such parameters
are the Q-factor, directivity, gain, *etc.* Expressions that do not involve explicitly
the fields radiated by antennas are given in the following for the stored electric
and magnetic energies, partial radiation intensity, and total radiated power (after
a short review of important energy-related results in electromagnetics). These
expressions are applied throughout this thesis to antenna analysis and design.

Special attention has been given in electromagnetism to the concepts of stored
electric and magnetic energies (in the fields created by an antenna). These ener-
gies appear in definition (3.6). A simple insight into these energies is given by an
RLC circuit where electric and magnetic energy is stored in a capacitor and an
inductor, respectively, and energy is dissipated (modeling radiation) in a resistor.
The estimation of these stored energies has posed some difficulties which cannot
be overcome using the simple circuit-theory insight. Two such difficulties are the
interaction between the radiated and reactive field, which does not allow a simple
separation of radiated and stored fields, and the infinite total energy of the fields
created by a radiator, [20].

Collin and Rothschild, [20], used the energy balance given by the Poynting
theorem and observations pertaining power flow in radiated fields to overcome the
difficulties mentioned above. The energetic balance of an antenna, obtained by
integrating the Poynting vector over a surface S closed around and immediately
surrounding the antenna, is [19]

$$\frac{1}{2} \oint_S (\boldsymbol{E} \times \boldsymbol{H}^*) \cdot \hat{\boldsymbol{n}} \, \mathrm{d}S = P_\mathrm{r} + 2\mathrm{j}\omega(W_\mathrm{m} - W_\mathrm{e}), \qquad (4.1)$$

where $\boldsymbol{E}$ and $\boldsymbol{H}$ are the electric and magnetic fields, $\hat{\boldsymbol{n}}$ is the outward-pointing
normal vector to the surface S, P_r is the time-average power flowing across the
surface S, and W_e and W_m are the time-average reactive (stored) energies in the
electric and magnetic fields, respectively, within the volume enclosed by S. The
balance (4.1) determines the difference between the stored magnetic and electric
energies. This balance is used to calculate the energy density and velocity of
power flow in the far field, *i.e.*, when $S \to \infty$. The energy density in the far field
is subtracted from the total energy density in the fields created by an antenna.
The remainder after this subtraction is the energy density of the reactive field,
used to compute the energy stored in the fields created by the antenna.

Other methods to estimate the energies stored in the fields created by an
antenna have been proposed, including spherical-mode equivalent circuit-models,
approximations, *etc.*, see Sec. 2.3. Of particular importance in the scope of
this thesis is Vandenbosch's approach presented in [100]. The main results of
this approach are concentrated in equations (4.2) and (4.3). A discussion of
Vandenbosch's results on the topic of stored electric and magnetic energies can
be found in [41].

Consider the situation sketched in Fig. 2. A structure radiating electromag-
netic waves, *e.g.*, an antenna, communications device, mobile phone, *etc.*, occu-
pies a region of space denoted V. This structure is excited by a source inside or

on the boundary of V, ∂V, such that the current density $\boldsymbol{J}(\boldsymbol{r})$ exists inside the volume V. We assume, in this thesis, that the volume V contains only PEC and vacuum such that $\boldsymbol{J}(\boldsymbol{r})$ is an electric current. The electric and magnetic energies stored in the electromagnetic fields created by a radiating structure are expressed as, respectively, [100]

$$
W_{\mathrm{e}} = \frac{\eta_0}{4\omega} \int_V \int_V \nabla_1 \cdot \boldsymbol{J}_1 \nabla_2 \cdot \boldsymbol{J}_2^* \frac{\cos(kR_{12})}{4\pi k R_{12}}
$$
$$
- \left(k^2 \boldsymbol{J}_1 \cdot \boldsymbol{J}_2^* - \nabla_1 \cdot \boldsymbol{J}_1 \nabla_2 \cdot \boldsymbol{J}_2^* \right) \frac{\sin(kR_{12})}{8\pi} \, \mathrm{d}V_1 \, \mathrm{d}V_2 \quad (4.2)
$$

and

$$
W_{\mathrm{m}} = \frac{\eta_0}{4\omega} \int_V \int_V k^2 \boldsymbol{J}_1 \cdot \boldsymbol{J}_2^* \frac{\cos(kR_{12})}{4\pi k R_{12}}
$$
$$
- \left(k^2 \boldsymbol{J}_1 \cdot \boldsymbol{J}_2^* - \nabla_1 \cdot \boldsymbol{J}_1 \nabla_2 \cdot \boldsymbol{J}_2^* \right) \frac{\sin(kR_{12})}{8\pi} \, \mathrm{d}V_1 \, \mathrm{d}V_2, \quad (4.3)
$$

where η_0 is the impedance of free space, $\boldsymbol{J}_n = \boldsymbol{J}(\boldsymbol{r}_n)$, $n = 1, 2$, is the current density at positions $\boldsymbol{r}_n$ in the volume V occupied by the radiating structure (see Fig. 2), and $R_{12} = |\boldsymbol{r}_1 - \boldsymbol{r}_2|$ is the distance between a conceptual source and observation point (indexed by the subscripts 1 and 2, respectively).

The integral expressions (4.2) and (4.3) are derived by subtracting the radiated field energy density from the total energy density [100]; see also [41]. These expressions reduce to the stored energies in [13, 30] in the limit of electrically small radiators, i.e., $ka \ll 1$. Note that (4.2) and (4.3) are the result of a double integration over the domain occupied by a radiating structure. Compared to other approaches, these integrals do not involve explicitly the field radiated by the antenna.

The remainder of this section presents expressions for the other energy quantities used in defining the Q-factor and partial directivity of antennas. These quantities, the partial radiation intensity and total radiated power, can be found in textbooks on electromagnetic field theory such as [31, 72], expressed in terms of the current density in an antenna volume.

The radiation intensity in the $\hat{\boldsymbol{k}}$-direction, with the time convention (3.1), is [72]

$$
P(\hat{\boldsymbol{k}}) = \frac{\eta_0 k^2}{32\pi^2} |\boldsymbol{F}(\hat{\boldsymbol{k}})|^2, \quad (4.4)
$$

where $\boldsymbol{F}(\hat{\boldsymbol{k}})$ is the tangential component of the radiation vector, i.e.,

$$
\boldsymbol{F}(\hat{\boldsymbol{k}}) = -\hat{\boldsymbol{k}} \times \int_V \hat{\boldsymbol{k}} \times \boldsymbol{J}(\boldsymbol{r}) \mathrm{e}^{\mathrm{j}k\hat{\boldsymbol{k}}\cdot\boldsymbol{r}} \, \mathrm{d}V. \quad (4.5)
$$

Note that $\boldsymbol{r} \in V$ in the equation above. The electric field at position $\boldsymbol{r} \in \mathbb{R}^3$ is

$$
\boldsymbol{E}(\boldsymbol{r}) = -\mathrm{j}k\eta_0 \frac{\mathrm{e}^{-\mathrm{j}kr}}{4\pi r} \boldsymbol{F}(\hat{\boldsymbol{r}}) \quad \text{as } \boldsymbol{r} \to \infty, \quad (4.6)
$$
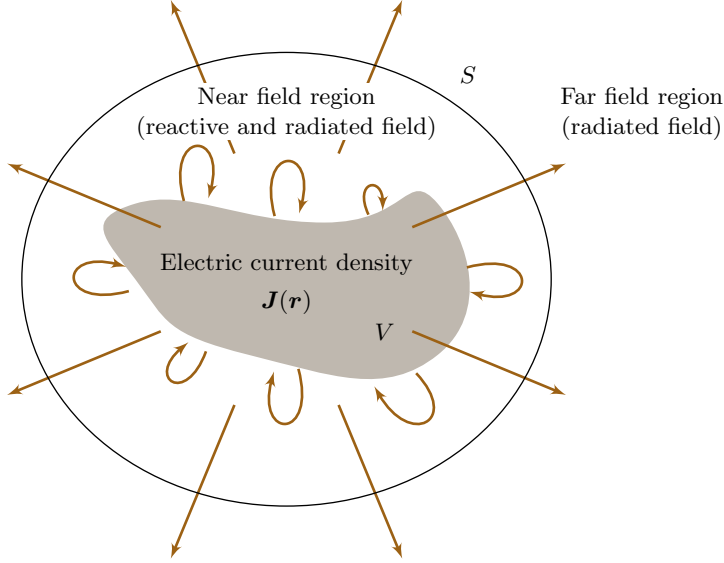
Figure 2: Radiating structure occupying the volume V where the current density $\boldsymbol{J}(\boldsymbol{r})$ is excited. The arrows illustrate, in a simplified manner, the power flow in the near and far field regions of the structure.

where $\hat{\boldsymbol{r}} = \boldsymbol{r}/r$ is a unit vector pointing in the direction of $\boldsymbol{r}$.

The partial radiation intensity in the $\hat{\boldsymbol{k}}$-direction for the polarization $\hat{\boldsymbol{e}}$, where $\hat{\boldsymbol{e}} \cdot \hat{\boldsymbol{k}} = 0$, is

$$P(\hat{\boldsymbol{k}}, \hat{\boldsymbol{e}}) = \frac{\eta_0 k^2}{32\pi^2} |\hat{\boldsymbol{e}}^* \cdot \boldsymbol{F}(\hat{\boldsymbol{k}})|^2 = \frac{\eta_0 k^2}{32\pi^2} \left| \int_V \hat{\boldsymbol{e}}^* \cdot \boldsymbol{J}(\boldsymbol{r}) \mathrm{e}^{\mathrm{j}k\hat{\boldsymbol{k}}\cdot\boldsymbol{r}} \, \mathrm{dV} \right|^2. \qquad (4.7)$$

A quadratic form of the current density $\boldsymbol{J}$ on the surface of a radiating structure, similar to (4.2) and (4.3), gives the total power radiated by the structure as, [31, 41, 100],

$$P_\mathrm{r} = \frac{\eta_0}{2} \int_V \int_V \left(k^2 \boldsymbol{J}_1 \cdot \boldsymbol{J}_2^* - \nabla_1 \cdot \boldsymbol{J}_1 \nabla_2 \cdot \boldsymbol{J}_2^* \right) \frac{\sin(kR_{12})}{4\pi k R_{12}} \, \mathrm{dV}_1 \, \mathrm{dV}_2. \qquad (4.8)$$

One of the main advantages of equations (4.2), (4.3), (4.7) and (4.8) is the fact that the integration domain is the finite volume occupied by the antenna, V. Common numerical techniques can be used to treat the singularity of the integrands in these equations, [52, 73]. Current densities on radiating structures are commonly computed by electromagnetic solvers. This fact facilitates the implementation of (4.2), (4.3), (4.7) and (4.8) in electromagnetic solvers for applications such as antenna optimization.

4.2   Energy Expressions for Discretized Antennas

The expressions (4.2), (4.3), (4.7), and (4.8) can be evaluated for many situations in which analytic expressions of the current densities can be derived. However, some situations of practical importance cannot be studied with these expressions in an analytic manner. Such situations can be treated by applying a discretization scheme to the integration domain V. The discretization procedure is presented for the general three-dimensional case of volumetric current densities. The applications presented in this thesis are implemented for surface formulations of electromagnetic problems solved using the method of moments. This method is well suited for antenna problems and provides reasonable accuracy such that it is one of the predominant methods in computational electromagnetics [14, 15, 52, 73, 103]. An illustration of a discretized planar structure is presented in Fig. 4.

One scheme to discretize an antenna is to divide the domain V into smaller regions, mesh cells/elements, such that the collection of all these regions, the mesh, is a "good approximation"[1] of V. A set of N vectorial, dimensionless basis functions $\boldsymbol{\psi}_n$ is defined on mesh elements in order to approximate the current density as

$$\boldsymbol{J}(\boldsymbol{r}) \approx \sum_{n=1}^{N} J_n \boldsymbol{\psi}_n(\boldsymbol{r}). \tag{4.9}$$

Note that, in general, N is not equal to the number of mesh elements. We introduce

$$\mathbf{J} = (J_1, J_2, \ldots, J_N)^{\mathrm{T}} \tag{4.10}$$

to denote an $N \times 1$ matrix of complex expansion coefficients with units of volumetric current density—Am^{-2}. Replacing (4.9) in the equations (4.2), (4.3), (4.7), and (4.8) and rearranging the summations involved we obtain

$$W_{\mathrm{e}} \approx \frac{1}{4\omega} \sum_{m=1}^{N} \sum_{n=1}^{N} J_m^* X_{\mathrm{e},mn} J_n = \frac{1}{4\omega} \mathbf{J}^{\mathrm{H}} \mathbf{X}_{\mathrm{e}} \mathbf{J}, \tag{4.11}$$

$$W_{\mathrm{m}} \approx \frac{1}{4\omega} \sum_{m=1}^{N} \sum_{n=1}^{N} J_m^* X_{\mathrm{m},mn} J_n = \frac{1}{4\omega} \mathbf{J}^{\mathrm{H}} \mathbf{X}_{\mathrm{m}} \mathbf{J}, \tag{4.12}$$

$$P(\hat{\boldsymbol{k}}, \hat{\boldsymbol{e}}) \approx \frac{1}{2\eta_0} \left| \sum_{n=1}^{N} F_n^* J_n \right|^2 = \frac{1}{2\eta_0} \left| \mathbf{F}^{\mathrm{H}} \mathbf{J} \right|^2, \tag{4.13}$$

and

$$P_{\mathrm{r}} \approx \frac{1}{2} \sum_{m=1}^{N} \sum_{n=1}^{N} J_m^* R_{\mathrm{r},mn} J_n = \frac{1}{2} \mathbf{J}^{\mathrm{H}} \mathbf{R}_{\mathrm{r}} \mathbf{J}, \tag{4.14}$$

---

[1]To qualify as a "good approximation", a number of application specific requirements have to be met, including geometric tolerance in representing details, accuracy of the desired results, *etc.*

where the superscripts H and T denote Hermitian and ordinary transposition, respectively. The matrices $\mathbf{X}_\mathrm{e}$, $\mathbf{X}_\mathrm{m}$ and $\mathbf{R}_\mathrm{r}$ have $N \times N$ elements whereas $\mathbf{F}$ has $N \times 1$ elements. These matrices have the elements, respectively,

$$
X_{\mathrm{e},mn} = \eta_0 \int_V \int_V \nabla_1 \cdot \boldsymbol{\psi}_{m1} \nabla_2 \cdot \boldsymbol{\psi}_{n2} \frac{\cos(kR_{12})}{4\pi kR_{12}}
$$
$$
- \left(k^2 \boldsymbol{\psi}_{m1} \cdot \boldsymbol{\psi}_{n2} - \nabla_1 \cdot \boldsymbol{\psi}_{m1} \nabla_2 \cdot \boldsymbol{\psi}_{n2} \right) \frac{\sin(kR_{12})}{8\pi} \, \mathrm{dV}_1 \, \mathrm{dV}_2, \quad (4.15)
$$

$$
X_{\mathrm{m},mn} = \eta_0 \int_V \int_V k^2 \boldsymbol{\psi}_{m1} \cdot \boldsymbol{\psi}_{n2} \frac{\cos(kR_{12})}{4\pi kR_{12}}
$$
$$
- \left(k^2 \boldsymbol{\psi}_{m1} \cdot \boldsymbol{\psi}_{n2} - \nabla_1 \cdot \boldsymbol{\psi}_{m1} \nabla_2 \cdot \boldsymbol{\psi}_{n2} \right) \frac{\sin(kR_{12})}{8\pi} \, \mathrm{dV}_1 \, \mathrm{dV}_2, \quad (4.16)
$$

$$
R_{\mathrm{r},mn} = \eta_0 \int_V \int_V \left(k^2 \boldsymbol{\psi}_{m1} \cdot \boldsymbol{\psi}_{n2} - \nabla_1 \cdot \boldsymbol{\psi}_{m1} \nabla_2 \cdot \boldsymbol{\psi}_{n2} \right) \frac{\sin(kR_{12})}{4\pi kR_{12}} \, \mathrm{dV}_1 \, \mathrm{dV}_2, \quad (4.17)
$$

and
$$
F_n^* = \frac{-\mathrm{j}k\eta_0}{4\pi} \int_V \hat{\boldsymbol{e}}^* \cdot \boldsymbol{\psi}_n(\boldsymbol{r}) \mathrm{e}^{\mathrm{j}k\hat{\boldsymbol{k}}\cdot\boldsymbol{r}} \, \mathrm{dV}, \quad (4.18)
$$

where the explicit $\boldsymbol{r}$-dependence of the basis functions has been omitted or replaced by the subscripts $1, 2$ when ambiguity may occur, i.e., $\boldsymbol{\psi}_{m1} = \boldsymbol{\psi}_m(\boldsymbol{r}_1)$, and $\boldsymbol{\psi}_{n2} = \boldsymbol{\psi}_n(\boldsymbol{r}_2)$. The matrices $\mathbf{X}_\mathrm{e}$ and $\mathbf{X}_\mathrm{m}$ are positive semi-definite for electrically small structures and may become indefinite for larger structures [40]. Note that it is assumed that magnetic materials are not contained in the antenna volume V.

The total radiation intensity (4.4) has not been approximated in terms of the discrete expansion coefficients $\mathbf{J}$ because, in general, radiating structures are designed for specific polarizations $\hat{\boldsymbol{e}}$.

Antenna quantities can be expressed using the discrete expressions (4.11)–(4.14). The Q-factor (3.6) and the directivity (3.8) are expressed as, respectively,

$$
Q \approx \frac{\max\{\mathbf{J}^\mathrm{H}\mathbf{X}_\mathrm{e}\mathbf{J}, \mathbf{J}^\mathrm{H}\mathbf{X}_\mathrm{m}\mathbf{J}\}}{\mathbf{J}^\mathrm{H}\mathbf{R}_\mathrm{r}\mathbf{J}} \quad (4.19)
$$

and
$$
D \approx \frac{4\pi}{\eta_0} \frac{\left|\mathbf{F}^\mathrm{H}\mathbf{J}\right|^2}{\mathbf{J}^\mathrm{H}\mathbf{R}_\mathrm{r}\mathbf{J}}. \quad (4.20)
$$

The D/Q quotient is expressed, combining (3.8) and (3.6), as

$$
\frac{D(\hat{\boldsymbol{r}}, \hat{\boldsymbol{e}})}{Q} = \frac{2\pi P(\hat{\boldsymbol{r}}, \hat{\boldsymbol{e}})}{\omega \max\{W_\mathrm{e}, W_\mathrm{m}\}}. \quad (4.21)
$$

Replace (4.11)–(4.13) in (4.21) to obtain the D/Q quotient for discretized structures:

$$\frac{D(\hat{\boldsymbol{k}}, \hat{\boldsymbol{e}})}{Q} = \frac{4\pi \left|\mathbf{F}^{\mathrm{H}}\mathbf{J}\right|^2}{\eta_0 \max\{\mathbf{J}^{\mathrm{H}}\mathbf{X}_{\mathrm{e}}\mathbf{J}, \mathbf{J}^{\mathrm{H}}\mathbf{X}_{\mathrm{m}}\mathbf{J}\}}. \tag{4.22}$$

One of the outcomes of discretization is the possibility to evaluate energy expressions by ordinary matrix operations, $e.g.$, (4.11)–(4.14), (4.19)–(4.22). Common numerical methods can be employed to evaluate the integrals in (4.15)–(4.18). Note that matrices are evaluated at a single frequency in (4.19) to calculate Q, which gives information about bandwidth using, $e.g.$, a single resonance model [35, 110]. A quadratic-form expression in terms of eigencurrents, for the Q-factor of scatterers, is presented in [47]. In this reference, the author solves an optimization problem to find the minimum Q of a certain structure. The same author optimized the Q-factor of antenna arrays in free space using an expression similar to (4.19) in [48].

4.3   Physical Bounds on Antenna Parameters

There exist electromagnetic quantities, including antenna parameters, which are convex quantities [11, 36]. This fact allows the formulation of some antenna optimization problems as convex problems. Numerical algorithms and tools are available for solving such optimization problems, see $e.g.$, [11, 26, 32, 63], for an overview and examples of optimization methods, including methods for convex problems. The discrete expressions (4.11)–(4.14) are readily suitable for numerical optimization algorithms.

Physical bounds on antenna parameters can be computed by solving appropriately formulated optimization problems. Discrete expressions such as (4.11)–(4.14) play a key role in these problems. One of the most important advantages of the discrete formulation is the possibility to derive physical limitations for a structure as it is, without assuming a bounding geometry as, $e.g.$, a sphere, spheroid, cylinder, $etc.$ This allows the analysis of many practical situations, including complex geometries not easily approachable using analytic methods, geometries with interacting fixed regions and regions to optimize, $etc.$

Optimum current densities on antennas are the solutions of the optimization problems considered. The performance achieved by these optimum current densities is used to compare the performance of realistic structures. Performance can either be the convex parameter optimized or a non-convex parameter describing optimum currents, $e.g.$, D/Q is a convex parameter whereas Q is non-convex; we can compare the Q of physical structures with the Q of a D/Q-optimum current density. Even though optimum currents may or may not be physical, such currents give an upper bound for the performance that a physical antenna can attain. Physically realizable optimum antenna currents have been derived throughout the history of antenna theory, usually for specific applications [10, 23, 62, 65, 78, 99]. Note that the formulations presented in this thesis do

not include a feed model, *e.g.*, a voltage gap feeding a part of the structure [52]. However, a feeding scheme of all possible feed points can be obtained with an expression such as the impedance-like, method-of-moments equation (4.35). This optimum-current feeding scheme may or may not be physically realizable.

In the remainder of this section, examples of optimization problems formulated for obtaining bounds on different antenna parameters are presented, Sec. 4.3.1–4.3.3. These examples are described in more detail in [36]. In addition, a procedure to obtain bounds when radiating structures are divided (abstractly) in fixed regions and regions which can be optimized is presented in Sec. 4.3.4.

4.3.1   Maximum D/Q

Equations (4.21) and (4.22) can be maximized, to obtain bounds on the D/Q quotient, using different methods. A Lagrangian formulation is used in [40] to maximize (4.21) under the assumption that $W_e \geqslant W_m$. Equation (4.22) can be maximized as a convex problem. This problem can be formulated in different equivalent ways, of which two are presented in the following.

One approach is to maximize the numerator of (4.22), *i.e.*, $|\mathbf{F}^H\mathbf{J}|^2$. This maximization can be replaced by that of $\mathrm{Re}\{\mathbf{F}^H\mathbf{J}\}$, [36, 40]. It is also sufficient to consider real valued quantities $\hat{\boldsymbol{e}} \cdot \boldsymbol{F} \approx \mathbf{F}^H\mathbf{J}$. The convex optimization problem is

$$
\begin{aligned}
\text{maximize}_\mathbf{J} \quad & \mathrm{Re}\{\mathbf{F}^H\mathbf{J}\} \\
\text{subject to} \quad & \mathbf{J}^H\mathbf{X}_e\mathbf{J} \leqslant 1 \\
& \mathbf{J}^H\mathbf{X}_m\mathbf{J} \leqslant 1,
\end{aligned} \tag{4.23}
$$

where the current matrix $\mathbf{J}$ is rescaled such that $\mathbf{J}^H\mathbf{X}_e\mathbf{J}$ is dimensionless. Equation (4.23) yields an upper bound for (4.21) as

$$
\frac{D(\hat{\boldsymbol{k}}, \hat{\boldsymbol{e}})}{Q} \leqslant \frac{4\pi|\mathbf{F}^H\mathbf{J}_o|^2}{\eta_0 \max\{\mathbf{J}_o^H\mathbf{X}_e\mathbf{J}_o, \mathbf{J}_o^H\mathbf{X}_m\mathbf{J}_o\}}, \tag{4.24}
$$

where $\mathbf{J}_o$ is an optimum current in the sense of (4.23).

An alternative formulation to (4.23) is based on the fact that the maximum of two convex functions is convex, [11]. This fact is used to minimize the energy stored in the fields generated by an antenna. The convex optimization formulation is, [36],

$$
\begin{aligned}
\text{minimize}_\mathbf{J} \quad & \max\{\mathbf{J}^H\mathbf{X}_e\mathbf{J}, \mathbf{J}^H\mathbf{X}_m\mathbf{J}\} \\
\text{subject to} \quad & \mathbf{F}^H\mathbf{J} = -\mathrm{j}.
\end{aligned} \tag{4.25}
$$

The bound has the same form, (4.24). The optimization problem (4.25) can be relaxed to the dual problem, [11],

$$
\begin{aligned}
\text{minimize}_\mathbf{J} \quad & \mathbf{J}^H \left(\alpha\mathbf{X}_e + (1-\alpha)\mathbf{X}_m\right) \mathbf{J} \\
\text{subject to} \quad & \mathbf{F}^H\mathbf{J} = -\mathrm{j},
\end{aligned} \tag{4.26}
$$

over $0 \leqslant \alpha \leqslant 1$. The solution of (4.26) for a fixed α is

$$\mathbf{J} = \frac{-\mathrm{j}\left(\alpha\mathbf{X}_\mathrm{e} + (1-\alpha)\mathbf{X}_\mathrm{m}\right)^{-1}\mathbf{F}}{\mathbf{F}^\mathrm{H}\left(\alpha\mathbf{X}_\mathrm{e} + (1-\alpha)\mathbf{X}_\mathrm{m}\right)^{-1}\mathbf{F}}, \tag{4.27}$$

with appropriate scaling of $\mathbf{J}$ such that $\mathbf{F}^\mathrm{H}\mathbf{J}$ is dimensionless.

   The upper bound for (4.21) and (4.22) is reached by an optimum current, $\mathbf{J}_\mathrm{o}$, computed with, *e.g.*, a convex optimization formulation such as (4.23), (4.25) or (4.26), a Lagrangian formulation, *etc.* This current may or may not be physically realizable. However, its performance in terms of D/Q gives an upper bound on the D/Q of a physically realizable current density. The Q-factor (4.19) of such optimum currents, *i.e.*,

$$Q \approx \frac{\max\{\mathbf{J}_\mathrm{o}^\mathrm{H}\mathbf{X}_\mathrm{e}\mathbf{J}_\mathrm{o}, \mathbf{J}_\mathrm{o}^\mathrm{H}\mathbf{X}_\mathrm{m}\mathbf{J}_\mathrm{o}\}}{\mathbf{J}_\mathrm{o}^\mathrm{H}\mathbf{R}_\mathrm{r}\mathbf{J}_\mathrm{o}}, \tag{4.28}$$

can be used to compare Q-factors of physical structures. This comparison may show that an antenna has a Q smaller than that of a D/Q-optimum current, which is not optimum in the sense of Q.

4.3.2   Given Radiation Pattern and Its Minimum Q

A radiated field (4.5) denoted $\boldsymbol{F}_0(\hat{\boldsymbol{k}})$ is realized by a current density $\boldsymbol{J}_0$ in the antenna volume V (see Fig. 2), such that

$$\boldsymbol{J}_0(\boldsymbol{r}) = \int_\Omega \boldsymbol{F}_0(\hat{\boldsymbol{k}})\mathrm{e}^{-\mathrm{j}k\hat{\boldsymbol{k}}\cdot\boldsymbol{r}}\,\mathrm{d}\Omega_{\hat{\boldsymbol{k}}}, \tag{4.29}$$

where $\Omega_{\hat{\boldsymbol{k}}}$ is a sphere of unit radius and outward-pointing normal vector $\hat{\boldsymbol{k}}$. A current density that realizes $\boldsymbol{F}_0$ can be found by maximizing the projection of a realized far field, $\boldsymbol{F}$, on the desired far field, $\boldsymbol{F}_0$, defined as

$$\int_\Omega \boldsymbol{F}_0(\hat{\boldsymbol{k}}) \cdot \boldsymbol{F}^*(\hat{\boldsymbol{k}})\,\mathrm{d}\Omega_{\hat{\boldsymbol{k}}} = \int_V \boldsymbol{J}^*(\boldsymbol{r}) \cdot \boldsymbol{J}_0(\boldsymbol{r})\,\mathrm{d}V \approx \mathbf{J}^\mathrm{H}\mathbf{V}_\mathrm{vol}\mathbf{J}_0, \tag{4.30}$$

where $\mathbf{J}_0$ is the column vector (4.10) of expansion coefficients corresponding to $\boldsymbol{J}_0$, and the matrix $\mathbf{V}_\mathrm{vol}$ has the elements

$$\mathbf{V}_{\mathrm{vol},mn} = \int_V \boldsymbol{\psi}_m(\boldsymbol{r}) \cdot \boldsymbol{\psi}_n(\boldsymbol{r})\,\mathrm{d}V. \tag{4.31}$$

   The convex optimization problem that yields a current density $\boldsymbol{J}$ that approximates $\boldsymbol{J}_0$ is, [36],

$$\begin{aligned}
\text{maximize}_\mathbf{J} \quad & \mathrm{Re}\{\mathbf{J}_0^\mathrm{H}\mathbf{V}_\mathrm{vol}\mathbf{J}\} \\
\text{subject to} \quad & \mathbf{J}^\mathrm{H}\mathbf{X}_\mathrm{e}\mathbf{J} \leqslant 1 \\
& \mathbf{J}^\mathrm{H}\mathbf{X}_\mathrm{m}\mathbf{J} \leqslant 1.
\end{aligned} \tag{4.32}$$

A lower bound on the Q-factor of an antenna having a far field approximated by $\boldsymbol{F}_0$ can be obtained by solving the minimization problem, [36],

$$
\begin{aligned}
\text{minimize}_{\mathbf{J}} \quad & \max\{\mathbf{J}^{\mathrm{H}}\mathbf{X}_{\mathrm{e}}\mathbf{J}, \mathbf{J}^{\mathrm{H}}\mathbf{X}_{\mathrm{m}}\mathbf{J}\} \\
\text{subject to} \quad & \left(\int_{\Omega} |\boldsymbol{F}(\hat{\boldsymbol{k}}) - \boldsymbol{F}_0(\hat{\boldsymbol{k}})|^2 \, \mathrm{d}\Omega_{\hat{\boldsymbol{k}}}\right)^{1/2} < 4\pi\delta,
\end{aligned}
\tag{4.33}
$$

where δ is the maximum least-squares deviation of $\boldsymbol{F}$ from $\boldsymbol{F}_0$. Note that any norm can be used to quantify the deviation of the realized far field from the desired far field.

4.3.3 Maximum D/Q for Superdirective Antennas

A superdirective antenna has a directivity greater than directivities of typical antennas with the same electrical size [5, 43, 57, 65]. Denoting D_0 the directivity of such typical antennas, the convex optimization problem that yields the current density maximizing the D/Q ratio is, [36],

$$
\begin{aligned}
\text{minimize}_{\mathbf{J}} \quad & \max\{\mathbf{J}^{\mathrm{H}}\mathbf{X}_{\mathrm{e}}\mathbf{J}, \mathbf{J}^{\mathrm{H}}\mathbf{X}_{\mathrm{m}}\mathbf{J}\} \\
\text{subject to} \quad & \mathbf{F}^{\mathrm{H}}\mathbf{J} = -\mathrm{j} \\
& \mathbf{J}^{\mathrm{H}}\mathbf{R}_{\mathrm{r}}\mathbf{J} \leqslant \frac{4\pi}{\eta_0 D_0}.
\end{aligned}
\tag{4.34}
$$

4.3.4 Embedded Antennas

From the electromagnetic wave generation point of view, many mobile devices that integrate antennas consist of two spatial domains, as illustrated in Fig. 3. One of the domains, the "antenna region", is represented by the space reserved for a structure fed by the transmitter(s). The other domain, the "ground plane", contains all other parts integrated in the device. This domain usually contains metallic parts that act as ground for the structure in the antenna region. The structures in both domains contribute, in general, to radiated fields. It is also observed that the antenna region usually occupies a small fraction of the entire device.

Situations such as that described in the previous paragraph are not readily analyzable with the formulations of Sec. 4.3.1–4.3.3. However, a block matrix decomposition applied to the matrices involved in these formulations allows the study of antennas embedded in and interacting with other structures, [55, 76]. Consider the situation illustrated in Fig. 3. The current density in the antenna region can be controlled by, *e.g.*, a feed, optimization to derive physical bounds, *etc.* The ground plane current is determined by the current in the antenna region and the interaction between the two domains. This interaction is described by a system of equations that relates the current-density expansion coefficients to other
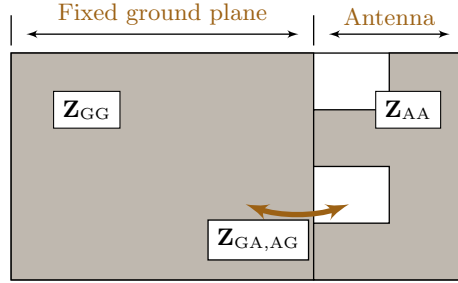
Figure 3: Schematic illustration of antenna embedded in a wireless terminal. Gray shading—metallic parts.

quantities used to model the radiating system. One of the simplest ways to describe such an interaction is the impedance-like equation

$$\mathbf{Z}\mathbf{J} = \mathbf{V}, \tag{4.35}$$

where $\mathbf{Z} = (Z_{mn})$ is a matrix describing the interaction between basis functions p and q with $p, q = 1, 2, \ldots, N$, and $\mathbf{V}$ is an N-element column vector describing the excitation corresponding to each basis function. The system of equations (4.35) is usually solved in method of moments (MoM) algorithms based on the electric field integral equation (EFIE) [48, 52, 73]. The elements of $\mathbf{Z}$ do not depend on the current density flowing in the volume V. These elements depend only on the electromagnetic properties of the radiating system and its environment. The excitation vector $\mathbf{V}$ models sources feeding the structure. This vector does not appear in an optimization formulation, as shown in the following.

A block matrix decomposition is applied to (4.35), [55, 76]:

$$\begin{pmatrix} \mathbf{Z}_{\mathrm{AA}} & \mathbf{Z}_{\mathrm{AG}} \\ \mathbf{Z}_{\mathrm{GA}} & \mathbf{Z}_{\mathrm{GG}} \end{pmatrix} \begin{pmatrix} \mathbf{J}_{\mathrm{A}} \\ \mathbf{J}_{\mathrm{G}} \end{pmatrix} = \begin{pmatrix} \mathbf{V}_{\mathrm{A}} \\ \mathbf{0} \end{pmatrix}. \tag{4.36}$$

The indexes A and G denote the antenna region and ground plane, respectively. For example, the elements of $\mathbf{Z}_{\mathrm{AA}}$ have both basis functions (whose interaction the elements of $\mathbf{Z}_{\mathrm{AA}}$ describe) in the antenna region whereas the elements of $\mathbf{Z}_{\mathrm{GA}}$ have the first basis function in the ground plane and the second in the antenna region. The **0**-matrix in the right hand side of (4.36) expresses the fact that the current in the ground plane is controlled by the current in the antenna region, *i.e.*,

$$\begin{cases} \mathbf{J}_{\mathrm{A}} &= (\mathbf{Z}_{\mathrm{AA}} - \mathbf{Z}_{\mathrm{AG}}\mathbf{Z}_{\mathrm{GG}}^{-1}\mathbf{Z}_{\mathrm{GA}})^{-1}\mathbf{V}_{\mathrm{A}} \\ \mathbf{J}_{\mathrm{G}} &= -\mathbf{Z}_{\mathrm{GG}}^{-1}\mathbf{Z}_{\mathrm{GA}}\mathbf{J}_{\mathrm{A}} = \mathbf{T}\mathbf{J}_{\mathrm{A}} \end{cases}. \tag{4.37}$$

These relations allow expressing the quadratic forms (4.11)–(4.14) in terms of $\mathbf{J}_{\mathrm{A}}$ as, respectively,

$$\mathbf{J}^{\mathrm{H}}\mathbf{X}_{\mathrm{e}}\mathbf{J} = \mathbf{J}_{\mathrm{A}}^{\mathrm{H}}\left(\mathbf{X}_{\mathrm{e,AA}} + \mathbf{T}^{\mathrm{H}}\mathbf{X}_{\mathrm{e,GA}} + \mathbf{X}_{\mathrm{e,AG}}\mathbf{T} + \mathbf{T}^{\mathrm{H}}\mathbf{X}_{\mathrm{e,GG}}\mathbf{T}\right)\mathbf{J}_{\mathrm{A}}, \tag{4.38}$$

$$\mathbf{J}^{H}\mathbf{X}_{m}\mathbf{J} = \mathbf{J}_{A}^{H}\left(\mathbf{X}_{m,AA} + \mathbf{T}^{H}\mathbf{X}_{m,GA} + \mathbf{X}_{m,AG}\mathbf{T} + \mathbf{T}^{H}\mathbf{X}_{m,GG}\mathbf{T}\right)\mathbf{J}_{A}, \qquad (4.39)$$

$$\left|\mathbf{F}^{H}\mathbf{J}\right|^{2} = \left|\left(\mathbf{F}_{A} + \mathbf{T}^{T}\mathbf{F}_{G}\right)^{H}\mathbf{J}_{A}\right|^{2}, \qquad (4.40)$$

and

$$\mathbf{J}^{H}\mathbf{R}_{r}\mathbf{J} = \mathbf{J}_{A}^{H}\left(\mathbf{R}_{r,AA} + \mathbf{T}^{H}\mathbf{R}_{r,GA} + \mathbf{R}_{r,AG}\mathbf{T} + \mathbf{T}^{H}\mathbf{R}_{r,GG}\mathbf{T}\right)\mathbf{J}_{A}, \qquad (4.41)$$

where the $\mathbf{X}_{e}$, $\mathbf{X}_{m}$, $\mathbf{F}$ and $\mathbf{R}_{r}$-blocks are defined in the same manner as the $\mathbf{Z}$-blocks. Note that (4.38)–(4.41) do not contain the feed-model matrix $\mathbf{V}_{A}$. The sizes of the matrices in parentheses in these equations are determined by the size of the region that is optimized, discretization scheme, *etc.* However, these matrices have the number of rows (and columns, where applicable) smaller than N, the size of the matrices describing the entire structure.

5   Antenna Analysis and Design Applications

Standard electromagnetic EFIE-based MoM solvers compute most of the quantities needed to estimate (4.15)–(4.17). The integration of this estimation in an EFIE-based MoM solver is described in Sec. 5.1. The MoM solver used in this thesis is described in Sec. 5.3. The matrix approximations (4.11)–(4.14) are readily suitable for global optimization algorithms. The integration of these expressions in a genetic algorithm optimization with MoM simulation is described in Secs 5.4 and 5.5.

5.1   Method of Moments

Numerical methods for electromagnetic problems are commonly used in the process of antenna analysis and design. Details and examples of such computational methods can be found in, *e.g.*, [52, 73]. One of the methods used to solve problems in electromagnetism is the method of moments [48]. This method, applicable in general to a wider class of problems than electromagnetism, transforms a boundary-value problem involving integral or differential equations into a matrix problem, *e.g.*, (4.35), [52]. The elements of the matrices involved are computed based on a discretization scheme applied to the object analyzed and the formulation of the problem, *i.e.*, the equation that is solved. The MoM is particularly suited for antenna problems because it does not require space to be truncated around the analyzed structure [52].

Consider the discretization scheme presented in Sec. 4.2. In the remainder of this thesis expansion coefficients $\mathbf{J}$ are surface-currents and integrals are evaluated on the surface ∂V enclosing the radiating structure (that occupies the volume V). An EFIE-based mixed-potential formulation using Galerkin testing computes an impedance matrix with the elements, [52, 73],

$$Z_{mn} = j\eta_{0}\int_{\partial V}\int_{\partial V}\left(k\boldsymbol{\psi}_{m1}\cdot\boldsymbol{\psi}_{n2} - \frac{1}{k}\nabla_{1}\cdot\boldsymbol{\psi}_{m1}\nabla_{2}\cdot\boldsymbol{\psi}_{n2}\right)\frac{e^{-jkR_{12}}}{4\pi R_{12}}\,dS_{1}\,dS_{2}. \qquad (5.1)$$

Note that due to the inner product operation performed in the MoM, *i.e.*, one integration over the surface bounding the radiating structure, the SI unit for Z_{mn} is Ωm^2. Various forms of (5.1) are usually computed by MoM electromagnetic solvers.

The matrices $\mathbf{X}_\text{e}$, $\mathbf{X}_\text{m}$ and $\mathbf{R}_\text{r}$ with the elements (4.15)–(4.17) can be derived in an MoM solver as that introduced above with little computational effort. This derivation involves splitting the computation of $\mathbf{Z}$ in two parts, and performing a new computation. Express the impedance matrix as

$$\mathbf{Z} = \mathbf{Z}_\text{m} - \mathbf{Z}_\text{e}, \tag{5.2}$$

where

$$Z_{\text{e},mn} = \frac{-\eta_0}{\text{j}k} \int_{\partial V} \int_{\partial V} \nabla_1 \cdot \boldsymbol{\psi}_{m1} \nabla_2 \cdot \boldsymbol{\psi}_{n2} \frac{\text{e}^{-\text{j}kR_{12}}}{4\pi R_{12}} \,\text{dS}_1 \,\text{dS}_2, \tag{5.3}$$

and

$$Z_{\text{m},mn} = \text{j}k\eta_0 \int_{\partial V} \int_{\partial V} \boldsymbol{\psi}_{m1} \cdot \boldsymbol{\psi}_{n2} \frac{\text{e}^{-\text{j}kR_{12}}}{4\pi R_{12}} \,\text{dS}_1 \,\text{dS}_2 \tag{5.4}$$

and introduce the matrix $\mathbf{Z}_\text{em}$ with the elements

$$Z_{\text{em},mn} = -\eta_0 \int_{\partial V} \int_{\partial V} \left(k^2 \boldsymbol{\psi}_{m1} \cdot \boldsymbol{\psi}_{n2} - \nabla_1 \cdot \boldsymbol{\psi}_{m1} \nabla_2 \cdot \boldsymbol{\psi}_{n2} \right) \frac{\text{e}^{-\text{j}kR_{12}}}{8\pi} \,\text{dS}_1 \,\text{dS}_2. \tag{5.5}$$

These quantities are used to compute

$$\mathbf{X}_\text{e} = \text{Im}\{\mathbf{Z}_\text{e} - \mathbf{Z}_\text{em}\}, \tag{5.6}$$

$$\mathbf{X}_\text{m} = \text{Im}\{\mathbf{Z}_\text{m} - \mathbf{Z}_\text{em}\}, \tag{5.7}$$

and

$$\mathbf{R}_\text{r} = \text{Re}\{\mathbf{Z}_\text{m} - \mathbf{Z}_\text{e}\}. \tag{5.8}$$

The most computationally demanding part of the above derivation (excluding the effort for computing (5.3) and (5.4), which depends on the MoM solver implementation) is the integration (5.5). This integral has a non-singular integrand such that it does not pose difficulties for numerical computation. In fact, the only difference between (5.5) and (5.3), (5.4) is the singular factor $1/R_{12}$.

The EFIE impedance matrix can be expressed alternatively as

$$\mathbf{Z} = \mathbf{R}_\text{r} + \text{j}(\mathbf{X}_\text{m} - \mathbf{X}_\text{e}). \tag{5.9}$$

Based on this equation, we call $\mathbf{R}_\text{r}$ the radiation resistance matrix, and $\mathbf{X}_\text{e}$ and $\mathbf{X}_\text{m}$ the electric and magnetic reactance matrices, respectively. The radiation resistance matrix is positive semi-definite [48]. The reactance matrices are positive semi-definite for electrically small structures. These matrices may become indefinite for larger structures [36, 40, 41]. The quadratic form

$$\frac{1}{2}\mathbf{J}^\text{H}\mathbf{Z}\mathbf{J} \approx P_\text{r} + 2\omega\text{j}(W_\text{m} - W_\text{e}) \tag{5.10}$$

resembles the energetic balance (4.1) given by integrating the Poynting vector on a surface closed around and immediately surrounding a radiating structure.

5.2   Single Frequency $Q_{Z'}$ Computation

The antenna parameter $Q_{Z'}$, introduced in [110], can be evaluated from a single-frequency current density in an EFIE-based MoM solver with little additional computational effort. The first derivative with respect to wave number of the impedance matrix elements (5.1) is

$$\frac{k\partial Z_{mn}}{\eta_0 \partial k} = \int_{\partial V} \int_{\partial V} \mathrm{j} \left(k^2 \boldsymbol{\psi}_{m1} \cdot \boldsymbol{\psi}_{n2} + \nabla_1 \cdot \boldsymbol{\psi}_{m1} \nabla_2 \cdot \boldsymbol{\psi}_{n2} \right) \frac{\mathrm{e}^{-\mathrm{j}kR_{12}}}{4\pi k R_{12}}$$
$$+ \left(k^2 \boldsymbol{\psi}_{m1} \cdot \boldsymbol{\psi}_{n2} - \nabla_1 \cdot \boldsymbol{\psi}_{m1} \nabla_2 \cdot \boldsymbol{\psi}_{n2} \right) \frac{\mathrm{e}^{-\mathrm{j}kR_{12}}}{4\pi} \, \mathrm{d}V_1 \, \mathrm{d}V_2. \quad (5.11)$$

The element-wise, first-order, wave-number derivative of the impedance matrix,

$$\mathbf{Z}' = \frac{\partial \mathbf{Z}}{\partial k} = \frac{1}{k} \left(\mathbf{Z}_\mathrm{m} + \mathbf{Z}_\mathrm{e} - 2\mathbf{Z}_\mathrm{em} \right), \quad (5.12)$$

with the elements given by (5.11) is used to evaluate $Q_{Z'}$ from the current density computed at a single frequency. Equation (5.12) is obtained by comparing (5.11) to (5.3)–(5.5).

The Q-factor of an antenna tuned to resonance, in a single-resonance model, can be approximated as [35, 110]

$$Q_{Z'}(k_0) \approx \frac{k_0 \left| Z'_{\mathrm{in,t}}(k_0) \right|}{2R_\mathrm{in}(k_0)}, \quad (5.13)$$

where prime denotes first derivative with respect to wave number, k_0 is the resonance wave number, $Z_{\mathrm{in,t}}$ is the input impedance of the antenna tuned to resonate at k_0, and

$$Z_\mathrm{in}(k) = R_\mathrm{in}(k) + \mathrm{j} X_\mathrm{in}(k) \quad (5.14)$$

is the input impedance of the antenna without tuning circuitry. Note the change of variables $k = \omega/c_0$, performed in (5.13), compared to (3.5), in order for Z_in to be expressed in terms of the same frequency variable as $\mathbf{Z}$, whose elements are (5.1). If the single resonance assumption does not hold, the derivative of the input impedance may approach zero such that $Q_{Z'} \approx 0$. In these situations the Brune, multiple-resonance, input-impedance-approximation procedure [106] may produce a better approximation of Q than $Q_{Z'}$. If the antenna is tuned to resonate at the wave number k_0 using a series-connected, ideal, lumped inductor or capacitor, we have

$$Z_\mathrm{in,t}(k) = Z_\mathrm{in}(k) + \mathrm{j} X_\mathrm{t}(k), \quad (5.15)$$

where

$$X_\mathrm{t}(k) = \begin{cases} \dfrac{-kX_\mathrm{in}(k_0)}{k_0} & X_\mathrm{in}(k_0) < 0 \\[2ex] \dfrac{-k_0 X_\mathrm{in}(k_0)}{k} & X_\mathrm{in}(k_0) > 0 \end{cases}. \quad (5.16)$$

At the resonance frequency the input impedance has only the real part, *i.e.*,

$$Z_{\text{in,t}}(k_0) = R_{\text{in}}(k_0). \tag{5.17}$$

Replace (5.15) and (5.16) in (5.13) to obtain

$$Q_{Z'}(k_0) \approx \left| \frac{k_0 Z'_{\text{in}}(k_0)}{2R_{\text{in}}(k_0)} + \text{j} \frac{|X_{\text{in}}(k_0)|}{2R_{\text{in}}(k_0)} \right|. \tag{5.18}$$

In the above equation, Z'_{in} is traditionally computed using a numerical approximation based on evaluating Z_{in} at two closely spaced frequencies. An single-frequency alternative to this approach is presented in the following.

We express the input impedance derivative in terms of the input admittance. The admittance matrix, given by:

$$\mathbf{J} = \mathbf{Y}\mathbf{V} = \mathbf{Z}^{-1}\mathbf{V}, \tag{5.19}$$

defines the input admittance (and equivalently impedance) of the antenna using a voltage gap model of feeding edge elements:

$$Y_{\text{in}} = \frac{\mathbf{V}^{\text{T}}\mathbf{Y}\mathbf{V}}{V_{\text{in}}^2}, \tag{5.20}$$

where V_{in} is the voltage applied across the gap. Note that in (4.35) we have, for the formulation (5.1),

$$V_f = V_{\text{in}}\ell_f, \tag{5.21}$$

where a voltage gap is applied along basis function f, and ℓ_f is the length of the edge common to the two rectangles where $\boldsymbol{\psi}_f \neq \mathbf{0}$. We consider that the source is real-valued and frequency independent, *i.e.*, $\mathbf{V}' = \mathbf{0}$. The input impedance derivative becomes

$$Z'_{\text{in}} = \left(\frac{1}{Y_{\text{in}}}\right)' = -\frac{Y'_{\text{in}}}{Y_{\text{in}}^2} = -\frac{\left(\mathbf{V}^{\text{T}}\mathbf{Y}\mathbf{V}\right)'}{V_{\text{in}}^2 Y_{\text{in}}^2} = -\frac{\mathbf{V}^{\text{T}}\mathbf{Y}'\mathbf{V}}{I_{\text{in}}^2}, \tag{5.22}$$

where I_{in} is the current flowing into the antenna input. Consider the following equation:

$$\mathbf{0} = \left(\mathbf{Z}^{-1}\mathbf{Z}\right)' = \left(\mathbf{Z}^{-1}\right)'\mathbf{Z} + \mathbf{Z}^{-1}\mathbf{Z}'. \tag{5.23}$$

Multiplication from the right by $\mathbf{Z}^{-1}$ gives

$$\mathbf{Y}' = -\mathbf{Z}^{-1}\mathbf{Z}'\mathbf{Z}^{-1} = -\mathbf{Y}\mathbf{Z}'\mathbf{Y}, \tag{5.24}$$

such that the input impedance derivative is

$$Z'_{\text{in}} = \frac{\mathbf{J}^{\text{T}}\mathbf{Z}'\mathbf{J}}{V_{\text{in}}^2 Y_{\text{in}}^2} = \frac{\mathbf{J}^{\text{T}}\mathbf{Z}'\mathbf{J}}{I_{\text{in}}^2}, \tag{5.25}$$

where the fact that $\mathbf{Z}$ and $\mathbf{Y}$ are symmetric matrices has been used. Replace (5.25) in (5.18) to obtain

$$Q_{\mathrm{Z}'}(k_0) \approx \left| \frac{k_0 \mathbf{J}^{\mathrm{T}} \mathbf{Z}' \mathbf{J}}{2 R_{\mathrm{in}} I_{\mathrm{in}}^2} + \mathrm{j} \frac{|X_{\mathrm{in}}|}{2 R_{\mathrm{in}}} \right|, \qquad (5.26)$$

where all the frequency-dependent quantities are computed for the wave number k_0. The corresponding expression for $Q_{\mathrm{Z}'}$ in [12] differs from (5.26) as the former includes frequency derivatives of the current density and complex conjugates.

The single-frequency $Q_{\mathrm{Z}'}$ derivation has been presented for the case of a series circuit element used for tuning an antenna, as in [110]. An expression similar to (5.26) can be derived using a parallel tuning susceptance.

5.3   In-House Method of Moments Solver

An in-house method of moments solver computes the matrices (5.1), (5.11), and (4.15)–(4.18), for the situations of Sec. 6. These are the impedance matrix and its frequency derivative, reactance and radiation resistance matrices, and far field matrix, respectively. Rectangular mesh elements are used to discretize the surfaces of the analyzed structures. This choice of discretization allows the analysis of some antenna applications even though rectangular elements lack the geometry-conforming flexibility of triangles [73]. Galerkin's method is employed, *i.e.*, the same set of functions is used as testing and basis functions [48, 73]. These functions are zero except on the surfaces of two adjacent rectangles, *i.e.*, rectangles sharing a common edge, as illustrated in Fig. 4. The amplitudes of the basis functions increase from 0 to 1, linearly toward the common edge—they have a "rooftop" profile, [68]. Considering a numbering rule of the two rectangles supporting a basis function, the direction of this function is perpendicular to the common edge pointing from the first to the second rectangle.

The integrals in (5.1) and (5.11) are evaluated using the Gaussian quadrature when the two integration domains are at a great distance from each other. The singularity extraction technique is applied [48, 73] when the domains are identical or neighbor mesh elements of 2D structures. In the case of 3D radiating structures, the variable change described in [56] is employed to integrate the $1/R$ singularity. Four points are used in all Gaussian quadratures involved in the estimation of these integrals (except for the results presented in Sec. 6.2.3 where six points are used).

There exist situations where the performance of a fabricated antenna may be reduced compared with the performance of its corresponding simulated model. Typical reasons for this performance reduction are the nature of the discretization scheme, the difficulties in modeling fine geometrical details and fabrication tolerances, *etc.* These situations are usually observed when randomness is used to generate antennas, *e.g.*, using a genetic optimization algorithm, [54, 71]. Two such situations are covered by the following observations related to rectangular
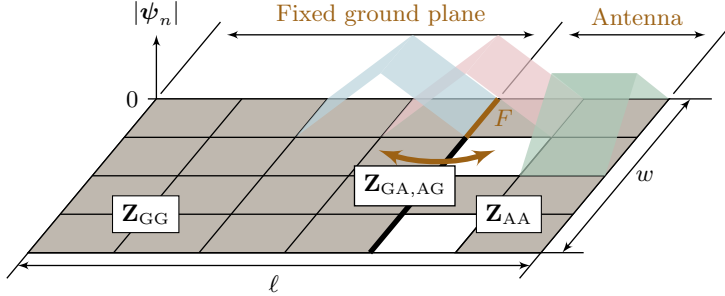
Figure 4: Illustration of discretization for a structure using rectangular mesh elements. Metal areas are depicted in gray shading. The amplitudes of three of the total $6 \times 3 + 5 \times 4 - 4 - 3$ basis functions are depicted in blue, pink and green shading. The feeding edge is marked F. The locations of basis and testing functions when a block matrix decomposition is applied to the impedance matrix, $\mathbf{Z}$, are illustrated by the positions of the resulting blocks, $\mathbf{Z}_{AA}$, $\mathbf{Z}_{GG}$, $\mathbf{Z}_{GA}$ and $\mathbf{Z}_{AG}$, where the subscripts G and A denote the ground plane and antenna region, respectively.

mesh elements and rooftop basis functions. The first observation pertains isolated mesh elements (sometimes called "orphan" elements). The mesh elements marked "1" and "2" in Fig. 5a are examples of isolated elements. None of the basis and test functions are non-zero on such isolated elements—they do not support basis functions. This results in the fact that isolated mesh elements do not affect the MoM solution obtained using solvers with basis functions defined on pairs of mesh elements [64, 71, 107], *e.g.*, the in-house solver. The second observation pertains non-isolated mesh elements that share a single vertex—corner or diagonal connections. An example corner connection is between the elements marked "1" and "2" in Fig. 5b. Due to the fact that the basis functions are zero at the element edges opposed the common edge, in the MoM analysis the current flowing through the corner connection is negligible. However, in a fabricated sample there may be an electrical connection at the corner such that a current may flow through that corner. This electrical connection may result in a performance alteration mostly due to the finite conductivity of real metals. In order to avoid such alterations, the fabrication has to ensure that corner conditions from simulation are reproduced in fabrication, *e.g.*, if a corner model with 0 curvature radius is used then no electrical connection should exist at corners in a fabricated model.

The procedure described in Sec. 4.3.4 can be applied to embedded antennas. The domains where the basis functions are non-zero overlap intrinsically, see Fig. 4. This fact allows the application of a block matrix decomposition to the matrices involved in the MoM computation. Consider a borderline between an antenna region and ground plane, *e.g.*, the thick line in Fig. 4. The antenna region contains the basis functions that are non-zero on rectangles to the right
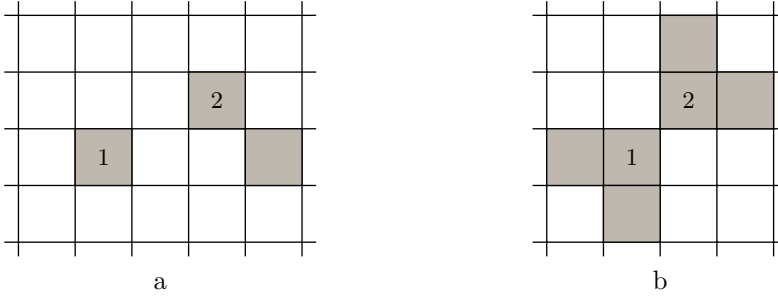
Figure 5: Example of isolated mesh elements (marked "1" and "2" in a) and corner connection (between the non-isolated elements marked "1" and "2" in b) that may appear in a mesh describing a discretized structure. Metallic regions are depicted in gray shading.

of the line or on pairs of rectangles lying across the line (one rectangle to the left and one to the right of the line). The ground plane contains the basis functions that are non-zero only on rectangles to the left of the line. In addition, the natural overlapping allows the existence of connections from the ground plane to the antenna region and back to the ground plane, as depicted in Fig. 4.

5.4   Genetic Algorithms

Optimization algorithms can be used to improve antenna performance, which is measured in terms of antenna parameters included in the optimization goals. Global algorithms are one class of methods that perform such optimizations. Mathematical considerations and examples of global optimization algorithms are presented in [4, 9, 11, 22, 26, 27, 32, 50, 51, 63, 69, 70, 74, 79, 80, 82, 89, 111].

Some antenna optimization problems have a number of possible solutions that is prohibitive for applying deterministic optimization methods. Furthermore, the performance of these solutions is sometimes predictable only by numerical simulation of each solution. Heuristic methods, *e.g.*, genetic algorithms, random search, particle swarm optimization, ant colony, *etc.*, yield reasonable solutions to optimization problems that are prohibitive for deterministic methods, [49, 76, 81, 98].

A genetic algorithm has been chosen to illustrate the use of the discrete expressions of Sec. 4.2 for antenna optimization. This algorithm is based on Holter's implementation distributed with the PB-FDTD package, [98]. Genetic algorithms feature an acceptably fast convergence to suboptimal solutions and avoid local extrema, [76]. These algorithms are based on simple genetic principles that mimic population evolution (of humans, animals, plants). Genetic principles are based on concepts such as "generation", "individual", "population", "gene", "chromosome", "breeding", "offspring", "crossover", "mutation", *etc.*
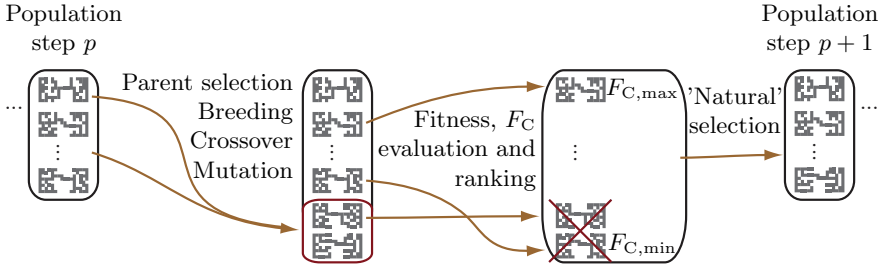
Figure 6: Illustration of a genetic algorithm implementation for antenna optimization.

The commonly accepted principle of genetics is improvement of a population in steps, as depicted schematically in Fig. 6. Improvement is measured in terms of fitness which is, *e.g.*, a scalar cost function, F_{C}, defined in terms of antenna quantities. A population is made of one or more individuals. An individual is defined by traits which are determined by genes. A collection of genes forms a chromosome; the traits of an individual are established by one or more chromosomes. All genes in an individual form its genotype. The individuals in a population compete to breed offspring. The breeding process is affected by the phenomena of crossover and mutation. The GA implementation used in this thesis enlarges the population by two offspring at each step. The offspring's fitness is evaluated and the individuals are ranked according to their fitness. The two least-fit individuals are removed from the population, which returns to its original size.

The notions introduced above can be defined in the context of antenna optimization. We consider the discretization rule introduced in Sec. 4.2, *i.e.*, a radiating structure is divided into N_{e} mesh elements. A possible approach to defining individuals and populations is to consider each mesh element a gene. Such a gene can be interpreted in a binary manner: the mesh element may or may not exist in an individual. An individual is, in this context, an arbitrary collection of any of the mesh elements. It is understood here that these mesh elements maintain all their characteristics when defining an individual: position in the mesh and in space, shape, dimensions, material, *etc.*

Each of the $2^{N_{\text{e}}}$ individuals represents a unique radiating structure. A cost function, F_{C}, determines the "fitness" of each individual (radiating structure). Examples of such cost functions are the directivity, Q-factor, radiation resistance, and more complex functions of one or more antenna parameters, including those presented in Sec. 6. Note that even a small number of mesh elements may result in a large number of combinations, impossible in general to study individually. For example, a mesh with 50 elements results in more than 10^{15} different radiating structures that need to be studied.

Fitness is evaluated during genetic optimization using an electromagnetic solver. A method of moments solver is easily integrable into a genetic optimiza-

tion algorithm, [55]. Following the GA/MoM scheme, [55], the antenna optimization process is reduced to a process of matrix row and column search. In addition, this scheme allows direct integration of the discrete expressions (4.11)–(4.14) into fitness computations involving quantities such as the Q-factor, directivity, *etc.*

A mother structure is defined in the GA/MoM scheme, [55], prior to starting an optimization process. This structure is a radiator having usually a geometry limiting the space (allocated to the radiator searched by the optimization) and the structure intended for the radiator (metallic parts, dielectric parts, *etc.*). The mother structure is discretized using a rule as that described in Sec. 4.2. The matrices $\mathbf{Z}_M$, (5.1), $\mathbf{X}_{e,M}$, (4.15), $\mathbf{X}_{m,M}$, (4.16), $\mathbf{R}_{r,M}$, (4.17), and $\mathbf{F}_M$, (4.18), are computed for the mother structure.

Discretization rules used for the mother structure and genetic optimization may be different. However, genetic characteristics should be characterized with the accuracy needed using the discretization chosen for the mother structure. In other words, the discrete elements of the mother structure should allow reproducing the finest details of each possible individual. One choice that appears natural is to use the same discretization rule for the genetic optimization and mother structure.

During the optimization process, genetic information is translated into matrices describing each individual. These matrices, $\mathbf{Z}_I$, $\mathbf{X}_{e,I}$, $\mathbf{X}_{m,I}$, $\mathbf{R}_{r,I}$ and $\mathbf{F}_I$, are compiled from rows and columns of corresponding mother matrices. The rows and columns compiling the individual matrices have the same indexes, *i.e.*, one set of indexes is used to define all matrices describing an individual. In this way, the rather involved numerical computations of the individual matrices whose elements are given by (4.15)–(4.18) are performed only once prior to an optimization process. Note that, in the case of genetic optimization, the feed concept is used to determine the current density on each individual using (4.35).

The procedure for embedded antennas, described in Sec. 4.3.4, is well suited for genetic optimization, [55, 76]. A block matrix decomposition can be applied to the mother matrices prior to the optimization. The matrices in parentheses in (4.37)–(4.41) become mother matrices in which the genetic algorithm searches for the combination of rows and columns that gives the minimum cost function. The sizes of the matrices manipulated by the genetic algorithm repetitively reduce even though the preprocessing becomes more computationally demanding.

The genetic algorithm is neither an exhaustive search of the optimum solution nor an exhaustive evaluation of the characteristics of certain individuals. This algorithm uses genetic principles to drive an initially random population toward a suboptimal solution avoiding to some extent local extrema. Genetic principles allow the appearance of unwanted characteristics of offspring ("malformations"). Such characteristics may have unpredictable effects on the performance of a fabricated structure, [18, 54, 71, 107]. The GA used in this thesis "purges" unwanted traits after each offspring generation. It has been observed that purging must be performed in such a manner that the population can still evolve toward optimum.
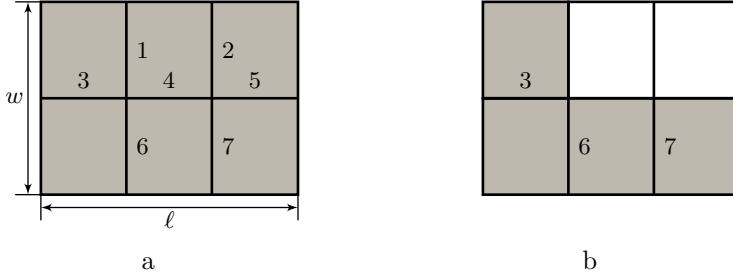
Figure 7: Illustration of a mother structure (a) and an individual derived from it (b). Gray-shaded rectangles—PEC mesh elements. Basis functions are numbered.

5.5   GA/MoM for Rectangular Regions

As an example consider radiating structures limited to infinitely thin rectangular sheets of perfect electrical conductor, as the structures depicted in Fig. 7. Such a region, with the dimensions $\ell \times w$, is the mother structure for an optimization algorithm. This mother structure is divided in $N_\ell = 3$ and $N_w = 2$ rectangular mesh elements in the ℓ and w-directions, respectively. Basis functions are defined on pairs of adjacent, metallic mesh elements, *i.e.*, on mesh edges shared by two metallic elements. These edges are numbered $1, 2, \ldots, 7$ in Fig. 7a. All matrices relevant for optimization, *e.g.*, $\mathbf{Z}_{\mathrm{M}}$, $\mathbf{X}_{\mathrm{e,M}}$, *etc.*, are computed in a preprocessing stage. These matrices, with the size 7×7 (7×1 in the case of $\mathbf{F}$), are used in the MoM computation of parameters corresponding to different individuals.

The same dicretization rule is applied for the genetic algorithm, such that the mother structure has the genotype

$$\text{Mother genotype}: (1,1,1,1,1,1), \tag{5.27}$$

where the six binary genes correspond to the rectangular mesh elements numbered from left to right and top to bottom in Fig. 7a. The individual depicted in Fig. 7b does not have rectangles 2 and 3 such that its genotype is

$$\text{An individual genotype}: (1,0,0,1,1,1). \tag{5.28}$$

The mother impedance matrix is

$$\mathbf{Z}_{\mathrm{M}} = \begin{pmatrix} z_{11} & z_{12} & z_{13} & z_{14} & z_{15} & z_{16} & z_{17} \\ z_{21} & z_{22} & z_{23} & z_{24} & z_{25} & z_{26} & z_{27} \\ z_{31} & z_{32} & z_{33} & z_{34} & z_{35} & z_{36} & z_{37} \\ z_{41} & z_{42} & z_{43} & z_{44} & z_{45} & z_{46} & z_{47} \\ z_{51} & z_{52} & z_{53} & z_{54} & z_{55} & z_{56} & z_{57} \\ z_{61} & z_{62} & z_{63} & z_{64} & z_{65} & z_{66} & z_{67} \\ z_{71} & z_{72} & z_{73} & z_{74} & z_{75} & z_{76} & z_{77} \end{pmatrix}. \tag{5.29}$$

All individual matrices, *e.g.*, $\mathbf{Z}_\mathrm{I}$, $\mathbf{X}_{\mathrm{e,I}}$, $\mathbf{F}_\mathrm{I}$, *etc.*, are compiled by rows 3, 6 and 7 (intersected with the same-index columns for square matrices):

$$\mathbf{Z}_\mathrm{I} = \left(\begin{array}{ccc} z_{33} & z_{36} & z_{37} \\ z_{63} & z_{66} & z_{67} \\ z_{73} & z_{76} & z_{77} \end{array} \right) \tag{5.30}$$

The MoM system of equations (4.35) is written for the individual as

$$\mathbf{Z}_\mathrm{I}\mathbf{J}_\mathrm{I} = \mathbf{V}_\mathrm{I}, \tag{5.31}$$

where $\mathbf{J}_\mathrm{I}$ is a three-element column vector of basis-function expansion coefficients, and $\mathbf{V}_\mathrm{I}$ is a three-element column vector describing the feed of the individual. The discrete expressions (4.11)–(4.14) are evaluated from matrices compiled using the same indexes 3, 6 and 7 such that, *e.g.*, the electric energy stored in the fields created by this individual is

$$W_{\mathrm{e,I}} \approx \frac{1}{4\omega}\mathbf{J}_\mathrm{I}^\mathrm{H}\mathbf{X}_{\mathrm{e,I}}\mathbf{J}_\mathrm{I}. \tag{5.32}$$

The genetic optimization algorithm used in this thesis searches for that combination of rows and columns of the mother matrix (5.29) that minimizes the targeted cost function. Note that genetic algorithm implementations can also maximize cost functions.

6 Examples and Verifications

The theory presented in Sec. 4 is applied, as described in Sec. 5, to the study of radiating structures. The agreement between the theoretical results and numerical simulations performed with in-house and commercial tools confirm the validity of the results of Secs 4 and 5.

The four situations sketched in Fig. 8 are considered, where antennas are made of an infinitely thin perfect electrical conductor. In the first example, Fig. 8a, antennas limited to a rectangular region with normalized dimensions $\ell \times w = 2 \times 1$ are optimized using the GA/MoM procedure presented in Sec. 5.5. The physical bound on the Q-factor of an electrically small PEC rectangle is computed, [37–39], and the optimized-antenna Q-factors are compared with this bound. Some of the optimized antennas are simulated with the commercial electromagnetic solver ESI-CEM [24] to confirm the results obtained with the in-house MoM solver described in Sec. 5.3 and single-frequency expressions of Sec. 4. The first example is presented in Sec. 6.1.

The second example is the analysis of a simplified 2D wireless device model presented in Sec. 6.2. This model is depicted in Fig. 8b and consists of an antenna (black in the figure) embedded in a device (black and gray shading in the figure). Structures are optimized in the antenna region and physical bounds
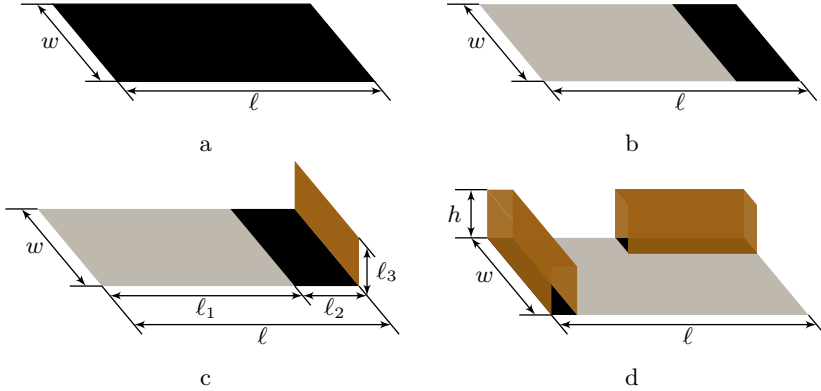
Figure 8: Four antenna design situations, labeled a–d, analyzed in Secs 6.1–6.4, respectively. Gray shading—fixed regions, *i.e.*, ground plane. Black and bronze—regions where structures can be optimized, *i.e.*, antenna region [17].

and optimum currents are derived for the model using the results of Secs 4 and 5. Some of the optimized structures are simulated using the commercial solver ESI-CEM [24]. Further integration of optimized structures in communication systems is considered using the commercial tool BetaMatch [8].

A 3D simplified wireless device model is analyzed in Sec. 6.3. This model is depicted in Fig. 8c and consists of an antenna embedded in a communications device. In addition to an analysis similar to that of Sec. 6.2, *i.e.*, second example, the optimization for $Q_{Z'}$ is investigated. System integration of antennas optimized for Q, $Q_{Z'}$ or both is considered for this 3D device model.

The fourth example considers an antenna placement in wireless terminal situation, Sec. 6.4. The purpose of the analysis is to find the location of an antenna in a device that could give the best performance in terms of D/Q or Q using physical bounds and optimum currents, Sec. 4. The model considered is depicted in Fig. 8d. The limiting geometry is a parallelepiped with the normalized dimensions $\ell \times w \times h = 2 \times 1 \times 0.1$. The ground plane [17] occupies $90\,\%$ of the area of one largest-area faces of the parallelepiped. The antenna region occupies $10\,\%$ of the volume of the parallelepiped and consists of simple arrangements of rectangular PEC sheets.

6.1   2D Rectangular Regions

We consider a rectangular region with the dimensions $\ell/w = 2$. This region is divided in $N_\ell = 64$ and $N_w = 32$ elements in the ℓ and w-directions, respectively. This particular choice of discretization results in square mesh elements. The mother matrices used in the GA/MoM procedure, see Sec. 5.5, have $2N_\ell N_w - N_\ell - N_w = 4000$ rows (and 4000 columns for square matrices). The frequencies

for the analysis are chosen such that $k\ell \in [0.1, 1.3]$ ($ka \in [0.06, 0.7]$, where a is the radius of the smallest circumscribing sphere). These frequencies correspond to electrical dimensions usually considered small. A voltage gap model is used to feed the structures in the GA antenna populations. This gap corresponds to the basis function oriented in the ℓ-direction that is non-zero on the two mesh elements closest to the center of the rectangular region. These two elements are removed from the genotype such that the GA individuals have 2046 genes, at the most.

The population used in the genetic algorithm has 200 individuals. Eighty of these individuals are chosen randomly to compete for breeding offspring, *i.e.*, tournament selection. Offspring generation is subjected to crossover and mutation. Crossover happens at two random positions in the genotype with probability 0.8. The mutation rate is 0.2 when the population evolves "naturally"; in this situation a single gene is mutated at a time. The probability of mutation becomes 1 when the population does not improve during 200 steps. In all succeeding steps, all offspring have up to 10 random genes mutated at a time. If a new individual with better performance is found, the evolution returns to "natural" conditions, 0.2 single-gene mutation probability. The purpose of this implementation is to increase the chances of finding better solutions in less steps.

The cost function minimized by the GA is

$$F_{\mathrm{C}} = \alpha_{\mathrm{Q}} Q + \alpha_{\mathrm{R}} 2\omega \left| \frac{W_{\mathrm{m}} - W_{\mathrm{e}}}{P_{\mathrm{r}}} \right| + A_{\mathrm{N}}, \qquad (6.1)$$

where α_{Q} and α_{R} are weights that correspond to the Q-factor and resonance, respectively, and A_{N} is the metallic area normalized to ℓw. The weights α_{Q} and α_{R} control the optimization algorithm. Either of these weights is emphasized at a time to obtain antennas optimized for Q or resonance. These two optimization criteria have $\alpha_{\mathrm{Q}} = 4$, $\alpha_{\mathrm{R}} = 1$ and $\alpha_{\mathrm{Q}} = 1$, $\alpha_{\mathrm{R}} = 4$, respectively. For illustration purpose resonance is evaluated from the difference between the stored electric and magnetic energies (normalized to the radiated energy). These energies are equal at resonance.

The stop condition of the algorithm is genetic stability of the population during 10^4 steps. This condition can be replaced by the best individual performance in the current population. When this performance is close enough to physical bounds or optimum-current performance, [34, 36, 38, 40], the optimization process can be stopped.

From the symmetry point of view, three groups of structures are considered: non-symmetric, symmetric in the ℓ-direction and symmetric in the ℓ and w-directions, see Fig. 4. These are denoted "None", "Single", and respectively "Double" in Figs. 9 and 9. The corresponding numbers of genes in the genotype are: 2046, 1023 and 512.

The smallest Q-factor (4.19) of 5 optimized antennas for each symmetry and optimization criterion is depicted in Fig. 9. The physical bound on the Q-factor
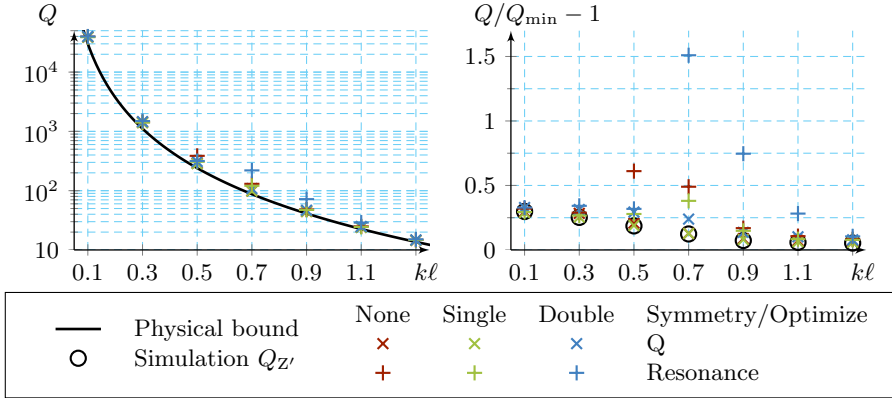
Figure 9: Left—GA-optimized antenna Q-factors compared with the physical bound [37, 38] for rectangular regions. The smallest Q-factor obtained in 5 GA runs for each symmetry (none, single—along ℓ, and double—along ℓ and w) and optimization criterion (Q-factor or resonance) is depicted. Right—deviation of the Q-factors depicted to the left relative to the physical bound $Q_{\min}$ [37, 38]. The deviations of the Q-factors (5.13) evaluated from the input impedance computed by ESI-CEM [24] are included for the antennas having the smallest Q-factor for each frequency, regardless of optimization criterion or symmetry.

of a rectangular region with the same dimensions is computed using the results in [37–39]. This bound is derived assuming the structure radiates as a small electric dipole, *i.e.*, omnidirectional, directivity 1.5 radiation. The relative deviation of the Q-factors from this physical bound is also depicted in Fig. 9. The antennas with the smallest Q in all GA runs per $k\ell$-value have been simulated with ESI-CEM [24]. These antennas, depicted in Fig. 10, have radiation patterns resembling that of an electric dipole. The $Q_{Z'}$-factors (5.13), where Z'_{in} is approximated from the input impedance computed by ESI-CEM, are included in Fig. 9 for comparison.

Some observations can be made even though the number of GA runs is rather small. Antennas symmetric in the ℓ-direction have the smallest Q-factors. Antennas symmetric both in the ℓ and w-directions have the greatest Q-factors. Intermediate Q-factors are obtained by antennas that are non-symmetric. The antennas obtained by the GA have Q-factors that deviate less than 10 % (larger electrical dimensions) or 30 % (smaller dimensions) relative to the physical bound. Antennas optimized for resonance have greater Q-factors than those optimized for Q, significantly greater for some electrical dimensions. This difference between Q-factors confirms a trade-off between the optimization criteria involved in the cost function (6.1).

The optimized antennas show common characteristics that depend on their electrical size. A few such characteristics are given as examples in the following
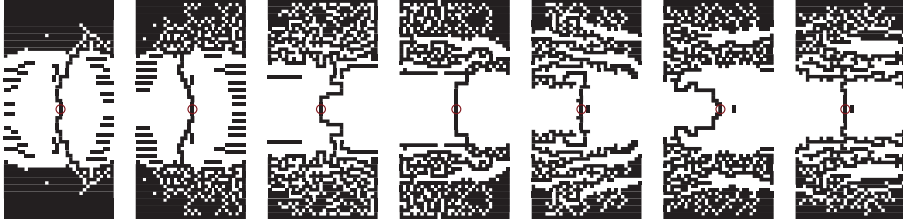
Figure 10: The structures simulated in ESI-CEM, [24], whose Q-factors are the smallest per $k\ell$-value in Fig. 9. The $Q_{Z'}$-factors (5.13) of these structures are depicted with circular marks in Fig. 9. Feeding edges are circled. From left to right— $k\ell = 0.1, 0.3, 0.5, 0.7, 0.9, 1.1, 1.3$.

considering Fig. 10. The structure with $k\ell = 0.1$ has: large metallic regions at the extremities in the ℓ-direction, little meandering that increases the longest current path, and w-aligned metallic strips which grow in length toward the extremities of the structure. The structure with $k\ell = 0.5$ is heavily meandered with many short metallic stubs along the meander; it has less metallic w-aligned strips. Larger structures are dominated by shorter meandering path and longer stubs.

6.2   2D Simplified Wireless Device Model

6.2.1   Optimization for Q and Resonance

The rectangular, simplified, wireless-device model with the dimensions $\ell/w = 2$ of Fig. 8b is considered. This model consists of an antenna (located within the black rectangle in the figure, *i.e.*, within the antenna region) embedded in a rectangular device (black and gray shading). The ground plane, gray shading in Fig. 8b, is considered fixed. The GA of Sec. 5.5 optimizes structures within the antenna region. Optimum currents are determined for each considered antenna design situation using the procedure described in Secs 4.3.1 and 4.3.4.

Two antenna design situations are investigated. In the first situation three dimensions of the antenna region are imposed while optimizing structures for minimum Q. These dimensions are 6 %, 15 % and 25 % of the structure area at one end in the ℓ-direction, as in Fig. 8b. The second situation considers GA optimization for Q or resonance for two feeding positions on the borderline between the antenna region and ground plane. The Q-factors of GA-optimized antennas are compared with the Q-factors of corresponding D/Q-optimum current distributions in Fig. 11. Examples of optimized antennas obtained in the above mentioned situations are depicted in Fig. 12. The two design situations mentioned above lead to six distinct combinations of antenna region size, optimization target, and feed position. These combinations are: 6 %-antenna region optimization for Q of structures fed to the side of the rectangular model in the w-
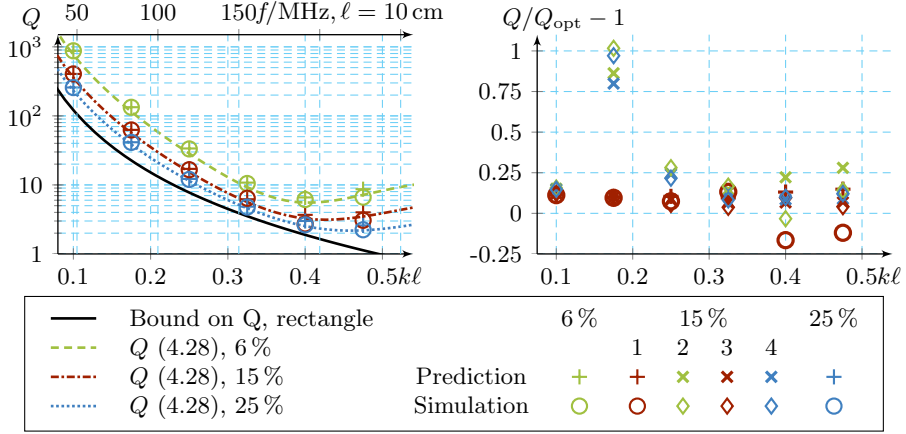
Figure 11: GA-optimized antenna Q-factors, labeled "Prediction", compared with Q-factors (4.28), denoted Q_{opt} to the right, of D/Q-optimum current distributions (see Sec. 4.3.1). The physical bound on Q for a rectangular, infinitely thin, PEC sheet [37, 38] is included for illustration. The $Q_{\mathrm{Z}'}$-factors (5.13) of the structures having the Q-factors "Prediction" are labeled "Simulation" because the former are computed from ESI-CEM [24] simulation data. Antenna regions extend $6\,\%$, $15\,\%$ and $25\,\%$ of the model area, as in Fig. 8b. The cases $6\,\%$, $15\,\%$–1 and $25\,\%$ are structures optimized for minimum Q, fed at the side of the rectangular model in the w-direction. The case $15\,\%$–2 represents structures optimized for resonance fed, at the side. The cases $15\,\%$–3 and $15\,\%$–4 are structures fed at the center of the rectangular model in the w-direction, optimized for minimum Q and resonance, respectively.

direction, $15\,\%$-antenna region optimization for Q side feed, $15\,\%$-antenna region optimization for resonance side feed, $15\,\%$-antenna region optimization for Q of structures fed in the center of the rectangular model in the w-direction, $15\,\%$-antenna region optimization for resonance center feed, and $25\,\%$-antenna region optimization for Q side feed. The six combinations correspond to the pairs of values "Prediction" and "Simulation" for each electrical size in Fig. 11, and to the rows of example antennas in Fig. 12.

The discretization of the model (antenna region and ground plane, as described in Sec. 4.3.4) has $N_\ell = 96$ and $N_w = 48$ elements in the ℓ and w-directions, respectively. The frequencies are chosen such that the electrical dimensions of the resulting device are in the range $\ell/\lambda \in [0.1, 0.5]$. These frequencies are between $300\,\mathrm{MHz}$ and $1.5\,\mathrm{GHz}$ for an $\ell = 10\,\mathrm{cm}$ device. The structures are fed by a voltage gap such that their far field is mainly linearly polarized in the ℓ-direction.

The procedure described in Sec. 4.3.4 is applied to the initial MoM matrices, *e.g.*, $\mathbf{Z}$, $\mathbf{X}_{\mathrm{e}}$, *etc.* These initial matrices have 9072 rows (and 9072 columns for square matrices). The mother matrices that the GA algorithm manipulates, *i.e.*, the matrices in parentheses in (4.37)–(4.41), have 570, 1330 and 2280 rows (and
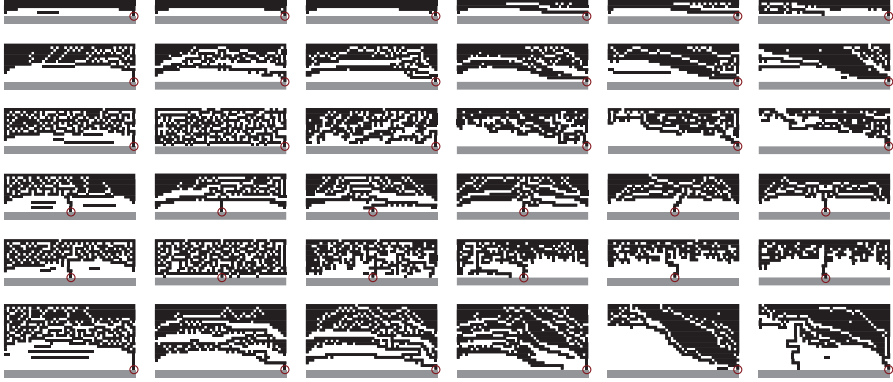
Figure 12: Antenna regions of the structures whose Q-factors are depicted in Fig. 11. Each structure has a Q-factor labeled "Prediction" and a $Q_{Z'}$-factor labeled "Simulation" in Fig. 11. Shaded—part of the ground plane. Feeding edges are circled. The rows from top to bottom correspond to the columns 6 %, 15 %–1, 15 %–2, 15 %–3, 15 %–4 and 25 % in the legend of Fig. 11.

the same number of columns for square matrices) when the antenna region occupies 6 %, 15 % and 25 % of the structure length. The genetic algorithm used here has the same parameters as that used in Sec. 6.1. The cost function minimized by the optimization algorithm is (6.1) with $\alpha_Q = 10$ and $\alpha_R = 1$ when optimizing for minimum Q, and $\alpha_Q = 1$, $\alpha_R = 10$ when optimizing for resonance.

The GA has been run five times for each frequency and combination of antenna region size, optimization target, and feed position. The antennas with the minimum Q-factor in the five runs, labeled "Prediction" in Fig. 11, have been simulated with the commercial electromagnetic solver ESI-CEM [24]. The input impedance computed by this solver is used to evaluate the $Q_{Z'}$-factors labeled "Simulation" in this figure. The single-resonance model [35, 110] was used to compute the $Q_{Z'}$ (5.13) for $\ell/\lambda = 0.1, 0.175$ and 0.25. The multiple-resonance Brune synthesis model [106] was employed to evaluate $Q_{Z'}$ when $\ell/\lambda = 0.325, 0.4$ and 0.475.

The convex optimization formulation (4.26) was used to derive the dashed, dash-dotted and dotted lines in Fig. 11. The directivity vector **F** is evaluated in the direction normal to the plane of the rectangular model.

It is observed in Fig. 11 that both the optimization prediction and the simulation Q-values follow closely the Q-factors of optimum current densities for small electrical dimensions. The relative deviation of these values from corresponding optimum-current Q is smaller than 20 %. When the electrical sizes of the structures increase, the values resulted from simulation data deviate from predicted values. One reason for this deviation is the Q-factor estimation procedure from the input impedance. Small Q-values are estimated less accurately when multiple closely spaced resonances are present around the frequency of interest.
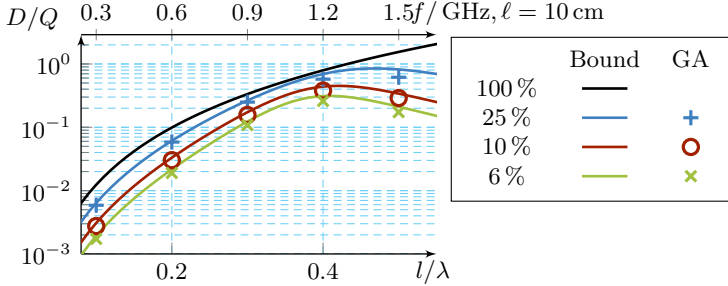
Figure 13: GA-optimized antenna D/Q-ratios (4.22), marks, compared with physical bounds on D/Q (4.24) for a rectangular wireless device model in which the antenna may occupy 6 %, 10 % and 25 % of the device at one end, see Fig. 8. The physical bound on the D/Q-ratio of a rectangular, infinitely-thin, PEC sheet [37–39] is labeled "100 %".

Common geometrical features can be observed in Fig. 12. Such features are metallic strips parallel to the ground plane, meandering, stubs extending from the meandered path, short circuits to the ground resembling a planar inverted-F antenna (PIFA) structure, *etc.*

6.2.2   Optimization for D/Q

The simplified model of Fig. 8b with the dimensions $\ell/w = 2$ is used to optimize structures in the antenna region that maximize the D/Q ratio. A simulation setup similar to that of Sec. 6.2.1 is used, with a uniform, $N_\ell = 96$ and $N_w = 36$-element mesh. The structures in the antenna region are considered fed on the borderline with the ground plane, at the side of the model in the w-direction. The antenna region extends 6 %, 10 % and 25 % of the model surface, at one end in the ℓ-direction. The GA is run five times for each combination of electrical size and antenna region extent. The maximum D/Q-value obtained in the five runs for each frequency is labeled "Prediction" in Fig. 13. The convex optimization formulation (4.26) is used to derive physical bounds on the D/Q-ratio for the antenna region sizes considered. These physical bounds (4.24) are depicted with solid colored lines in Fig. 13. The physical bound on D/Q [37, 38] is included in this figure for illustration. The antenna regions of the structures whose D/Q-ratios are marks in Fig. 13 are depicted in Fig. 14.

6.2.3   Optimization for Multiband Operation

The simplified 2D model of Fig. 8b is considered for simultaneous multiband Q-factor (4.19) optimization by the GA/MoM procedure described in Sec. 5.5. The parameters of the GA are similar to those used in Sec. 6.2.1. The dimensions of the model are $\ell \times w = 13 \times 6.5\,\mathrm{cm}^2$, common to hand-held wireless
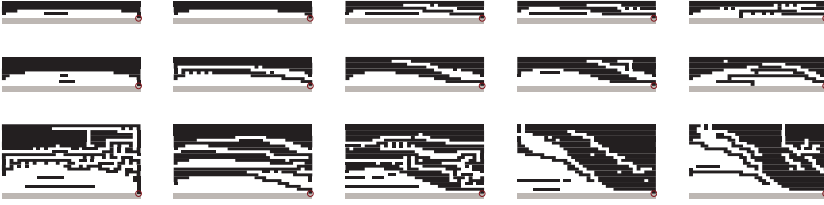
Figure 14: Black—ntenna regions of the structures whose D/Q-ratios are depicted as marks in Fig. 13. Gray shaded—part of the ground plane. Circled—feeding edges.

communication devices. The optimized structures are simulated using the commercial electromagnetic solver ESI-CEM [24]. The input impedance computed by this solver is used in BetaMatch [8] to design matching networks, using real component models, appropriate for multiband operation. These networks have the minimum number of components yielding less than $-6\,$dB throughout the considered frequency bands.

The model is discretized using a uniform, $N_\ell = 120$ by $N_w = 60$-square-element mesh. The MoM matrices, $e.g.$, $\mathbf{Z}$, $\mathbf{X}_e$, $etc.$, have 14220 rows (and the same number of columns for square matrices). Three sizes of the antenna region are considered: 20 %, 15 % and 10 % of the model at one end in the ℓ direction, as in Fig. 8b. The matrices manipulated by the GA have 2856, 2142 and 1428 rows (and the same number of columns for square matrices) respectively for the three sizes of the antenna region, see Sec. 4.3.4. These matrices are computed for the center frequencies of the bands 699 – 746, 880 – 960 and 1710 – 1990 MHz. The electrical size of the model at these center frequencies is $k\ell \approx 1.97, 2.5$ and 5.04 ($\ell/\lambda \approx 0.3, 0.4$ and 0.8). Three fixed feeding locations are considered for each antenna region size. These are located on the borderline between the ground plane and antenna region, to the side of the model in the w-direction, in the middle and half way between the side and middle, $i.e.$, approximately $0.54\,$mm, $16.8\,$mm, and $32\,$mm from the side in the w-direction, respectively.

The genetic algorithm described in Sec. 5.5 minimizes the objective function

$$F_{\mathrm{C}} = \max\left\{\frac{Q_1}{16}, \frac{Q_2}{12}, \frac{Q_3}{7}\right\} + 0.1\left(\frac{Q_1}{16} + \frac{Q_2}{12} + \frac{Q_3}{7}\right), \qquad (6.2)$$

where Q_1, Q_2 and Q_3 are the Q-factors of the radiating structures at the center frequencies of the considered bands, and the normalization values 16, 12 and 7 are computed with (3.7) for less than $-6\,$dB reflection coefficient magnitude at the antenna input in all frequency bands [110]. The GA has been run five times for each of the nine combinations of antenna region size and feed position. The optimized antenna regions of the structures with the smallest objective function (6.2) per such combination are depicted in Fig. 15. The structures fed half-way between the side and center of the w-dimension have the smallest objective function
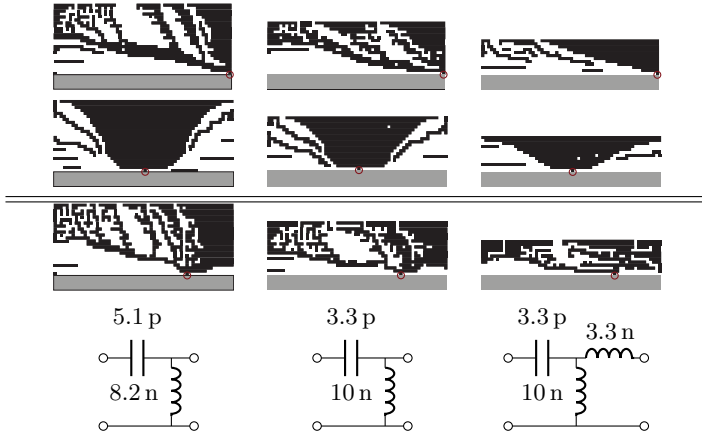
Figure 15: Antenna regions, black, of structures optimized for simultaneous multiband minimum Q. Circled—fed mesh edges on the borderline between antenna region and ground plane, at the side of the model in the w-direction (first row from the top), in the center (second row), and half way between center and side (third row). Bottom row—matching networks for the structures on the third row from the top, in SI units. Gray shaded—part of the ground plane. From left to right columns correspond to antenna regions extending $20\,\%$, $15\,\%$, and $10\,\%$ of the entire device model, at one end in the ℓ-direction, as depicted in Fig. 8b.

for each antenna region size. The amplitudes of the reflection coefficients at the input of these half-way fed structures, with and without the matching networks of Fig. 15, are depicted in Fig. 16. The matching networks yield less than $-6.5\,\mathrm{dB}$ reflection coefficient magnitude throughout all frequency bands.

6.3   3D Simplified Wireless Device Model

6.3.1   Optimization for Q

The 3D simplified model of some hand-held wireless devices illustrated in Fig. 8c is used to optimize structures in the antenna region for minimum Q. This optimization is performed using the GA/MoM procedure described in Sec. 5.5. The genetic algorithm is similar to that used in Sec. 6.2.1. The stop condition of this algorithm is a maximum number of $2\,10^5$ evolution steps reached or genetic stability during $2\,10^4$ steps, whichever event occurs first. Optimum current densities in the sense of the D/Q-ratio are derived using the convex optimization formulation (4.25) for polarization along ℓ and far-field direction ℓ_3.

The model illustrated in Fig. 8c consists of three rectangular regions connected together as in the figure. The first region, a fixed ground plane, has the length ℓ_1 and width $w = 7\,\mathrm{cm}$. The second and third rectangular regions, with the lengths ℓ_2 and $\ell_3 = 0.7\,\mathrm{cm}$, respectively, and width w, represent the antenna
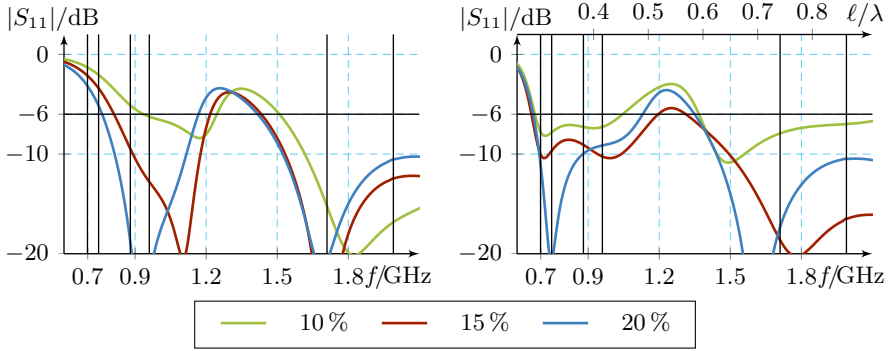
Figure 16: Left—magnitude of the reflection coefficient at the input of the structures with antenna regions depicted in Fig. 15, third row from the top. Right—magnitude of the reflection coefficient at the input of the matching networks of Fig. 15 terminated with the corresponding half-way-fed structures of Fig. 15. The curves correspond to antenna regions extending 10 %, 15 % and 20 % at one end of the structure length as in Fig. 8b.

region. The lengths ℓ_1 and ℓ_2 are chosen such that $\ell_1 + \ell_2 = \ell = 14$ cm. The region with the length ℓ_3 extends in a direction perpendicular to the common plane of the other two regions. Three configurations of the antenna region are considered, where $\ell_2 = 0.7$ cm, 1.4 cm and 2.8 cm, *i.e.*, 5 %, 10 % and 20 % of ℓ, respectively. The model is discretized with a non-uniform mesh, finer in the antenna region than in the ground plane. In order to have a single mesh, the first 11.2 cm in the ℓ-direction from the left in Fig. 8c are divided in 40 mesh elements (and 25 in the w-direction). The remaining 2.8 cm in the ℓ-direction are divided in 20 mesh elements (and 50 in the w-direction). The bent region is divided in 5 by 50 mesh elements in the ℓ_3 and w directions, respectively. This particular choice of discretization results in square mesh elements with the side 1.4 mm in the antenna region and 2.8 mm in the ground plane. A row of overlapping basis functions in the ℓ-direction at the place of the discontinuity in the mesh size couples electrically the regions with different discretizations. The matrices describing the entire model have 4435 rows. The matrices manipulated repetitively by the GA have 990, 1485 and 2475 rows respectively for $\ell_2 = 0.7$ cm, 1.4 cm and 2.8 cm. Square matrices have the same number of columns as the number of rows.

The GA optimization of structures in the antenna region for minimum Q has been performed for the five frequencies given by $\ell/\lambda = 0.1, 0.2, 0.3, 0.4,$ and 0.5. Five optimized structures have been generated by the GA for each combination of ℓ_2 and frequency. The smallest optimized-structure Q-factor (4.19) of the five corresponding to each combination of ℓ_2 and frequency is labeled "Pred." in Fig. 17. The optimized structures with these smallest Q-factors (of which nine are depicted in Fig. 18) have been simulated using the commercial solver
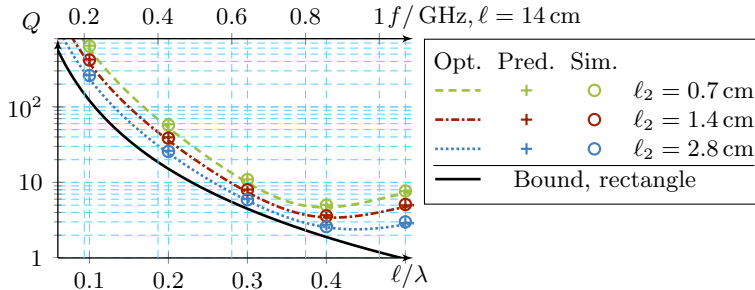
Figure 17: Q-factors of antennas optimized using a GA, "Pred.", compared to corresponding Q-factors (4.28) of D/Q-optimum current densities, "Opt.", for the bent-end model illustrated in Fig. 8c with $\ell_2 = 0.7\,\mathrm{cm}$, $1.4\,\mathrm{cm}$ and $2.8\,\mathrm{cm}$ and $\ell = 14\,\mathrm{cm}$. The input impedance of the GA-optimized structures, computed by ESI-CEM [24], has been used to calculate the Q-factors "Sim.". The physical bound on Q for a rectangular, infinitely thin, $14 \times 7\,\mathrm{cm}^2$, PEC sheet is depicted in solid black line [37, 38].

ESI-CEM, [24]. The input impedance of these structures is used to obtain the Q-factors labeled "Sim." in Fig. 17. These Q-factors agree to a large extent with those obtained using the in-house MoM solver and the discrete expression (4.19) (less than $6\,\%$ deviation relative to the former Q values). The single-resonance model (5.13), is employed to compute the Q-factor for $\ell/\lambda = 0.1$ and 0.2. The Q-factors for the other frequencies are computed using the multiple-resonance, Brune-synthesis model, [106]. The single-frequency $Q_{\mathrm{Z}'}$ estimation procedure described in Sec. 5.2 has been applied to the structures having the smallest Q-factors mentioned above. The $Q_{\mathrm{Z}'}$ (5.26) values in these cases have less than $5\,\%$ difference relative to corresponding $Q_{\mathrm{Z}'}$ values computed using (5.13).

The Q-factors obtained in optimization and simulation, as decribed in the previous paragraph, are compared to Q-factors given by optimum antenna current distributions, labeled "Opt." in Fig. 17. These distributions are obtained using the convex optimization formulation (4.26) for the D/Q-quotient, [36]. The matrices involved in these formulations are square with 990, 1485 and 2475 rows respectively for $\ell_2 = 0.7\,\mathrm{cm}$, $1.4\,\mathrm{cm}$ and $2.8\,\mathrm{cm}$. These matrices are obtained using a uniform, $1.4\,\mathrm{mm}$-side square mesh element discretization of the model of Fig. 8c. The physical bound on the Q-factor of a rectangular PEC region with the dimensions $14 \times 7\,\mathrm{cm}^2$ computed using the results in [37, 38] is included for illustration. It is observed in Fig. 17 that the optimized-structure Q-factors are close to those achieved by optimum antenna currents (less than $13\,\%$ deviation relative to the optimum-current Q-factors). Note that the current distributions used to compute the curves labeled "Opt." in Fig. 17 are optimum in the sense of D/Q. The Q-factors computed from these distributions may not be optimum in the sense of the Q-factor. This may result in structures that are on the "wrong side" of the D/Q-optimum current Q-factor, $e.g.$, below the curves in Fig. 17.
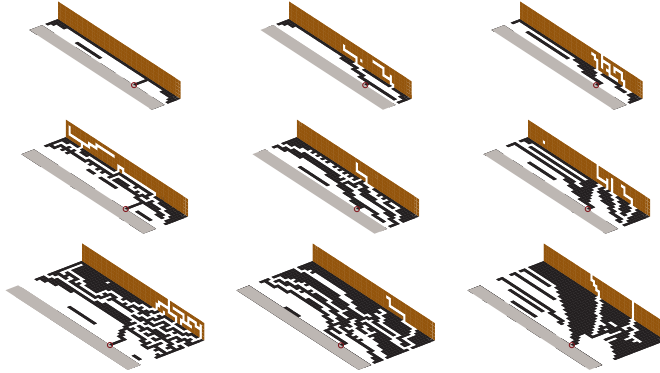
Figure 18: Example of genetic algorithm optimized structures (gray shading—part of the ground plane, black—antenna region part coplanar with the ground plane, bronze— antenna region part normal to the ground plane) with Q-factors depicted in Fig. 17 for $\ell/\lambda = 0.1$ (left column), 0.3 (middle column) and 0.5 (right column), and $\ell_2 = 0.7\,\mathrm{cm}$ (top row), 1.4 cm (middle row), and 2.8 cm (bottom row). Feeding edges are circled.

The D/Q-quotient of such structures is on the "right side" of the physical bound.

6.3.2   Optimization for Q, $Q_{\mathrm{Z}'}$, and Both

The bent-end model with $\ell_1 = 12.6\,\mathrm{cm}$ and $\ell_2 = 1.4\,\mathrm{cm}$, described in Sec. 6.3.1, is optimized using the GA/MoM procedure of Sec. 5.5 for operation between 700 MHz and 960 MHz. This frequency band is divided in two sub-bands with the center frequencies $f_{\mathrm{c},1} = 759.5\,\mathrm{MHz}$ and $f_{\mathrm{c},2} = 889.5\,\mathrm{MHz}$, The fractional bandwidths of the two sub-bands are equal, $\mathrm{FBW}_{1,2} \approx 15.8\,\%$. The matrices $\mathbf{Z}$ (5.1), $\mathbf{X}_{\mathrm{e}}$ (5.6), $\mathbf{X}_{\mathrm{m}}$ (5.7) and $\mathbf{R}_{\mathrm{r}}$ (5.8) are computed for the center frequencies. Two extra impedance matrices are computed for the frequencies $1.001 f_{\mathrm{c},1,2}$ in order to evaluate $Q_{\mathrm{Z}'}$ at $f_{\mathrm{c},1,2}$ using (5.13). The cost function minimized by the genetic algorithm is

$$F_{\mathrm{C}} = \alpha_{\mathrm{Q,M}} \max\left\{ \frac{Q_1}{7} + \frac{Q_2}{7} \right\} + \alpha_{\mathrm{Q,S}} \left(\frac{Q_1}{7} + \frac{Q_2}{7} \right)$$
$$+ \alpha_{\mathrm{Q_{Z'},M}} \max\{ Q_{\mathrm{Z}',1} + Q_{\mathrm{Z}',2} \} + \alpha_{\mathrm{Q_{Z'},S}} \left(Q_{\mathrm{Z}',1} + Q_{\mathrm{Z}',2} \right), \quad (6.3)$$

where the indices 1 and 2 denote the sub-band, Q is the energy-based antenna Q (4.19), $Q_{\mathrm{Z}'}$ is the single-resonance, input-impedance-derivative antenna Q (5.13), and the weights α define the optimization target. The normalization of Q by 7 is obtained from (3.7) for $-6\,\mathrm{dB}$ reflection coefficient magnitude at the antenna input for the targeted FBW, under the assumption of single-resonance [110]. The $Q_{\mathrm{Z}'}$ values are not normalized because some applications target as low $Q_{\mathrm{Z}'}$ as possible, *i.e.*, little variation of the input impedance in the operation band.

Target	$\alpha_{Q,}$		$\alpha_{Q_{Z'},}$		Q_1	Q_2	$Q_{Z',1}$	$Q_{Z',2}$
	M	S	M	S				
1	min Q	1	0.1	0	0	4.6	3.7	2.9	0.3
2	min $Q_{Z'}$	0	0	1	0.1	8.2	8.9	0.01	0.01
3	min Q & $Q_{Z'}$	1	0.1	1	0.1	8.7	6.8	0.08	0.08
4						6.5	5.5	1.1	1.1

Table 1: Parameters used in the cost function (6.3) to optimize the model of Fig. 8c for minimum Q (4.19), row 1, for minimum $Q_{Z'}$ (5.13), row 2, and both Q and $Q_{Z'}$, rows 3 and 4. The resulting Q and $Q_{Z'}$-values are included for the structures of Fig. 19.
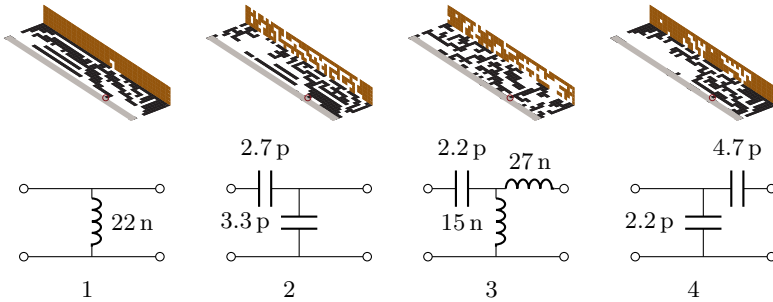
Figure 19: Top row—GA-optimized structures whose Q-factors are listed in Table 1. Gray shading—part of the ground plane, black—antenna region part coplanar with the ground plane, bronze—antenna region part normal to the ground plane. Feeding edges are circled. Middle row—matching networks with component values in SI units designed for the corresponding structures whose antenna regions are depicted on the top row. Bottom row—row index in Table 1.

The GA has been run five times for each optimization target whose α-values are listed in Table 1. The Q-factors of the four GA-optimized structures depicted in Fig. 19 (of the total 15 structures) are presented in the same table. The structures corresponding to rows 1, 2 and 3 have the minimum cost function. The structure whose Q-factors are listed on row 4 has been optimized for simultaneous minimum Q and $Q_{Z'}$, does not have the minimum cost function, but has minimum Q on both sub-bands (out of the total 5 GA-optimized structures with this target). The values for $Q_{Z'}$ listed in Table 1 are evaluated with (5.13). These values agree to a large extent with the same values reevaluated at the center frequencies with (5.26). The four structures of Fig. 19 have been simulated in ESI-CEM [24]. The magnitudes of the reflection coefficients at the inputs of these structures are depicted in Fig. 20. Matching networks that yield less than $-6\,\mathrm{dB}$ reflection coefficient in the entire band have been designed using BetaMatch [8]. These networks are depicted in Fig. 19 and the resulting S_{11} magnitudes in Fig. 20. Real component models of SMD lumped elements, including losses, have been used for matching.
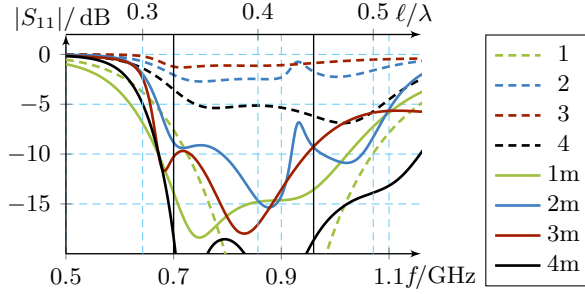
Figure 20: 1, 2, 3, 4—magnitudes of the S_{11} parameter at the input of the corresponding structures depicted in Fig. 19. 1m, 2m, 3m, 4m—magnitudes of the S_{11} parameter at the input of the matching networks of Fig. 19 terminated with the corresponding structures depicted on the first row in Fig. 19.

6.4 Wireless Terminal Antenna Placement Analysis Using Optimum Currents

Optimum antenna currents can be employed for evaluation and comparison of the performance achievable by a device with antennas placed at different locations. For illustration, we would like to determine the position and shape of the antenna region that has the smallest Q-factor in the frequency range given by $\ell/\lambda \in [0.05, 0.5]$. The nine 3D simplified models of common hand-held wireless terminals depicted in Fig. 21 are analyzed. One of these models is sketched in Fig. 8d. These models are limited to a rectangular parallelepiped with the dimensions $\ell \times w \times h = 14 \times 7 \times 0.7\,\mathrm{cm}^3$. Note that limiting the structures to a parallelepiped is introduced for illustration purpose and does not restrict the applicability of the procedure exemplified here. Each model is drawn in Fig. 21 to scale in three side views from the ℓ, w and h-directions (except for Fig. 21h where an h-side view and two sections through the symmetry planes are depicted). Gray and black represent the ground plane and antenna region, respectively. The thickness of the infinitely thin PEC material is exaggerated.

The ground plane consists of an infinitely thin planar PEC sheet that covers 90 % of the area of one $\ell \times w$ face of the parallelepiped bounding the model. The remaining 10 % of that face represents the support of the antenna region, which may be continuous or divided in more sub-regions. Here, a maximum of two sub-regions have been used. The structures in the antenna regions are limited to infinitely thin PEC sheets placed on faces of the 3D shape of the antenna region. This shape is obtained by translating the 10 % of the $\ell \times w$-face area reserved for the antenna region a distance h perpendicularly to the ground plane (*i.e.*, by extruding the 10 % in the h-direction to the opposed face). The shapes resulting in the antenna region are made of rectangular parallelepipeds. These parallelepipeds are covered with PEC sheets on the four largest-area faces (in the

Figure 21: Nine simplified wireless-device models limited to a parallelepiped. Three side views are depicted for a-g and i, *i.e.*, structures as seen along the length, width and height. A side view along the height and two sections at the symmetry planes are depicted for h. Gray shading—ground plane; black—antenna region.

Struct.	a	b	c	d	e, f	g	h	i
N	7584	8256	7568	7584	8256	8256	10830	7584
N_{AR}	1936	2608	1928	1944	2616	2612	5168	1992

Table 2: Dimensions of MoM matrices for the structures of Fig. 21. N—total number of basis functions. N_{AR}—number of basis functions in the blocks corresponding to the antenna region, see Sec. 4.3.4.

case depicted in Fig. 21h there are four openings adjacent to the ground plane corners in the $w \times h$-plane; these are one mesh-element wide and extend the entire h-dimension).

The antenna region placement situations introduced above are discretized using a uniform mesh of $1.75 \times 1.75\,\mathrm{mm}^2$ square elements. The total number of basis functions, N, resulting for the structures depicted in Fig. 21 are presented in Table 2 (*i.e.*, the number of rows and columns, where applicable, of $\mathbf{Z}$, $\mathbf{Z}'$, $\mathbf{X}_\mathrm{e}$, $\mathbf{X}_\mathrm{m}$, $\mathbf{R}_\mathrm{r}$, and $\mathbf{F}$). The same table presents the number of rows, and columns where applicable, N_{AR}, of the blocks corresponding to the $10\,\%$-$\ell \times w$-area antenna region, see Sec. 4.3.4. These blocks are computed for the matrices involved in the convex optimization formulation (4.26).

The bounds on D/Q using the convex optimization formulation (4.26) for the simplified models of Fig. 21 are depicted in Fig. 22. Linear polarization along the length and directivity in the direction of the height of the parallelepiped bounding the models are considered. The D/Q-optimum current distributions giving the physical bounds on D/Q of Fig. 22 have the Q-factors (4.28) depicted in the same figure. The bounds on D/Q and Q computed using the results in [37–39] for a rectangular, infinitely thin, $14 \times 7\,\mathrm{cm}^2$ PEC sheet are labeled "R" in this figure. The ring structure depicted in Fig. 21h outperforms all other structures in the figure in terms of D/Q and Q, except for a frequency region around $\ell/\lambda \approx 0.1$ where the structure in Fig. 21b has a greater D/Q. We also note that around $\ell/\lambda \approx 0.37$ a few of the structures in Fig. 21 reach close to the D/Q bound of a
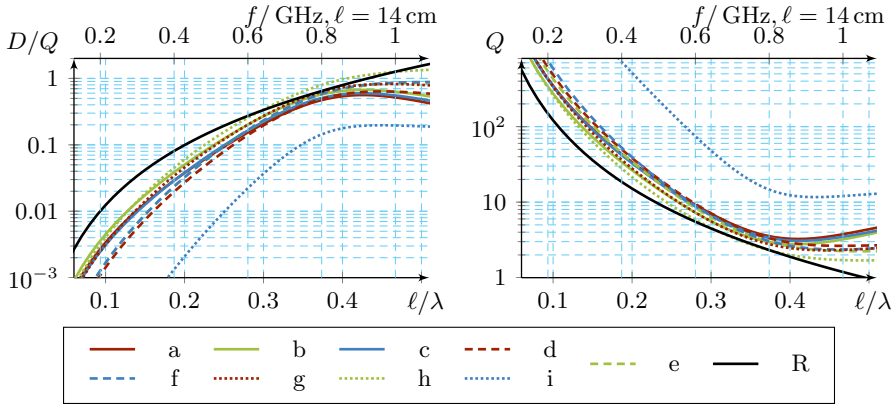
Figure 22: Left—physical bounds on D/Q for the structures depicted in Fig. 21 obtained using the convex optimization formulation (4.26) when only the antenna region (black in Fig. 21) is optimized. Right—Q-factors (4.28) of the D/Q-optimum current densities giving the curves to the left. The physical bounds on D/Q and Q for a rectangular PEC surface $14 \times 7\,\mathrm{cm}^2$, [37–39], is depicted in solid black line and labeled "R".

rectangular region and the structure in Fig. 21h has a D/Q value greater than that of a rectangular region. The optimum-current Q-factors do not reach as close to the physical bound on Q for a rectangular region as the D/Q-values.

7   Contributions of the Author

The work reported in this thesis and papers herein contributes to the field of antenna theory and design two things, in the author's view:

> It proposes a method to estimate the bandwidth of antennas, using Q or $Q_{\mathrm{Z'}}$ and a resonance model, from a current distribution computed at a single frequency.

> It applies the concepts of physical bounds and optimum currents to planar and 3D antenna design situations.

Paper I introduces a method to compute antenna Q-factors from single frequency current distributions. Based on a resonance model, the bandwidth of an antenna can be estimated by simulating the antenna at a single frequency. This single-frequency method is applied to antenna optimization in two design situations. These situations are the optimization of antennas limited to rectangular regions, and the optimization of a part of a rectangular, simplified wireless device model. In addition to the Q-factor estimation method, in this paper the concept of optimum antenna currents is applied to the study and design of antennas in

the two considered situations. The author of this thesis is the main contributor
to Paper I. He has derived antenna quantities needed in the study, implemented
their computation in MATLAB, set up and run simulations, collected results,
and written the paper and drawn the conclusions.

Paper II is an extension of Paper I to a new design situation, antennas that
operate on multiple frequency bands. The author of this thesis is the main
contributor to this paper. He has set up and run simulations, collected results,
and written the paper and drawn the conclusions.

Paper III introduces a method to estimate $Q_{\mathrm{Z'}}$ from a single-frequency cur-
rent distribution. This method is verified in all situations illustrated in the pa-
per. In addition to introducing the $Q_{\mathrm{Z'}}$ estimation method, Paper III illustrates
the application of the theory presented in Paper I to the study of 3D radiating
structures, optimization for Q, $Q_{\mathrm{Z'}}$ and both Q and $Q_{\mathrm{Z'}}$, and antenna-in-device
location optimization using optimum currents and physical bounds. The author
of this thesis is the main contributor to Paper III. He has derived the single-
frequency $Q_{\mathrm{Z'}}$ estimation method, implemented its computation in MATLAB,
set up and run simulations, collected results, and written the paper and drawn
the conclusions.

Paper IV presents a study of physical bounds on the antenna D/Q quotient
using an optimization formulation. The author of this thesis has contributed
in the verification of the theory presented in this paper, including the study
related to the negative stored energy. He has designed the spherical and strip
dipole antennas, collected data related to them and written a description of this
verification, included in the paper.

Paper V is a study of the generalized, or all spectrum, absorption efficiency.
The author of this thesis has performed the numerical examples included in the
paper and written the section about them.

8   Conclusions

The single-frequency estimation procedures for antenna parameters described in
Secs 4.2 and 5.2 have potential applications mainly in, but not limited to, au-
tomatic optimization. A significant reduction of time may be achieved in the
optimization process of antenna parameters such as Q-factor and bandwidth for
some radiating structures using these procedures. Single-frequency expressions
such as (4.11)–(4.14), (4.19), or (5.26) can be easily integrated in standard MoM
solvers, as illustrated in Secs 5.1 and 5.2. Such an integration does not add a
significant temporal overhead to the standard computation because most quanti-
ties are already computed by such standard MoM solvers. The single-frequency
derivations presented in this thesis are based on the expressions for the ener-
gies stored in the fields generated by an antenna derived in [100] and evaluated
following the procedure in [36, 40].

Optimum current densities can be used to express physical limitations for

structures of arbitrary complexity without assuming a bounding geometry such as a sphere, cylinder, *etc.* Such physical bounds, derived as illustrated in Sec. 4.3, can be applied in the process of antenna design to assess feasibility and performance of some structures in realistic conditions. The examples presented in this thesis use the discretized energy expressions (4.11)–(4.14) to derive optimum current distributions in the sense of D/Q, see Sec. 4.3.1. This derivation is performed by formulating adequate convex optimization problems as described in more detail in [11, 36].

9 Future Work

The methods and tools presented in this thesis can be extended to other situations. Such situations are multiple antenna systems, structures that include dielectric and/or magnetic materials, losses, automatic antenna-in-device location optimization, etc. Other situations are different numerical methods, apart from MoM, where discrete expressions such as (4.11)–(4.14) may provide new tools for the antenna engineer.

References

[1] K. B. Alici and E. Ozbay. Electrically small split ring resonator antennas. *Journal of Applied Physics*, **101**(8), 2007.

[2] E. Altshuler. Electrically small self-resonant wire antennas optimized using a genetic algorithm. *Antennas and Propagation, IEEE Transactions on*, **50**(3), 297–300, Mar 2002.

[3] Antenna Standards Committee of the IEEE Antennas and Propagation Society. IEEE Standard Definitions of Terms for Antennas, 1993. IEEE Std 145-1993.

[4] M. Avriel. *Nonlinear programming : analysis and methods.* Prentice-Hall series in automatic computation. Englewood Cliffs, New Jersey, 1976.

[5] S. R. Best, E. E. Altshuler, A. D. Yaghjian, J. M. McGinthy, and T. H. O'Donnell. An impedance-matched 2-element superdirective array. *Antennas and Wireless Propagation Letters, IEEE*, **7**, 302–305, 2008.

[6] S. Best. A Low Q Electrically Small Magnetic (TE Mode) Dipole. *Antennas and Wireless Propagation Letters, IEEE*, **8**, 572–575, 2009.

[7] S. R. Best. Low Q electrically small linear and elliptical polarized spherical dipole antennas. *IEEE Trans. Antennas Propagat.*, **53**(3), 1047–1053, 2005.

[8] MNW Scan, Singapore—BetaMatch, Software for antenna component matching. http://www.mnw-scan.com/.

[9] J. Bonnans, J. Gilbert, C. Lemaréchal, and C. Sagastizábal. *Numerical Optimization – Theoretical and Practical Aspects.* Universitext. Springer-Verlag, Berlin, 2006.

[10] C. Bouwkamp and N. De Bruijn. The problem of optimum antenna current distribution. *Philips Res. Rep*, **1**(2), 135–158, 1946.

[11] S. P. Boyd and L. Vandenberghe. *Convex Optimization.* Cambridge Univ Pr, 2004.

[12] M. Capek, L. Jelinek, P. Hazdra, and J. Eichler. The Measurable Q Factor and Observable Energies of Radiating Structures. *IEEE Trans. Antennas Propagat.*, **62**(1), 311–318, Jan 2014.

[13] C. J. Carpenter. Electromagnetic energy and power in terms of charges and potentials instead of fields. *IEE Proc. A*, **136**(2), 55–65, 1989.

[14] W. C. Chew, M. S. Tong, and B. Hu. *Integral equation methods for electromagnetic and elastic waves*, volume 12. Morgan & Claypool, 2008.

[15] W. C. Chew, E. Michielssen, J. Song, and J. Jin. *Fast and efficient algorithms in computational electromagnetics.* Artech House, Inc., 2001.

[16] L. J. Chu. Physical Limitations of Omnidirectional Antennas. *J. Appl. Phys.*, **19**, 1163–1175, 1948.

[17] M. Cismasu and M. Gustafsson. Antenna Bandwidth Optimization with Single Frequency Simulation. *IEEE Trans. Antennas Propagat.*, **62**(3), 1304–1311, 2014.

[18] M. Cismasu and M. Gustafsson. Multiband Antenna Q Optimization using Stored Energy Expressions. *IEEE Antennas and Wireless Propagation Letters*, **13**(2014), 646–649, 2014.

[19] R. E. Collin. *Field Theory of Guided Waves.* IEEE Press, New York, second edition, 1991.

[20] R. E. Collin and S. Rothschild. Evaluation of antenna Q. *IEEE Trans. Antennas Propagat.*, **12**, 23–27, January 1964.

[21] R. E. Collin. *Foundations for Microwave Engineering.* McGraw-Hill, New York, second edition, 1992.

[22] J. E. Dennis and R. B. Schnabel. *Numerical Methods for Unconstrained Optimization and Nonlinear Equations.* Prentice-Hall, Inc., Englewood Cliffs, New Jersey, 1983.

[23] C. L. Dolph. A current distribution for broadside arrays which optimizes the relationship between beam width and side-lobe level. *Proceedings of the IRE*, **34**(6), 335–348, June 1946.

[24] ESI Group, Paris, France—ESI Group's computational electromagnetic (CEM) solution. http://www.esi-group.com.

[25] R. L. Fante. Quality factor of general antennas. *IEEE Trans. Antennas Propagat.*, **17**(2), 151–155, March 1969.

[26] R. Fletcher. *Practical Methods of Optimization*. John Wiley & Sons, Ltd., Chichester, 1987.

[27] C. Floudas. *Deterministic Global Optimization*. Nonconvex Optimization and Its Applications. Springer-Verlag, 1999.

[28] H. D. Foltz and J. S. McLean. Limits on the radiation Q of electrically small antennas restricted to oblong bounding regions. In *IEEE Antennas and Propagation Society International Symposium*, volume 4, pages 2702–2705. IEEE, 1999.

[29] W. Geyi. A method for the evaluation of small antenna Q. *IEEE Trans. Antennas Propagat.*, **51**(8), 2124–2129, 2003.

[30] W. Geyi. Physical limitations of antenna. *IEEE Trans. Antennas Propagat.*, **51**(8), 2116–2123, August 2003.

[31] W. Geyi. *Foundations of Applied Electrodynamics*. John Wiley & Sons, 2011.

[32] P. E. Gill, W. Murray, and M. H. Wright. *Practical Optimization*. Academic Press, London, 1981.

[33] E. I. Green. The story of Q. *American Scientist*, **43**(4), pp. 584–594, 1955.

[34] M. Gustafsson, M. Cismasu, and S. Nordebo. Absorption efficiency and physical bounds on antennas. *International Journal of Antennas and Propagation*, **2010**(Article ID 946746), 1–7, 2010.

[35] M. Gustafsson and S. Nordebo. Bandwidth, Q-factor, and resonance models of antennas. *Progress in Electromagnetics Research*, **62**, 1–20, 2006.

[36] M. Gustafsson and S. Nordebo. Optimal antenna currents for Q, superdirectivity, and radiation patterns using convex optimization. *IEEE Trans. Antennas Propagat.*, **61**(3), 1109–1118, 2013.

[37] M. Gustafsson, C. Sohl, and G. Kristensson. Physical limitations on antennas of arbitrary shape. *Proc. R. Soc. A*, **463**, 2589–2607, 2007.

[38] M. Gustafsson, C. Sohl, and G. Kristensson. Illustrations of new physical bounds on linearly polarized antennas. *IEEE Trans. Antennas Propagat.*, **57**(5), 1319–1327, May 2009.

[39] M. Gustafsson. AntennaQ—MATLAB script that computes physical bounds on Q and D/Q for antennas. . http://www.mathworks.se/matlabcentral/fileexchange/26806-antennaq.

[40] M. Gustafsson, M. Cismasu, and B. L. G. Jonsson. Physical bounds and optimal currents on antennas. *IEEE Trans. Antennas Propagat.*, **60**(6), 2672–2681, 2012.

[41] M. Gustafsson and B. L. G. Jonsson. Stored electromagnetic energy and antenna Q. Technical Report LUTEDX/(TEAT-7222)/1–25/(2012), Lund University, Department of Electrical and Information Technology, P.O. Box 118, S-221 00 Lund, Sweden, 2012. http://www.eit.lth.se.

[42] R. C. Hansen. Fundamental limitations in antennas. *Proc. IEEE*, **69**(2), 170–182, 1981.

[43] R. C. Hansen. *Electrically small, superdirective, and superconductive antennas.* John Wiley & Sons, New Jersey, 2006.

[44] R. C. Hansen and R. E. Collin. *Small Antenna Handbook.* Wiley, 2011.

[45] T. V. Hansen, O. S. Kim, and O. Breinbjerg. Properties of sub-wavelength spherical antennas with arbitrarily lossy magnetodielectric cores approaching the Chu lower bound. *IEEE Trans. Antennas Propagat.*, **62**(3), 1456–1460, 2014.

[46] R. F. Harrington. Effect of antenna size on gain, bandwidth and efficiency. *Journal of Research of the National Bureau of Standards – D. Radio Propagation*, **64D**, 1–12, January – February 1960.

[47] R. Harrington. Characteristic modes for antennas and scatterers. In R. Mittra, editor, *Numerical and Asymptotic Techniques in Electromagnetics*, volume 3 of *Topics in Applied Physics*, pages 51–87. Springer Berlin Heidelberg, 1975.

[48] R. F. Harrington. *Field Computation by Moment Methods.* Macmillan, New York, 1968.

[49] R. L. Haupt and D. H. Werner. *Genetic Algorithms in Electromagnetics.* Wiley-IEEE Press, 2007.

[50] D. Hertog. *Interior Point Approach to Linear, Quadratic and Convex Programming.* Kluwer Academic Publishers, 1994.

[51] R. Horst, P. Pardalos, and N. Van Thoai. *Introduction to Global Optimization.* Nonconvex Optimization and Its Applications. Springer-Verlag, 2000.

[52] J. M. Jin. *Theory and Computation of Electromagnetic Fields.* Wiley, 2011.

[53] L. Jofre, M. Martinez-Vazquez, R. Serrano, and G. Roqueta. *Handbook on small antennas.* EurAAP, Bruxelles, 2012.

[54] M. John and M. Ammann. Wideband Printed Monopole Design Using a Genetic Algorithm. *Antennas and Wireless Propagation Letters, IEEE*, **6**, 447–449, 2007.

[55] J. M. Johnson and Y. Rahmat-Samii. Genetic algorithms and method of moments GA/MOM for the design of integrated antennas. *IEEE Trans. Antennas Propagat.*, **47**(10), 1606–1614, oct 1999.

[56] M. A. Khayat and D. R. Wilton. Numerical evaluation of singular and near-singular potential integrals. *IEEE Trans. Antennas Propagat.*, **53**(10), 3180–3190, October 2005.

[57] O. Kim, S. Pivnenko, and O. Breinbjerg. Superdirective magnetic dipole array as a first-order probe for spherical near-field antenna measurements. *IEEE Trans. Antennas Propagat.*, **60**(10), 4670–4676, 2012.

[58] O. Kim. Low-Q Electrically Small Spherical Magnetic Dipole Antennas. *Antennas and Propagation, IEEE Transactions on*, **58**(7), 2210–2217, July 2010.

[59] O. Kim. Minimum Q Electrically Small Antennas. *Antennas and Propagation, IEEE Transactions on*, **60**(8), 3551–3558, Aug 2012.

[60] O. Kim, O. Breinbjerg, and A. Yaghjian. Electrically Small Magnetic Dipole Antennas With Quality Factors Approaching the Chu Lower Bound. *Antennas and Propagation, IEEE Transactions on*, **58**(6), 1898–1906, June 2010.

[61] J. D. Kraus. *Antennas.* McGraw-Hill, New York, second edition, 1988.

[62] L. La Paz and G. Miller. Optimum current distributions on vertical antennas. *Proceedings of the IRE*, **31**(5), 214–232, May 1943.

[63] L. S. Lasdon. *Optimization Theory for Large Systems.* Dover Books on Mathematics. Dover Publications, 2002.

[64] G. Manara, A. Monorchio, and R. Mittra. Frequency selective surface design based on genetic algorithm. *Electronics Letters*, **35**(17), 1400–1401, Aug 1999.

[65] D. Margetis, G. Fikioris, J. M. Myers, and T. T. Wu. Highly directive current distributions: General theory. *Physical Review E*, **58**(2), 2531, 1998.

[66] D. T. Marius Cismasu and M. Gustafsson. Stored Energy Based 3D Antenna Analysis and Design. Technical Report LUTEDX/(TEAT-7231)/1-18/(2014), Lund Institute of Technology, 2014.

[67] J. S. McLean. A re-examination of the fundamental limits on the radiation Q of electrically small antennas. *IEEE Trans. Antennas Propagat.*, **44**(5), 672–676, May 1996.

[68] J. R. Mosig and F. E. Gardiol. A dynamical radiation model for microstrip structures. In P. W. Hawkes, editor, *Advances in Electronics and Electron Physics*, volume 59, pages 139 – 237. Academic Press, 1982.

[69] Y. Nesterov and A. Nemirovsky. *Interior Point Polynomial Methods in Convex Programming*, volume 13. Studies in Applied Mathematics, Society for Industrial and Applied Mathematics, Philadelphia, PA, 1994.

[70] J. Nocedal and S. J. Wright. *Numerical Optimization*. Operations Research and Financial Engineering. Springer-Verlag, New York, 2006.

[71] M. Ohira, H. Deguchi, M. Tsuji, and H. Shigesawa. Multiband single-layer frequency selective surface designed by combination of genetic algorithm and geometry-refinement technique. *IEEE Trans. Antennas Propagat.*, **52**(11), 2925–2931, Nov 2004.

[72] S. J. Orfanidis. Electromagnetic waves and antennas, 2002. Available online at www.ece.rutgers.edu/~orfanidi/ewa.

[73] A. F. Peterson, S. L. Ray, and R. Mittra. *Computational Methods for Electromagnetics*. IEEE Press, New York, 1998.

[74] M. Pioro and D. Medhi. *Routing, flow, and capacity design in communication and computer networks*. Morgan Kaufmann Publishers, 2004.

[75] D. M. Pozar. *Microwave Engineering*. John Wiley & Sons, New York, third edition, 2005.

[76] Y. Rahmat-Samii and E. Michielssen. *Electromagnetic Optimization by Genetic Algorithms*. Wiley Series in Microwave and Optical Engineering. John Wiley & Sons, 1999.

[77] M. Rhodes and B. Hyland. Electrically small antenna, November 9 2010. US Patent 7,830,318.

[78] H. Riblet. Note on the maximum directivity of an antenna. *Proceedings of the IRE*, **36**(5), 620–623, May 1948.

[79] A. Rinnooy Kan and G. Timmer. Stochastic global optimization methods part I: Clustering methods. *Mathematical Programming*, **39**(1), 27–56, 1987.

[80] A. Rinnooy Kan and G. Timmer. Stochastic global optimization methods part II: Multi level methods. *Mathematical Programming*, **39**(1), 57–78, 1987.

[81] J. Robinson and Y. Rahmat-Samii. Particle swarm optimization in electromagnetics. *IEEE Trans. Antennas Propagat.*, **52**(2), 397 – 407, feb. 2004.

[82] A. Ruszczyński. *Nonlinear optimization*. Princeton University Press, Princeton, New Jersey, 2011.

[83] M. Shahpari, D. Thiel, and A. Lewis. An Investigation Into the Gustafsson Limit for Small Planar Antennas Using Optimization. *IEEE Trans. Antennas Propagat.*, **62**(2), 950–955, Feb 2014.

[84] A. K. Skrivervik, J.-F. Zürcher, O. Staub, and J. R. Mosig. PCS antenna design: The challenge of miniaturization. *IEEE Antennas and Propagation Magazine*, **43**(4), 12–27, August 2001.

[85] A. K. Skrivervik. Implantable antennas: The challenge of efficiency. In *Antennas and Propagation (EuCAP), 2013 7th European Conference on*, pages 3627–3631. IEEE, 2013.

[86] A. K. Skrivervik and M. Gustafsson. Fundamental limitations. In L. Joffre, M. Martinez-Vasquez, R. Serrano, and G. Roquetta, editors, *Handbook on small antennas*, EurAAP seventh framework programme, pages 5–59. Universitat Politecnica de Catalunya, 2012.

[87] J. C.-E. Sten, P. K. Koivisto, and A. Hujanen. Limitations for the radiation Q of a small antenna enclosed in a spheroidal volume: axial polarisation. *AEÜ Int. J. Electron. Commun.*, **55**(3), 198–204, 2001.

[88] J.-E. Sten, A. Hujanen, and P. Koivisto. Quality factor of an electrically small antenna radiating close to a conducting plane. *Antennas and Propagation, IEEE Transactions on*, **49**(5), 829–837, May 2001.

[89] G. Strang. *Introduction to applied mathematics*. Wellesley-Cambridge Press, Box 157, Wellesley MA 02181, 1986.

[90] H. R. Stuart and A. Pidwerbetsky. Electrically small antenna elements using negative permittivity resonators. *IEEE Trans. Antennas Propagat.*, **54**(6), 1644–1653, 2006.

[91] H. Stuart, S. Best, and A. Yaghjian. Limitations in Relating Quality Factor to Bandwidth in a Double Resonance Small Antenna. *Antennas and Wireless Propagation Letters*, **6**, 2007.

[92] H. Stuart and A. Yaghjian. Approaching the Lower Bounds on Q for Electrically Small Electric-Dipole Antennas Using High Permeability Shells. *Antennas and Propagation, IEEE Transactions on*, **58**(12), 3865–3872, Dec 2010.

[93] M. Tanielian, R. Greegor, and C. Parazzoli. Electrically small antenna, October 4 2011. US Patent 8,031,128.

[94] H. L. Thal. New Radiation Q Limits for Spherical Wire Antennas. *IEEE Trans. Antennas Propagat.*, **54**(10), 2757–2763, October 2006.

[95] H. L. Thal. Gain and Q Bounds for Coupled TM-TE Modes. *IEEE Trans. Antennas Propagat.*, **57**(7), 1879–1885, July 2009.

[96] H. L. Thal. Q Bounds for Arbitrary Small Antennas: A Circuit Approach. *IEEE Trans. Antennas Propagat.*, **60**(7), 3120–3128, 2012.

[97] G. Thiele, P. Detweiler, and R. Penno. On the lower bound of the radiation Q for electrically small antennas. *IEEE Trans. Antennas Propagat.*, **51**(6), 1263–1269, June 2003.

[98] B. Thors, H. Steyskal, and H. Holter. Broad-band fragmented aperture phased array element design using genetic algorithms. *IEEE Trans. Antennas Propagat.*, **53**(10), 3280 – 3287, oct. 2005.

[99] F.-I. Tseng and D. K. Cheng. Optimum scannable planar arrays with an invariant sidelobe level. *Proceedings of the IEEE*, **56**(11), 1771–1778, Nov 1968.

[100] G. A. E. Vandenbosch. Reactive energies, impedance, and Q factor of radiating structures. *IEEE Trans. Antennas Propagat.*, **58**(4), 1112–1127, 2010.

[101] G. A. E. Vandenbosch. Simple procedure to derive lower bounds for radiation Q of electrically small devices of arbitrary topology. *IEEE Trans. Antennas Propagat.*, **59**(6), 2217–2225, 2011.

[102] J. Volakis, C. C. Chen, and K. Fujimoto. *Small Antennas: Miniaturization Techniques & Applications*. McGraw-Hill, New York, 2010.

[103] J. L. Volakis and K. Sertel. *Integral Equation Methods for Electromagnetics*. SciTech Publishing Inc., 2012.

[104] H. A. Wheeler. Fundamental limitations of small antennas. *Proc. IRE*, **35**(12), 1479–1484, 1947.

[105] H. Wheeler. The radiansphere around a small antenna. *Proceedings of the IRE*, **47**(8), 1325–1331, 1959.

[106] O. Wing. *Classical Circuit Theory*. Springer, New York, 2008.

[107] B. G. Xia, J. Meng, D. H. Zhang, and J. S. Zhang. PMM-GA method to synthesize quasi-optical frequency selective surface on SiO2 substrate. *Progress in Electromagnetics Research*, **139**, 599–610, 2013.

[108] A. D. Yaghjian, M. Gustafsson, and B. L. G. Jonsson. Minimum Q for lossy and lossless electrically small dipole antennas. *Progress In Electromagnetics Research*, **143**, 641–673, 2013.

[109] A. D. Yaghjian and H. R. Stuart. Lower bounds on the Q of electrically small dipole antennas. *IEEE Trans. Antennas Propagat.*, **58**(10), 3114–3121, 2010.

[110] A. D. Yaghjian and S. R. Best. Impedance, bandwidth, and *Q* of antennas. *IEEE Trans. Antennas Propagat.*, **53**(4), 1298–1324, 2005.

[111] X.-S. Yang. *Engineering Optimization*. John Wiley & Sons, 2010.

[112] R. Ziolkowski and A. Erentok. Metamaterial-based efficient electrically small antennas. *Antennas and Propagation, IEEE Transactions on*, **54**(7), 2113–2130, July 2006.

[113] R. Ziolkowski and A. Kipple. Application of double negative materials to increase the power radiated by electrically small antennas. *Antennas and Propagation, IEEE Transactions on*, **51**(10), 2626–2640, Oct 2003.

Antenna Bandwidth Optimization With Single Frequency Simulation

Paper I

Marius Cismasu and Mats Gustafsson

Abstract

A method to compute antenna Q using an electromagnetic simulation at a single frequency is described. This method can easily be integrated into global optimization algorithms. In this way the optimization time of some antenna parameters, *e.g.*, bandwidth, may be significantly reduced. The method is validated by direct comparison with the physical bound of the analyzed structure. Numerical examples for rectangular antennas and antennas with a rectangular ground plane illustrate the integration of the method into a genetic algorithm. The results predicted by optimization agree very well with those obtained using a commercial electromagnetic solver. These results suggest that the method can be used to yield antennas with Q-factors within 20 % of their corresponding physical bound.

1 Introduction

Antenna performance may be improved, when necessary, through global optimization algorithms. Mathematical considerations and examples of such algorithms are presented in [3, 5, 17]. Deterministic approaches are prohibitive for some antenna optimization problems due to the size and unpredictability of the solution space studied. However, heuristic methods, *e.g.*, genetic algorithms, particle swarm optimization, *etc.*, have provided reasonable solutions to such problems [13, 16, 21–23]. One parameter frequently included in antenna optimization goals is the bandwidth. This parameter is commonly evaluated from multiple frequency samples of the antenna input impedance. The computation of these samples accounts in general for the greatest part of the solution time of an optimization algorithm.

Here, we estimate the Q-factor from the current excited on an antenna computed at a single frequency. Using the results by Vandenbosch [24] and Geyi [4] we compute the electric and magnetic energies stored in the fields excited by an antenna and the radiated power. We assume the studied antennas are electrically small, *i.e.*, $Q \gg 1$, such that the error in the Q computation is negligible (equal to $ka \ll 1$ [11]). The previously introduced computation is performed following the procedure in [8, 10], at a single frequency, usually the center of the intended operating band. Considering the input impedance of antennas described by a resonance model [7, 26], the Q-factor can be used as a direct measure of the bandwidth. This approach for computing the Q-factor is implemented in a standard Method of Moments (MoM) code [8, 10]. The implementation requires minor modifications of the code and does not increase the computation time significantly.

This method is applied to antennas that may take arbitrary shapes within a rectangular region. A genetic algorithm (GA) with MoM simulation is implemented following the GA/MoM approach described in [16, 21, 23]. Using rectangular mesh elements, a mother impedance matrix is computed prior to launching the actual optimization. Similar "mother" matrices are computed at the same

time for the stored electric and magnetic energies and radiated power. This approach reduces the actual optimization process to finding the rows and columns of these mother matrices that give optimum performance. A more realistic situation is also considered that describes typical devices with limited space for antennas. Such situations resulting in large solution times can be more efficiently handled by imposing a block matrix decomposition as described in [16, 21]. The results are verified using the commercial electromagnetic solver Efield[1]. The agreement between the Q-factors resulting from optimization and simulation is very good.

Antenna performance is evaluated during optimization as a linear combination of three parameters. These parameters are the Q-factor, the difference between the stored electric and magnetic energies, and metallic area (all appropriately normalized). They have been chosen to illustrate the single frequency antenna Q computation method. Other important parameters such as losses, radiation resistance or matching are not considered here. The energy-difference mentioned above represents the quantitative measure of self-resonance used during optimization. This resonance was compared with the corresponding resonance of the input impedance obtained from the commercial solver Efield. The optimization-predicted and impedance self-resonance agree to a large extent, confirming the validity of the expressions in [4, 10, 11, 24].

Physical bounds can be used to evaluate the optimization solution quality and stop an optimization process. The performance of the structures considered here has been compared with the physical bounds for rectangular structures [6, 9, 10], and structures with a rectangular ground plane [8]. This comparison shows that the optimized structures perform close to their physical bounds. In addition the rectangular ground plane results verify the theory presented in [8].

The paper is organized as follows. The method to compute the Q-factor of antennas using a single frequency electromagnetic solution obtained from an MoM solver is described in Sec. 2. A possible integration of this method in a genetic rectangular antenna optimization algorithm is presented in Sec. 3.1. Further improvements to this algorithm for fixed pattern antennas are described in Sec. 3.2. The physical bounds used to compare the optimized antenna performance are described in Sec. 4. Section 5.1 describes the setup for the numerical simulations performed. Sections 5.2 and 5.3 present numerical results for rectangular antennas and antennas with a rectangular ground plane respectively. The paper ends with conclusions in Sec. 6.

---

[1]www.efieldsolutions.com

2 Computation of Antenna Q in the Method of Moments

The quality factor of a lossless antenna is defined as [26]

$$Q = \frac{2c_0 k \max\{W_e, W_m\}}{P_{\mathrm{rad}}}, \tag{2.1}$$

where c_0 is the speed of light in free space, k is the wave number, W_e and W_m are respectively the electric and magnetic energies stored in the fields excited by the antenna, and P_r is the power radiated by the antenna. This definition is valid both for resonant and non-resonant antennas. Equation (2.1) is equivalent to the definition in [1] for resonant antennas.

A resonance model can be used to describe many antennas, [7, 26]. This model allows an approximation that relates the input impedance behavior to the Q-factor of antennas:

$$Q_{Z'} = \frac{k_0 |Z'(k_0)|}{2R(k_0)}, \tag{2.2}$$

where k_0 is the resonance wave number, Z' is the first derivative with respect to the wave number of the input impedance (tuned to resonance), and R is the radiation resistance. Equation (2.2) requires the input impedance be known at least for two different frequencies. This multiple frequency requirement is not necessary for evaluating (2.1). In this case it suffices to know the stored energies and radiated power at a single frequency. From these single frequency quantities the bandwidth can be estimated based on its inverse proportionality to the Q-factor [26].

The stored electric and magnetic energies in (2.1) can be expressed using the results in [4, 24]. Here we consider, for simplicity, surface currents. The stored electric and magnetic energies are respectively $W_e = \mu_0 w^{(e)}/(16\pi k^2)$ and $W_m = \mu_0 w^{(m)}/(16\pi k^2)$, see also [11]. Correspondingly the total radiated power is $P_r = \eta_0 p^{(\mathrm{rad})}/(8\pi k)$. In the previous expressions μ_0 and η_0 are respectively the free space permeability and impedance, and

$$w^{(e)} = \int_{\partial V} \int_{\partial V} \nabla_1 \cdot \boldsymbol{J}_1 \nabla_2 \cdot \boldsymbol{J}_2^* \frac{\cos(kR_{12})}{R_{12}} - \frac{k}{2} \big(k^2 \boldsymbol{J}_1 \cdot \boldsymbol{J}_2^* \\ - \nabla_1 \cdot \boldsymbol{J}_1 \nabla_2 \cdot \boldsymbol{J}_2^* \big) \sin(kR_{12}) \, \mathrm{dS}_1 \, \mathrm{dS}_2, \quad (2.3)$$

$$w^{(m)} = \int_{\partial V} \int_{\partial V} k^2 \boldsymbol{J}_1 \cdot \boldsymbol{J}_2^* \frac{\cos(kR_{12})}{R_{12}} - \frac{k}{2} \big(k^2 \boldsymbol{J}_1 \cdot \boldsymbol{J}_2^* \\ - \nabla_1 \cdot \boldsymbol{J}_1 \nabla_2 \cdot \boldsymbol{J}_2^* \big) \sin(kR_{12}) \, \mathrm{dS}_1 \, \mathrm{dS}_2, \quad (2.4)$$

and

$$p^{(\mathrm{rad})} = \int_{\partial V} \int_{\partial V} \big(k^2 \boldsymbol{J}_1 \cdot \boldsymbol{J}_2^* - \nabla_1 \cdot \boldsymbol{J}_1 \nabla_2 \cdot \boldsymbol{J}_2^* \big) \frac{\sin(kR_{12})}{R_{12}} \, \mathrm{dS}_1 \, \mathrm{dS}_2, \tag{2.5}$$

where $\boldsymbol{J}_1 = \boldsymbol{J}(\boldsymbol{r}_1)$, $\boldsymbol{J}_2 = \boldsymbol{J}(\boldsymbol{r}_2)$ and $R_{12} = |\boldsymbol{r}_1 - \boldsymbol{r}_2|$ are short notations for the surface current density $\boldsymbol{J}$ flowing on the boundary of volume V occupied by the entire structure and position vector $\boldsymbol{r}$.

The computation of stored energies and radiated power using (2.3), (2.4), and (2.5) is straight forward if implemented as an extension of an MoM code. Usual MoM solutions of the electric field integral equation (EFIE) use a set of local basis functions to approximate the surface current excited on the analyzed structure by a certain source [19]. Denoting by $\boldsymbol{\psi}_p$ the basis functions, this approximation is

$$\boldsymbol{J}(\boldsymbol{r}) \approx \sum_{p=1}^{N} J_p \boldsymbol{\psi}_p(\boldsymbol{r}). \tag{2.6}$$

The unknowns of the algorithm with this discretization are the coefficients $\mathbf{J} = (J_1, J_2, \ldots, J_N)^{\mathrm{T}}$. These coefficients are determined from the system of equations $\mathbf{ZJ} = \mathbf{V}$ where $\mathbf{V}$ is a discrete representation of the incident field (*e.g.*, the voltage gap model) and $\mathbf{Z}$ is the normalized impedance matrix computed based on a mixed potential formulation (equivalent to EFIE [15]) with the elements [19], normalized to $\eta_0/(4\pi k)$,

$$Z_{pq} = \mathrm{j} \int_{\partial V} \int_{\partial V} \left(k^2 \boldsymbol{\psi}_p(\boldsymbol{r}_1) \cdot \boldsymbol{\psi}_q(\boldsymbol{r}_2) - \nabla_1 \cdot \boldsymbol{\psi}_p(\boldsymbol{r}_1) \nabla_2 \cdot \boldsymbol{\psi}_q(\boldsymbol{r}_2) \right) \frac{\mathrm{e}^{-\mathrm{j}kR_{12}}}{R_{12}} \, \mathrm{dS}_1 \, \mathrm{dS}_2. \tag{2.7}$$

With the discretization defined by (2.6) the stored electric energy can be approximated using

$$w^{(\mathrm{e})} \approx \sum_{p=1}^{N} \sum_{q=1}^{N} J_p^* X_{\mathrm{e},pq} J_q = \mathbf{J}^{\mathrm{H}} \mathbf{X}_{\mathrm{e}} \mathbf{J}. \tag{2.8}$$

Apart from $\mathbf{X}_{\mathrm{e}}$, two other matrices, $\mathbf{X}_{\mathrm{m}}$ and $\mathbf{R}_{\mathrm{rad}}$, are introduced in a similar way respectively for the approximation of the stored magnetic energy and radiated power. These matrices have the same dimension as the impedance matrix, $N \times N$, and the elements:

$$X_{\mathrm{e},pq} = \int_{\partial V} \int_{\partial V} \nabla_1 \cdot \boldsymbol{\psi}_{p1} \nabla_2 \cdot \boldsymbol{\psi}_{q2} \frac{\cos(kR_{12})}{R_{12}}$$
$$- \frac{k}{2} \left(k^2 \boldsymbol{\psi}_{p1} \cdot \boldsymbol{\psi}_{q2} - \nabla_1 \cdot \boldsymbol{\psi}_{p1} \nabla_2 \cdot \boldsymbol{\psi}_{q2} \right) \sin(kR_{12}) \, \mathrm{dS}_1 \, \mathrm{dS}_2, \tag{2.9}$$

$$X_{\mathrm{m},pq} = \int_{\partial V} \int_{\partial V} k^2 \boldsymbol{\psi}_{p1} \cdot \boldsymbol{\psi}_{q2} \frac{\cos(kR_{12})}{R_{12}}$$
$$- \frac{k}{2} \left(k^2 \boldsymbol{\psi}_{p1} \cdot \boldsymbol{\psi}_{q2} - \nabla_1 \cdot \boldsymbol{\psi}_{p1} \nabla_2 \cdot \boldsymbol{\psi}_{q2} \right) \sin(kR_{12}) \, \mathrm{dS}_1 \, \mathrm{dS}_2, \tag{2.10}$$

and

$$R_{\mathrm{rad},pq} = \int_{\partial V} \int_{\partial V} \left(k^2 \boldsymbol{\psi}_{p1} \cdot \boldsymbol{\psi}_{q2} - \nabla_1 \cdot \boldsymbol{\psi}_{p1} \nabla_2 \cdot \boldsymbol{\psi}_{q2} \right) \frac{\sin(kR_{12})}{R_{12}} \, \mathrm{dS}_1 \, \mathrm{dS}_2. \tag{2.11}$$

With these notations the Q-factor (2.1) becomes

$$Q \approx \frac{\max\{\mathbf{J}^H \mathbf{X}_e \mathbf{J}, \mathbf{J}^H \mathbf{X}_m \mathbf{J}\}}{\mathbf{J}^H \mathbf{R}_{rad} \mathbf{J}}. \tag{2.12}$$

Quadratic forms similar to $\mathbf{J}^H \mathbf{R}_{rad} \mathbf{J}$ have been used in [14, 20] to express different types of power in radiating structures printed on dielectric substrates. These expressions have been further employed in the optimization of the radiation efficiency. A similar approach has been followed in the optimization of antenna arrays in free space [12].

As stated in the previous paragraph, an MoM solver can be extended to compute (2.9), (2.10) and (2.11). This extension does not significantly increase the computational complexity of the solver. We compare the original impedance matrix $\mathbf{Z}$ with the newly introduced matrices $\mathbf{X}_e$, $\mathbf{X}_m$ and $\mathbf{R}_{rad}$. This comparison shows that

$$Z_{pq} = R_{rad,pq} + \mathrm{j}(X_{m,pq} - X_{e,pq}), \tag{2.13}$$

and the second and third terms of $X_{e,pq}$ and $X_{m,pq}$ (correction terms introduced in [24]) are both equal to

$$-\frac{k}{2} \int_{\partial V} \int_{\partial V} \left(k^2 \boldsymbol{\psi}_{p1} \cdot \boldsymbol{\psi}_{q2} - \nabla_1 \cdot \boldsymbol{\psi}_{p1} \nabla_2 \cdot \boldsymbol{\psi}_{q2} \right) \sin(k R_{12}) \, \mathrm{dS}_1 \, \mathrm{dS}_2. \tag{2.14}$$

Equation (2.13) gives the elements of $\mathbf{R}_{rad}$ directly. The same equation gives the first terms of $X_{m,pq}$ and $X_{e,pq}$. Little computational effort is required to separate these terms from the imaginary part of Z_{pq}. The remaining correction terms (2.14) are non-singular. Their computation can be integrated in the calculation of the impedance matrix (2.7). These correction terms resemble the imaginary part of Z_{pq} except for the term causing the singularity, R_{12}. This resemblance can be utilized to reduce the computational overhead required by the correction term calculation with a standard MoM code.

In addition to the Q-factor computation, the relationship between the energies stored in the fields can be used as a measure of resonance. These energies are equal when the antenna is self resonant.

3   Implementation Example

3.1   Rectangular Regions

Infinitely thin lossless, *i.e.*, perfectly electrically conducting (PEC), metallic structures are considered in the following. These structures may take arbitrary shapes within a rectangular region with the length ℓ and width h. In order to limit the arbitrariness to a finite set of possible solutions, a discretization rule is established following the approach in [8, 10]. The natural choice is to use the same discretization as in the MoM solver used to determine the electromagnetic
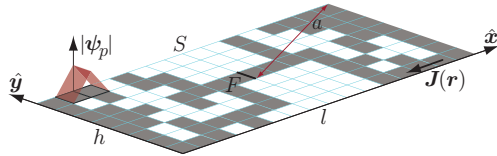
Figure 1: Example of discrete arbitrary structure within a rectangular region. The uniform rectangular grid defines the discretization of the region. Gray-shaded elements represent metallic patches on which a surface current density $\boldsymbol{J}(\boldsymbol{r})$ can exist. The feeding edge is marked F. The "rooftop" amplitude of one of the basis functions is represented in transparent red shading.

solution. This simplifies the optimization procedure and the MoM algorithm, as described in the following. Even though triangular mesh elements are more common, rectangular mesh elements [12, 18] pertain better to the considered regular shapes and illustration purposes of this study. Using rectangular mesh element discretization the optimal structures may take arbitrary shapes made of any of the mesh elements within the rectangular region. An example of such an antenna is depicted in Fig. 1.

The solution space of the optimization problem is made of all possible combinations of discrete elements. There are $2^{N_x N_y}$ such combinations, where N_x and N_y are the number of mesh elements in the x and y directions, respectively. Usually the number of combinations is large rendering prohibitive to study all solutions in the solution space.

One class of algorithms that search through an unknown solution space are heuristic global optimizers, *e.g.*, genetic algorithms, random search, particle swarm, ant colony, *etc*. Genetic algorithms have been used in electromagnetic optimization with remarkable results, see [13, 21, 23] for a description of the method and its applications. It is known that genetic algorithms feature an acceptably fast convergence to suboptimal solutions and avoid local extrema [21]. A genetic algorithm has been chosen here due to its well known principles, ease of adjustment and availability of sample codes. Other global optimization methods can be used similarly with the expressions in Sec. 2.

The fundamental principle of genetic optimization is to improve an initial random population towards an optimum in stages – generations – using evolutionary principles. To apply this algorithm to the situations considered here we define individuals and their fitness. A set of these individuals defines the population in each generation. Their fitness is a measure of optimality computed using the solution determined by the MoM solver.

Each individual corresponds to a single solution (combination of discrete mesh elements). Imposing a rule of numbering the elements of the mesh, the genotype of each individual is made of $N_x N_y$ possible genes in a single chromosome. Each gene determines if an element is metal or not present in a certain individual. A reasonable encoding for the genetic information is binary, 1 defining a metallic
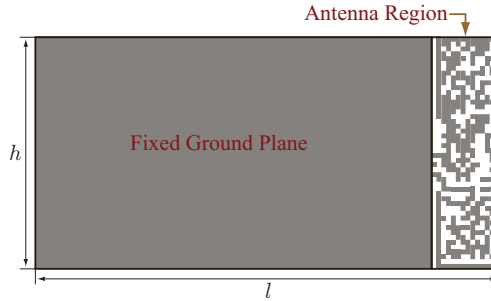
Figure 2: Example of simplified phone model with antenna region occupying approximately 15 % of the total length of the device.

and 0 a non present element. At least two genes are eliminated from the genotype as the edge between them defines the feed of the antenna represented by the individual. Patterned antennas can also be optimized by removing some of the genes corresponding to the fixed metallic areas. An example of such patterned antennas is described in Sec. 3.2 and 5.3.

The fitness of the individuals is given by the optimized parameter/parameters. Usually a linear combination of parameters is evaluated for each individual. Such parameters may be the Q-factor, matching, directivity, radiation pattern, metallic area, *etc.* These antenna parameters are computed here by an MoM solver with rectangular basis functions. Such basis functions usually decrease the number of MoM unknowns thus improving the solution time. Furthermore uniform discretization in both directions makes the basis functions equal (except for a spatial displacement). This fact is exploited to further improve the solution time.

The integration of the electromagnetic solver into the optimization algorithm follows the description in [21, Ch. 9]. The mother impedance matrix (2.7) of size $N = 2N_xN_y - N_x - N_y$ is computed once prior to the optimization. During the optimization the genotype of each individual determines which rows and columns of (2.7) compile the impedance matrix describing that individual. The rows and columns with the same indexes compile the matrices corresponding to $\mathbf{X}_e$, $\mathbf{X}_m$ and $\mathbf{R}_{rad}$ for each individual. The impedance matrix is used to compute the surface current density. This current can be used to compute other relevant parameters, *e.g.*, Q-factor (2.12), radiation pattern, radiation resistance, *etc.* The advantage of this approach is that impedance matrix compilation time is smaller than computation time with formulation (2.7).

3.2 Antennas Integrated into Devices

From the electromagnetic wave generation point of view, many mobile devices that integrate antennas can be thought of as consisting of two spatial domains.

One of the domains is represented by the space reserved for the structure (antenna) fed by the transmitter(s). This domain will be denoted in the following as the antenna region. The other domain contains all other parts integrated in the device. This domain usually contains metallic parts that act as ground for the structure in the antenna region. For this reason the second domain will be denoted ground plane in the following. In general the structures in both domains contribute to the radiated fields. It is also observed that the antenna region usually occupies a small fraction of the entire device.

We consider planar rectangular structures to further simplify the description of the previous paragraph. The two domains introduced above are defined as in Fig. 2. The optimization algorithm searches for metallic structures that may take arbitrary shapes within the antenna region. The other domain is a fixed rectangular metallic ground plane. This ground plane extends a significant part of the structure (75, 85 and 94 % of the area for the structures in Sec. 5.3). The metal is considered lossless as in the previous section, *i.e.*, PEC. Such structures can be studied using the same approach as in Sec. 3.1. However this implementation is rather inefficient due to the presence of the fixed ground plane. The large extent of this ground plane in the structure translates into large individual impedance matrices (*i.e.*, comparable in size with the mother impedance matrix). Such large matrices may result in an MoM solution time prohibitive for optimization.

It is more computationally efficient to use block matrix decomposition as described in [16, 21]. The solution of the MoM algorithm can be obtained from the system of equations

$$\left(\begin{array}{cc} \mathbf{Z}_{\mathrm{AA}} & \mathbf{Z}_{\mathrm{AG}} \\ \mathbf{Z}_{\mathrm{GA}} & \mathbf{Z}_{\mathrm{GG}} \end{array} \right) \left(\begin{array}{c} \mathbf{J}_{\mathrm{A}} \\ \mathbf{J}_{\mathrm{G}} \end{array} \right) = \left(\begin{array}{c} \mathbf{V} \\ \mathbf{0} \end{array} \right) \tag{3.1}$$

where the indexes A and G denote the antenna region and the ground plane respectively, $\mathbf{Z}_{\mathrm{AA}}$, $\mathbf{Z}_{\mathrm{AG}}$, $\mathbf{Z}_{\mathrm{GA}}$ and $\mathbf{Z}_{\mathrm{GG}}$ denote blocks of elements of the mother impedance matrix (2.7) with pq correspondingly in the domains defined by AA, AG, GA and GG, $\mathbf{J}_{\mathrm{A}}$ and $\mathbf{J}_{\mathrm{G}}$ are the blocks of basis function coefficients that define the current flowing on the antenna region and ground plane respectively, and $\mathbf{V}$ is the matrix corresponding to the feeding model. The structure is fed only in the antenna region, thus the $\mathbf{0}$ in the right hand side. The solution is

$$\begin{cases} \mathbf{J}_{\mathrm{A}} & = & (\mathbf{Z}_{\mathrm{AA}} - \mathbf{Z}_{\mathrm{AG}}\mathbf{Z}_{\mathrm{GG}}^{-1}\mathbf{Z}_{\mathrm{GA}})^{-1}\mathbf{V} \\ \mathbf{J}_{\mathrm{G}} & = & -\mathbf{Z}_{\mathrm{GG}}^{-1}\mathbf{Z}_{\mathrm{GA}}\mathbf{J}_{\mathrm{A}} = \mathbf{Z}'\mathbf{J}_{\mathrm{A}} \end{cases} \tag{3.2}$$

The preprocessing becomes more computationally demanding due to the necessity to express the inverse of $\mathbf{Z}_{\mathrm{GG}}$. However this does not affect the actual optimization process because the size of the matrices manipulated during this process reduces to the size of $\mathbf{Z}_{\mathrm{AA}}$ using a concept similar to the mother impedance matrix for the right hand sides of (3.2). Using the same approach the evaluation of the stored energies and radiated power necessary for the evaluation of the Q-factor (2.12) can be improved:

$$\mathbf{J}^{\mathrm{H}}\mathbf{X}_{\mathrm{e}}\mathbf{J} = \mathbf{J}_{\mathrm{A}}^{\mathrm{H}} \left(\mathbf{X}_{\mathrm{e,AA}} + 2\operatorname{Re}\{\mathbf{X}_{\mathrm{e,AG}}\mathbf{Z}'\} + \mathbf{Z}'^{\mathrm{H}}\mathbf{X}_{\mathrm{e,GG}}\mathbf{Z}' \right) \mathbf{J}_{\mathrm{A}} \tag{3.3}$$

where $\mathbf{X}_{e,AA}$, $\mathbf{X}_{e,AG}$ and $\mathbf{X}_{e,GG}$ are the blocks of $\mathbf{X}_e$ defined in the same way as those of $\mathbf{Z}$. It should be noted that the block matrix decomposition is performed in terms of basis functions, *i.e.*, the matrix elements in (3.1) correspond to basis functions defined on adjacent mesh elements. The inherent overlapping of the basis function domains of definition allows the existence of metallic elements supporting basis functions across the border between the ground plane and antenna region.

4   Physical Bounds

Physical bounds may be used as stopping criterion for an optimization process. They can also be used to compare the performance of optimized antennas. This comparison is illustrated in Sec. 5.2 and 5.3 respectively for antennas limited to rectangular regions and antennas with a fixed rectangular ground plane. These antennas are obtained through a genetic optimization process stopped by genetic stability during 50 generations. The Q-factors of these antennas do not deviate more than $30\,\%$ from their physical bound. This suggests that carefully integrated bounds may be used as stopping criterion in optimization algorithms.

The results in [6, 9, 39] are used to derive the physical bounds for antennas whose shapes are limited to rectangular regions[2]. The maximum D/Q ratio is computed with closed form expressions assuming main radiation direction orthogonal to the rectangle. The physical bound for the Q-factor can be derived further assuming that the antenna has directivity 1.5. The previous assumptions hold for many electrically small antennas.

Bounds for antennas with a fixed rectangular ground plane, see Fig. 2, are computed using the procedure described in [8, 10]. This procedure can be applied to structures with arbitrary shapes. The problem of determining the physical bound for the D/Q quotient of an antenna is solved using convex optimization [8]. This problem is equivalent to minimizing the energy stored in the fields excited by the antenna [10]. The current that minimizes this energy is determined by convex optimization. This current gives the minimum Q-factor of an antenna and the maximum D/Q quotient achievable by that antenna. It should be noted that this current may be unphysical thus impossible to excite on real structures. In this formulation it is assumed that the main radiation direction is orthogonal to the structure.

The bounds [8, 10] become those in [6, 9] when the antenna region occupies the entire rectangular region, *i.e.*, when antennas limited by a rectangular region are solved by convex optimization.

---

[2]see also http://www.mathworks.com/matlabcentral/fileexchange/26806-antennaq

5   Results

5.1   Simulation Setup

The genetic algorithm used here is based on Holter's implementation distributed with the PB-FDTD package [23]. We use a 200 individual population. Using tournament selection 80 randomly chosen individuals compete to become one of two breeding parents. Child generation is subjected to crossover and mutation. Offspring are generated in pairs and returned to the initial population. Then the population is decreased by removing the least fit two individuals.

Crossover happens at two random positions in the genotype with probability 0.8. The mutation rate is 0.2 when the population evolves naturally; in this situation a single gene is mutated at a time. The probability of mutation becomes 1 when the population does not improve during an entire generation. In all succeeding generations, all offspring will have 10 random genes mutated at a time. Due to randomness, the actual number of genes that are mutated may take any value between 1 and 10. If a new individual with better performance is found, the evolution returns to "natural" conditions, 0.2 single gene mutation probability. This behavior should increase the chances of finding better solutions in less generations. Even though the population evolution shows the expected behavior, a thorough performance study has not been carried out.

The stop condition of the algorithm is genetic stability of the population during 50 generations. This condition can be replaced by the best individual performance in the current population. When this performance is close enough to the physical bounds [6, 8–10] the optimization process can be stopped.

The objective function of the optimization algorithm is a linear combination of antenna parameters, *i.e.*,

$$\text{minimize} \qquad \alpha_Q Q + \alpha_R \left| \frac{\mathbf{J}^H \mathbf{X}_e \mathbf{J} - \mathbf{J}^H \mathbf{X}_m \mathbf{J}}{\mathbf{J}^H \mathbf{R}_{\text{rad}} \mathbf{J}} \right| + \alpha_{A_N} A_N, \qquad (5.1)$$

where α_Q, α_R and α_{A_N} are the weights associated with the Q-factor, resonance and normalized metallic area A_N, respectively. For illustrative purpose resonance is evaluated from the difference between the stored electric and magnetic energies. This difference is normalized to the radiated power. The area is normalized to the entire rectangular region area (antenna region area for antennas with a rectangular ground plane).

The weights introduced in the previous paragraph control the optimization process. Either α_Q or α_R is emphasized at a time for obtaining the data presented in the following. As a result either antennas with minimum Q or resonant are targeted, respectively. The normalized area weight has been maintained constant, $\alpha_{A_N} = 1$. This parameter has been included in order to decrease the metallic area of the structures and eliminate some isolated mesh elements.

The MoM solver integrated into the genetic algorithm is an EFIE based in-house simulator. Galerkin testing is used [19] with rooftop basis and testing

functions. The amplitudes of these functions have linear variation on two adjacent mesh elements, as exemplified in Fig. 1. Their direction is perpendicular to the common edge and pointing from the first to the second mesh element (considering a numbering rule imposed on the elements).

The optimization results are compared with simulation data obtained from the Efield MoM solver. This solver uses rooftop basis functions defined on triangular mesh elements. Non-self-resonant antennas have been loaded inductively such that they achieve resonance at the frequency they were optimized for. This loading has been used to confirm that tuning does not change the performance of the optimized antennas.

5.2 Rectangular Regions

The optimization algorithm has been run for rectangular regions with an aspect ratio of $\ell/h = 2$. Such regions can achieve the maximum D/Q ratio when operated optimally, [9, 10]. The antennas inside these regions are considered thin metallic sheets without losses, i.e., PEC. The frequencies were chosen such that the electrical dimensions are in the range $kl = 0.1 \ldots 1.3$ ($ka \approx 0.06 \ldots 0.7$). In this way some of the electrical dimensions usually considered small have been studied. The discretization was $N_x = 64$, $N_y = 32$ such that the discrete elements are square. A voltage gap model has been used to feed the antennas. Two mesh elements have been marked as fixed metallic areas and removed from the genotype. These elements are the two closest to the center of the rectangular region such that the voltage drop is applied along the x-direction, see Fig. 1.

From the symmetry point of view, three groups of structures have been considered: non-symmetric, symmetric with respect to $\hat{x}$ and symmetric with respect to $\hat{x}$ and $\hat{y}$, see Fig. 1. These are denoted as "None", "Single", and respectively "Double" in Figs 3 and 4. The corresponding number of genes in the genotype is: 2046, 1023 and 512.

Two optimization criteria have been imposed. They target to find either antennas with the optimal Q or antennas as close as possible to a resonance. The corresponding objective functions have $\alpha_Q = 4$, $\alpha_R = 1$ and $\alpha_Q = 1$, $\alpha_R = 4$ respectively.

The smallest Q-factor of 5 optimized antennas for each symmetry and criterion is depicted in Fig. 3. The physical bound for a rectangular region with the same dimensions is computed using the results in [6, 9, 10] and included for comparison. This computation is performed assuming main radiation direction orthogonal to the rectangle and directivity 1.5. The relative deviation of the Q-factor from this physical bound is depicted in Fig. 4. The antennas with the smallest Q in all runs per kl value have been simulated with Efield. Four of these antennas are depicted in Fig. 5. The resulting Q-factors computed according to [7, 26] are included in Fig. 4 for comparison. These antennas have radiation patterns resembling that of an electric dipole. Their directivities are between 1.49 and 1.52 in a direction within $30°$ of the normal of the rectangle.
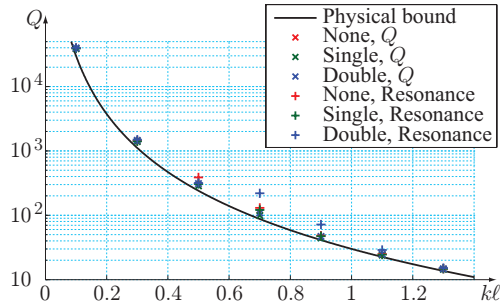
Figure 3: Optimized antenna Q-factors compared with the physical bound $[6, 9, 10]$ for rectangular regions. The best result from 5 runs for each symmetry (none, single and double) and optimization criterion (Q-factor or resonance) is depicted.
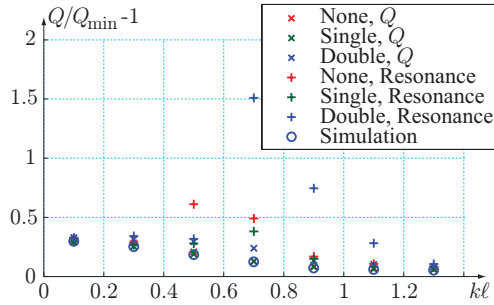
Figure 4: Deviation of the Q-factors depicted in Fig. 3 relative to the physical bound $Q_{\min}$ $[6, 9, 10]$. The deviations of the Q-factors computed from simulation data using the procedure in $[7, 26]$ are also included.

$kl=0.1$ $kl=0.5$ $kl=0.9$ $kl=1.3$
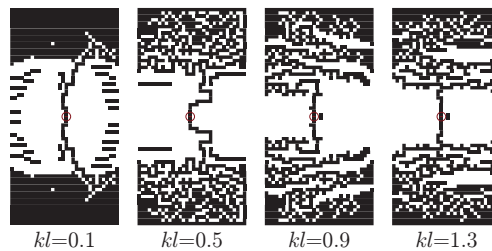
Figure 5: Four of the structures simulated in Efield whose Q-factors are depicted in Fig. 3. Feeding edges are circled.

Some observations can be made even though the number of runs is rather small. Antennas symmetric in the ℓ-direction have the smallest Q-factors. Antennas symmetric in both ℓ and h-directions have the greatest Q-factors. Intermediate Q-factors are obtained by antennas that are non-symmetric. The genetic algorithm can find antennas which perform within 10% of the physical bound when their dimensions are somewhat larger. When the antenna dimensions are smaller, the optimizer finds antennas about 30% away from the physical bound. Antennas optimized for resonance have a greater Q than those optimized for Q-factor, significantly greater for some electrical dimensions. This happens partly due to the compromise made during the optimization in the disadvantage of the Q-factor. This compromise modifies the genetic path followed by the antenna population based on the values involved in the computation of fitness with (5.1). However, a detailed study of the genetic path has not been carried out.

The optimized antennas show common characteristics that depend on their electrical size. A few such characteristics are given as examples in the following considering Fig. 5. The structure with $kl = 0.1$ has: large metallic regions at the extremities in the ℓ-direction, little meandering that increases the longest current path, and metallic strips parallel to the h direction which grow in length towards the extremities of the structure. The structure with $kl = 0.5$ is heavily meandered with many short metallic stubs along the meander; it has less metallic h-aligned strips. Larger structures are dominated by shorter meandering path and longer stubs. A statistic study has not been carried out to establish the distribution of these characteristics among the optimized antennas.

5.3   Simple Phone Model

A simplified model of a mobile telephone as a radiating device is obtained by considering the device mostly metallic. In a limited region a specially devised metallic structure is fed by the transmitter. For further simplification the metal is considered lossless, *i.e.*, PEC, and the entire structure planar, see Fig. 2. It has been observed that an aspect ratio $\ell/h = 2$ describes many mobile devices in use today. The frequencies have been chosen such that the electrical dimensions are in the range $\ell/\lambda = 0.1 \ldots 0.5$. These frequencies are between 300 MHz and 1.5 GHz for an $\ell = 10$ cm device. The discretization was $N_x = 96$ and $N_y = 48$ for the entire structure (antenna region and ground plane). Such structures but with coarser rectangular element mesh are preliminarily investigated in [2]. The procedure presented in Sec. 3.2 has been applied to increase the speed of the optimization process. The structures are fed by a voltage gap such that their far field is mainly linearly polarized along the ℓ dimension.

For illustration purpose the optimization procedure has been applied to two situations. In the first situation different dimensions of the antenna region have been imposed. The results of antenna optimization for minimum Q are presented in Fig. 6. The second situation illustrates the method for different optimization criteria and feeding positions, Fig. 7. Examples of optimized antenna regions
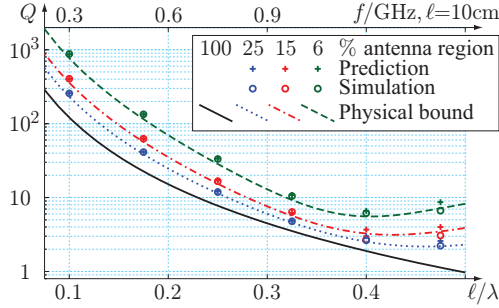
Figure 6: Optimized antenna Q-factors compared with the physical bound. The smallest Q-factor of five optimization algorithm runs per frequency and antenna region size is labeled "Prediction". The Q-factors computed using the results in [7, 25, 26] from simulation data for the smallest Q antennas are labeled "Simulation". The physical bounds for radiating structures with rectangular ground planes [8] and antenna regions occupying 6, 15 and 25 % of antenna length (see Fig. 2) are depicted in dashed, dash-dot and dotted line, respectively. The physical bound for antennas limited to rectangular regions [6, 9, 10] is depicted in solid line.

obtained in the above mentioned situations are depicted in Fig. 8.

Three cases have been considered for the results in Fig. 6 where approximately 6 %, 15 % and 25 % of the structure length is occupied by the antenna region. The optimization procedure has been run five times for each set of electrical and antenna region dimensions considered. The optimization target was antennas with minimum Q ($\alpha_Q = 10$, $\alpha_R = 1$). The smallest Q obtained in the five runs is labeled "Prediction". The antennas having these smallest Q-factors have been simulated in Efield. Their input impedance is differentiated following the procedure in [7, 26] to obtain the Q-factors labeled "Simulation". These antennas have a main radiation direction within $30°$ of the normal of the rectangular region. The physical bounds [8] corresponding to radiating structures with a rectangular ground plane, normal main radiation direction and antenna regions occupying 6 %, 15 % and 25 % of the antenna length are included in Fig. 6. In addition the physical bound [6, 9, 10] of rectangular radiating structures with normal main radiation direction and directivity 1.5 is depicted in solid line.

It is observed in Fig. 6 that both the predicted and the simulated Q values follow closely the physical bounds for small electrical dimensions. The relative deviation of these values from the corresponding physical bound is smaller than 20 % in these cases. The deviation is greater for smaller antenna regions. When the electrical sizes of the structures increase, the values resulted from the simulation data deviate from the predicted values. The simulation values are smaller than the predicted values and bound. This happens due to the Q-factor estimation procedure from the input impedance. Small Q values are estimated less accurately when multiple closely spaced resonances are present around the fre-
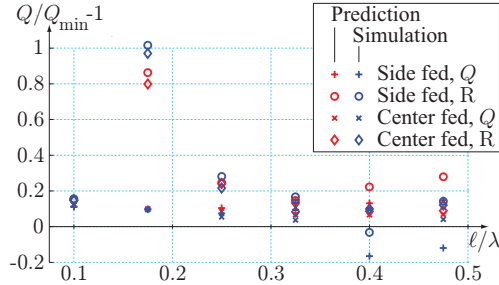
Figure 7: Deviation of optimized antenna Q-factors relative to the physical bound [8] for 15 % antenna regions (see Fig. 2). The smallest Q-factor from five optimization algorithm runs is labeled "Prediction". The Q-factors computed using the results in [7, 25, 26] from simulation data for the smallest Q antennas are labeled "Simulation". Side and center feeding has been considered for structures optimized for Q-factor and resonance (R).

quency of interest. The single resonance model [7, 26] was used to compute the Q for the structures with $\ell/\lambda = 0.1, 0.175$ and 0.25. The multiple resonance Brune synthesis model [25] was used to compute the Q for the structures with $\ell/\lambda = 0.325, 0.4$ and 0.475.

Four cases have been considered for the results in Fig. 7. They are defined by all the combinations of two feeding positions and two optimization targets applied to structures with the antenna region 15 % of the structure length. The two feeding positions are at the interface between the ground plane and the antenna region in the center of the h dimension and at the side of the structure. As optimization targets Q-factor ($\alpha_\mathrm{Q} = 10$, $\alpha_\mathrm{R} = 1$) and resonance ($\alpha_\mathrm{Q} = 1$, $\alpha_\mathrm{R} = 10$) have been considered. The optimization algorithm has been run five times for each case and frequency. The relative deviations of the smallest Q-factors obtained in the five runs are labeled "Prediction" in the figure. The reference for these relative deviations is the physical bound [8] for antenna regions occupying 15 % and normal main radiation direction. The antennas with these smallest Q-factors have been simulated in Efield. Their input impedance gives the Q-factors labeled "Simulation" using a resonance model [7, 25, 26]. These antennas have a main radiation direction within $30°$ of the normal of the structure. The observations pertaining to Figs 4 and 6 are also valid for Fig. 7.

6   Conclusions

A method of computing Q-factors of radiating structures from single frequency simulation data is presented. This computation is based on the electric and magnetic energies stored in the fields excited by an antenna [24] evaluated following the procedure described in [8, 10]. Using this method it is possible to estimate an-

$l/\lambda=0.1$ $l/\lambda=0.25$ $l/\lambda=0.4$
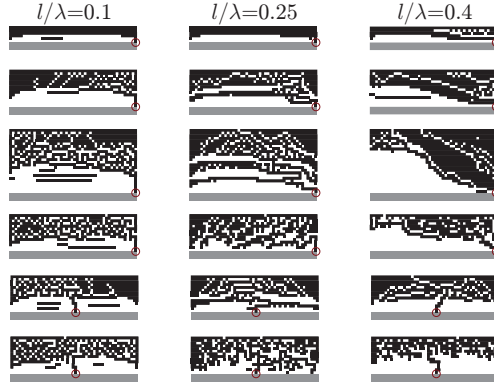
Figure 8: Example of antenna regions of structures simulated in Efield. Shaded – part of the ground plane. First three rows from top to bottom: side fed antenna regions occupying 6 %, 15 %, 25 % of antenna length optimized for Q-factor. Row 4: side fed 15 % antenna regions optimized for resonance. Rows 5 and 6: center fed 15 % antenna regions optimized for Q-factor and resonance, respectively. Feeding edges are circled.

tenna bandwidth from the current excited on the structure at a single frequency. This method has been applied to rectangular structures and structures with a rectangular ground plane describing in a simplified manner some mobile devices in use today. The resulting antennas perform close to the physical bounds in terms of their Q-factors for many electrically small dimensions. Simulation data obtained from the commercial electromagnetic solver Efield agree very well with the theoretical results.

The method can be integrated very easily in a standard MoM solver. The temporal overhead added by such an integration is small due to the fact that most of the quantities needed are computed in standard MoM solvers. Thus using this method may reduce optimization time for some radiating structures. In addition it is possible to directly compare realized performance of optimized structures with their physical bounds [8]. The results presented confirm the validity of these physical bounds. Sub-optimum solutions resulted from optimization have "genetic" characteristics that may prove useful for the manual design of other radiating structures.

The results obtained using this method have been presented in terms of antenna Q-factors. Other important antenna parameters such as radiation resistance, matching and losses are the object of future work. More realistic structures will be considered there.

Acknowledgment

References

[1] Antenna Standards Committee of the IEEE Antennas and Propagation Society. IEEE Standard Definitions of Terms for Antennas, 1993. IEEE Std 145-1993.

[2] M. Cismasu and M. Gustafsson. Illustration of mobile terminal antenna optimization by genetic algorithms with single frequency simulation. In *Electromagnetic Theory (EMTS), Proceedings of 2013 URSI International Symposium on*, pages 84–87, 2013.

[3] R. Fletcher. *Practical Methods of Optimization*. John Wiley & Sons, Ltd., Chichester, 1987.

[4] W. Geyi. A method for the evaluation of small antenna Q. *IEEE Trans. Antennas Propagat.*, **51**(8), 2124–2129, 2003.

[5] P. E. Gill, W. Murray, and M. H. Wright. *Practical Optimization*. Academic Press, London, 1981.

[6] M. Gustafsson, M. Cismasu, and S. Nordebo. Absorption efficiency and physical bounds on antennas. *International Journal of Antennas and Propagation*, **2010**(Article ID 946746), 1–7, 2010.

[7] M. Gustafsson and S. Nordebo. Bandwidth, Q-factor, and resonance models of antennas. *Progress in Electromagnetics Research*, **62**, 1–20, 2006.

[8] M. Gustafsson and S. Nordebo. Optimal antenna currents for Q, superdirectivity, and radiation patterns using convex optimization. *IEEE Trans. Antennas Propagat.*, **61**(3), 1109–1118, 2013.

[9] M. Gustafsson, C. Sohl, and G. Kristensson. Illustrations of new physical bounds on linearly polarized antennas. *IEEE Trans. Antennas Propagat.*, **57**(5), 1319–1327, May 2009.

[10] M. Gustafsson, M. Cismasu, and B. L. G. Jonsson. Physical bounds and optimal currents on antennas. *IEEE Trans. Antennas Propagat.*, **60**(6), 2672–2681, 2012.

[11] M. Gustafsson and B. L. G. Jonsson. Stored electromagnetic energy and antenna Q. Technical Report LUTEDX/(TEAT-7222)/1–25/(2012), Lund University, Department of Electrical and Information Technology, P.O. Box 118, S-221 00 Lund, Sweden, 2012. http://www.eit.lth.se.

[12] R. F. Harrington. *Field Computation by Moment Methods*. Macmillan, New York, 1968.

[13] R. L. Haupt and D. H. Werner. *Genetic Algorithms in Electromagnetics*. Wiley-IEEE Press, 2007.

[14] R. W. Jackson and D. M. Pozar. Full-wave analysis of microstrip open-end and gap discontinuities. *IEEE Trans. Microwave Theory Tech.*, **33**(10), 1036–1042, 1985.

[15] J. M. Jin. *Theory and Computation of Electromagnetic Fields*. Wiley, 2011.

[16] J. M. Johnson and Y. Rahmat-Samii. Genetic algorithms and method of moments GA/MOM for the design of integrated antennas. *IEEE Trans. Antennas Propagat.*, **47**(10), 1606–1614, oct 1999.

[17] L. S. Lasdon. *Optimization Theory for Large Systems*. Dover Books on Mathematics. Dover Publications, 2002.

[18] J. R. Mosig and F. E. Gardiol. A dynamical radiation model for microstrip structures. In P. W. Hawkes, editor, *Advances in Electronics and Electron Physics*, volume 59, pages 139 – 237. Academic Press, 1982.

[19] A. F. Peterson, S. L. Ray, and R. Mittra. *Computational Methods for Electromagnetics*. IEEE Press, New York, 1998.

[20] D. M. Pozar. Considerations for millimeter wave printed antennas. *IEEE Trans. Antennas Propagat.*, **31**(5), 740–747, September 1983.

[21] Y. Rahmat-Samii and E. Michielssen. *Electromagnetic Optimization by Genetic Algorithms*. Wiley Series in Microwave and Optical Engineering. John Wiley & Sons, 1999.

[22] J. Robinson and Y. Rahmat-Samii. Particle swarm optimization in electromagnetics. *IEEE Trans. Antennas Propagat.*, **52**(2), 397 – 407, feb. 2004.

[23] B. Thors, H. Steyskal, and H. Holter. Broad-band fragmented aperture phased array element design using genetic algorithms. *IEEE Trans. Antennas Propagat.*, **53**(10), 3280 – 3287, oct. 2005.

[24] G. A. E. Vandenbosch. Reactive energies, impedance, and Q factor of radiating structures. *IEEE Trans. Antennas Propagat.*, **58**(4), 1112–1127, 2010.

[25] O. Wing. *Classical Circuit Theory*. Springer, New York, 2008.

[26] A. D. Yaghjian and S. R. Best. Impedance, bandwidth, and Q of antennas. *IEEE Trans. Antennas Propagat.*, **53**(4), 1298–1324, 2005.

Multiband Antenna Q Optimization using Stored Energy Expressions

Marius Cismasu and Mats Gustafsson

Paper II

Abstract

A method to compute antenna Q from a single frequency current distribution is applied to the optimization of multiband radiating structures. A genetic algorithm produces suboptimal structures in the sense of simultaneous multiband minimum Q. These structures model in a simplified manner common wireless communication devices. The comparison with the physical bounds for the considered situations shows that the suboptimal structures perform close to their limitations. Matching networks are designed using real component models with a commercial tool. These networks have less than three components and provide less than $-6.5\,\mathrm{dB}$ reflection coefficient magnitude in all considered bands. The results show that the single frequency Q estimation method may be useful for antenna design.

1   Introduction

A method to compute antenna Q from a single frequency current excited on a radiating structure is presented in [7, 9], see also [10]. This method is based on stored electric and magnetic energy [5, 18] and radiated power expressions in terms of the current. The Q estimation method is applied in a genetic algorithm and method of moments (GA/MoM) [13, 16] scheme to optimize antenna Q and resonance at single frequencies in [3].

Here we apply the above introduced method to the multiband Q optimization of rectangular radiating structures with rectangular ground planes. Such structures model in a simplified manner common wireless communication terminals. An improved version of the genetic algorithm produces structures which are less prone to unpredictable behavior due to genetic characteristics such as isolated single mesh element metallic patches. The optimized structure input impedance is computed using the commercial electromagnetic solver ESI-CEM [4]. This result is used in the software tool BetaMatch [2] to design a matching network for all considered bands. The results show that the Q estimation method from the energy stored in excited fields and radiated power may be useful for the design process of radiating structures.

The comparison with the physical bounds for structures with a rectangular ground plane [7] shows that the optimized structures perform close to their physical limitations. Such a comparison can be used to stop an optimization process or assess the realizability of design specifications.

The paper is organized as follows. The results of the theory presented in [3, 7, 9] are included in Sec. 2. The multiband antenna objective function for optimization is introduced in Sec. 3. The setup used for obtaining the results of Sec. 4 is described in Sec. 4.1. Structures optimized using the GA/MoM scheme and their performance are presented in Sec. 4.2. The paper ends with conclusions, Sec. 5.

2   Antenna Q and Stored Energies

The quality factor of a lossless, resonant or nonresonant, antenna is defined as [19]

$$Q = \frac{2c_0 k \max\{W_e, W_m\}}{P_{\text{rad}}}, \tag{2.1}$$

where c_0 is the speed of light in free space, k is the wave number, W_e and W_m are respectively the electric and magnetic energies stored in the fields excited by the antenna, and P_r is the power radiated by the antenna. This definition is equivalent to that in [1] for resonant antennas.

We consider infinitely thin lossless perfectly electrically conducting (PEC) structures in vacuum on which surface current densities $\boldsymbol{J}$ may be excited. Such currents are approximated using a set of basis functions $\boldsymbol{\psi}_p$ as

$$\boldsymbol{J}(\boldsymbol{r}) \approx \sum_{p=1}^{N} J_p \boldsymbol{\psi}_p(\boldsymbol{r}), \tag{2.2}$$

where $\boldsymbol{r}$ is the position vector and $\mathbf{J} = (J_1, J_2, \ldots, J_N)^{\mathrm{T}}$ is a matrix of complex expansion coefficients. These coefficients are used to approximate the stored electric and magnetic energies and radiated power in (2.1) as

$$W_e \approx \frac{\mu_0}{4k} \sum_{p=1}^{N} \sum_{q=1}^{N} J_p^* X_{e,pq} J_q = \frac{\mu_0}{4k} \mathbf{J}^{\mathrm{H}} \mathbf{X}_e \mathbf{J}, \tag{2.3}$$

$$W_m \approx \frac{\mu_0}{4k} \sum_{p=1}^{N} \sum_{q=1}^{N} J_p^* X_{m,pq} J_q = \frac{\mu_0}{4k} \mathbf{J}^{\mathrm{H}} \mathbf{X}_m \mathbf{J}, \tag{2.4}$$

and

$$P_r \approx \frac{\eta_0}{2} \sum_{p=1}^{N} \sum_{q=1}^{N} J_p^* R_{r,pq} J_q = \frac{\eta_0}{2} \mathbf{J}^{\mathrm{H}} \mathbf{R}_r \mathbf{J}, \tag{2.5}$$

where μ_0 and η_0 are the free space permeability and impedance respectively, $\mathbf{X}_e$ and $\mathbf{X}_m$ are the electric and magnetic reactance matrices, and $\mathbf{R}_r$ is the radiation resistance matrix. These matrices have been introduced in [7, 9], see also [10]. Quadratic forms similar to those in (2.5) have been employed for antenna array optimization in free space [11]. Replacing (2.3), (2.4) and (2.5) in (2.1) we obtain:

$$Q \approx \frac{\max\{\mathbf{J}^{\mathrm{H}} \mathbf{X}_e \mathbf{J}, \mathbf{J}^{\mathrm{H}} \mathbf{X}_m \mathbf{J}\}}{\mathbf{J}^{\mathrm{H}} \mathbf{R}_r \mathbf{J}}. \tag{2.6}$$

The expansion coefficients in (2.2) can be computed using an electromagnetic solver, *e.g.*, ESI-CEM [4] or any other commercial solver. An EFIE (Electric Field Integral Equation) based MoM (Method of Moments) solver is straightforwardly

customizable for the computation of the matrices $\mathbf{X}_\mathrm{e}$, $\mathbf{X}_\mathrm{m}$ and $\mathbf{R}_\mathrm{r}$, [3, 7, 9]. This customization does not add a significant computational overhead to the original EFIE impedance matrix, $\mathbf{Z}$, computation [11, 12, 15]. Furthermore the previously mentioned four matrices are readily suitable for GA/MoM [13] optimization.

3   Multiband Antennas

Many hand-held mobile terminals support communication standards that operate in different frequency bands. One solution to accommodate this multiband requirement is to use antennas that perform acceptably well in all frequency bands needed for communication. In addition to multiband antennas matching networks are usually used to connect antennas to transceiver chains. These matching networks improve the intrinsic power transfer capability between transceiver and antenna and mitigate some effects of the changing communication environment on antenna performance.

We optimize the structures for minimum Q at the center frequency of each band of interest. The optimized structures are then simulated using the commercial solver ESI-CEM [4]. The input impedance obtained from the commercial solver is used in BetaMatch [2] to optimize a matching network for multiband operation. The results show that the stored energies (2.3) and (2.4) may be useful for automating part of the design process of mobile terminal antennas.

The GA/MoM procedure [13, 16, 17] is used to obtain suboptimal structures in the sense of multiband operation. An in-house genetic algorithm [3] searches the rows and columns of an impedance matrix that minimize the objective function

$$F_\mathrm{C} = \alpha_\mathrm{M} \max \left\{ \frac{Q_b}{Q_{\mathrm{T},b}} \right\}_{b=1,2,\ldots,N_\mathrm{b}} + \alpha_\mathrm{S} \sum_{b=1}^{N_\mathrm{b}} \frac{Q_b}{Q_{\mathrm{T},b}}, \tag{3.1}$$

where Q_b is the quality factor (2.6) at the center frequency of band b, $Q_{\mathrm{T},b}$ is the quality factor required for the antenna to meet the specifications in band b, N_b is the total number of frequency bands where the structure should operate, and α_M and α_S are weights associated with the maximum and sum of the normalized Q-factors for each band. Equation (3.1) is an example as different optimization criteria lead to different objective functions.

4   Results

4.1   Simulation Setup

Mobile terminals may be modeled, in a simplified manner, as rectangular regions. We consider, for further simplification, infinitely thin PEC radiating structures limited to a rectangular region with the length $\ell = 13\,\mathrm{cm}$ and width $w = 6.5\,\mathrm{cm}$. A small, rectangular part of this region, the "antenna region", is dedicated to

a structure fed by the transmitter(s), see Fig. 1. The structure in the antenna region is not necessarily rectangular. Here this structure is obtained through a process of GA/MoM optimization [13]. The remaining rectangular, usually larger, part of the region is considered entirely metallic and fixed. This part acts as a ground plane for the structure in the antenna region, contributing to the radiation of the structure. We refer to this part as the "ground plane" in the following.

The "mother" structure [13, 16] for the simplified situation above is a metallic, rectangular region of the same dimensions ℓ and w. This structure represents the maximum extent PEC metal may have in the radiating device. The mother structure is divided into $N_x = 120$ by $N_y = 60$ rectangular mesh elements in the $\hat{\boldsymbol{x}}$ and $\hat{\boldsymbol{y}}$ directions, respectively. Note that in this particular case the mesh elements are square. This discretization is used both in the MoM impedance matrix computation and in the genetic optimization.

An in-house EFIE based electromagnetic solver is used to compute the matrices $\mathbf{Z}$, $\mathbf{X}_e$, $\mathbf{X}_m$ and $\mathbf{R}_r$ for the mother structure. This solver uses Galerkin testing [15] with rooftop basis and testing functions. These functions are defined on pairs of adjacent mesh elements, *i.e.*, elements sharing a common edge, [14]. Their amplitudes are linearly increasing towards the common edge. Their directions are perpendicular to the common edge, pointing from the first to the second mesh element (considering a fixed mesh element numbering rule). The four matrices mentioned above are square with $N = 2N_x N_y - N_x - N_y = 14220$ rows.

Three frequency bands have been chosen to illustrate the Q computation procedure. These bands are $699 - 746$, $880 - 960$ and $1710 - 1990 \, \mathrm{MHz}$. The electrical sizes of the structure for the center frequencies are $k\ell \approx 1.97, 2.5$, and 5.04. The mother matrices $\mathbf{Z}_b$, $\mathbf{X}_{e,b}$, $\mathbf{X}_{m,b}$ and $\mathbf{R}_{r,b}$ are computed using the in-house solver described above for the center frequency of each band, indexed by $b = 1, 2, 3$.

A block matrix decomposition [13] is performed on each of the twelve mother matrices introduced in the previous paragraph. Denote one of these mother matrices $\mathbf{X} \in \{\mathbf{Z}_b, \mathbf{X}_{e,b}, \mathbf{X}_{m,b}, \mathbf{R}_{r,b}\}_{b=1,2,3}$. Each element of this matrix corresponds to a pair of basis and test functions. Considering a borderline between a metallic ground plane and an antenna region (*e.g.*, the line along which F is located in Fig. 1) we write

$$\mathbf{X} = \left(\begin{array}{cc} \mathbf{X}_{\mathrm{AA}} & \mathbf{X}_{\mathrm{AG}} \\ \mathbf{X}_{\mathrm{GA}} & \mathbf{X}_{\mathrm{GG}} \end{array} \right).$$

The elements of $\mathbf{X}$ with the corresponding basis and test functions entirely in the antenna region or across the borderline are grouped into the first block, $\mathbf{X}_{\mathrm{AA}}$. The elements with basis and test functions entirely in the ground plane are grouped into the block $\mathbf{X}_{\mathrm{GG}}$. The last two blocks have basis functions in the antenna region/across the border (ground plane) and test functions in the ground plane (antenna region/across the border), $\mathbf{X}_{\mathrm{AG}}$ ($\mathbf{X}_{\mathrm{GA}}$). The natural overlapping of the rooftop function domains of definition allows the existence of closed loops

of metal ground–antenna region–ground.

The sizes of the matrices manipulated during optimization reduce using block matrix decomposition. The EFIE MoM system of equations is written for each frequency

$$\left(\begin{array}{cc} \mathbf{Z}_{AA} & \mathbf{Z}_{AG} \\ \mathbf{Z}_{GA} & \mathbf{Z}_{GG} \end{array} \right) \left(\begin{array}{c} \mathbf{J}_A \\ \mathbf{J}_G \end{array} \right) = \left(\begin{array}{c} \mathbf{V} \\ \mathbf{0} \end{array} \right), \tag{4.1}$$

where $\mathbf{J}_A$ and $\mathbf{J}_G$ are the blocks of basis function coefficients that define the current flowing on the antenna region and ground plane respectively, $\mathbf{V}$ is a matrix that models the feeding of the structure, *e.g.*, a voltage gap, and the frequency band index has been omitted. Considering the structure fed only in the antenna region the current is

$$\left\{ \begin{array}{rcl} \mathbf{J}_A & = & (\mathbf{Z}_{AA} - \mathbf{Z}_{AG}\mathbf{Z}_{GG}^{-1}\mathbf{Z}_{GA})^{-1}\mathbf{V} \\ \mathbf{J}_G & = & -\mathbf{Z}_{GG}^{-1}\mathbf{Z}_{GA}\mathbf{J}_A = \mathbf{T}\mathbf{J}_A \end{array} \right. \tag{4.2}$$

The quadratic forms in (2.3), (2.4) and (2.5) take the form

$$\mathbf{J}^H\mathbf{X}\mathbf{J} = \mathbf{J}_A^H \left(\mathbf{X}_{AA} + 2\,\mathrm{Re}\{\mathbf{X}_{AG}\mathbf{T}\} + \mathbf{T}^H\mathbf{X}_{GG}\mathbf{T} \right) \mathbf{J}_A, \tag{4.3}$$

where $\mathbf{X} \in \{\mathbf{X}_e, \mathbf{X}_m, \mathbf{R}_r\}$. The block matrix decomposition is applied to the original mother matrices prior to the optimization procedure. The optimization algorithm searches the rows and columns of the matrices in parentheses in (4.2) and (4.3) that minimize the objective function (3.1). These latter matrices may be considered "mother" matrices for the optimization process. Their size is given by the size and shape of the antenna region. For example, in the case of a rectangular antenna region occupying 20% of the entire structure area as in Fig. 1, the size of the matrices in parentheses is 2856×2856.

An in-house genetic algorithm [3] is used to optimize the structures. This algorithm uses a population of 200 individuals out of which 80 are randomly chosen for tournament selection. The two point crossover probability is 0.8. A maximum of six genes at once are mutated with a probability of 20% if improvement of the objective function occurs within 100 iterations. After 100 iterations without improvement up to ten genes at once are mutated with 100% probability. The algorithm stops if the objective function does not improve during 50 generations, *i.e.*, 10^4 iterations.

The genetic algorithm is neither an exhaustive search of the optimum solution nor an exhaustive evaluation of the characteristics of a suboptimal solution. This algorithm uses genetic principles to drive an initially random population towards a suboptimal solution avoiding to some extent local extrema. Genetic principles allow the appearance of unwanted characteristics of offspring ("malformations"). For instance there may appear isolated single mesh element metallic patches or double 90° metallic bends diagonally interconnected (*i.e.*, corner connections). Such characteristics might have unpredictable effects on the manufactured structure performance. This is why such traits are specially "purged" after each offspring generation.
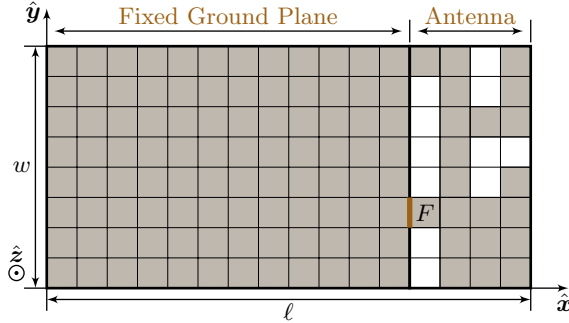
Figure 1: Example of discretized radiating structure with a fixed rectangular ground plane. Gray shaded elements represent metallic patches. The feeding edge is marked F.

The objective function (3.1) minimized by the GA is

$$F_{\mathrm{C}} = \max\left\{\frac{Q_1}{16}, \frac{Q_2}{12}, \frac{Q_3}{7}\right\} + 0.1\left(\frac{Q_1}{16} + \frac{Q_2}{12} + \frac{Q_3}{7}\right). \qquad (4.4)$$

The values 16, 12 and 7 are computed for less than $-6\,\mathrm{dB}$ reflection coefficient magnitude at the antenna input in all frequency bands [19].

The solutions obtained through optimization are simulated using the commercial solver ESI-CEM [4]. The input impedance computed by this solver is used in BetaMatch [2] to design a matching network. Models of large SMD (surface-mount devices) have been employed for matching. However not all optimized structures could be matched in all bands with realistic component models. In these situations matching with ideal components has been attempted.

The Q-factors of optimized structures are compared to the physical bounds [7, 9] for rectangular structures with a fixed rectangular ground plane. Here we maximize the $\hat{z}$ directivity – antenna Q (D/Q) quotient to derive the physical bound for the Q-factor. For illustration purpose the Q-factors are also compared to the physical bound [6, 8] for structures limited to rectangular regions. This latter bound is derived assuming the structures electrically small, $ka \ll 1$, radiating as an electric dipole with directivity approximately 1.5. Such comparisons with physical bounds may be used as stopping criteria for optimization algorithms applied to electrically small structures. For electrically large structures the physical bounds on Q [6–9] are less useful as the Q is very small and the antennas do not radiate mainly in the $\hat{z}$ direction.

4.2   Simple Phone Model

The structures optimized for multiband operation are exemplified in Fig. 1. Three sizes of the antenna region have been imposed: 20, 15 and 10% of the entire struc-
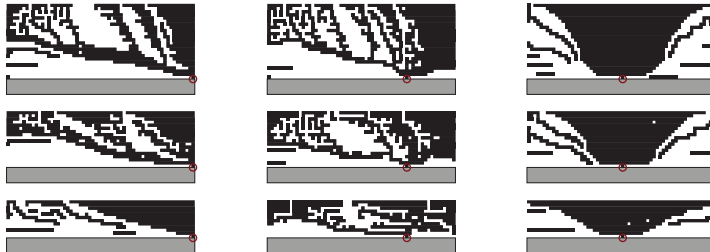
Figure 2: Example of antenna regions of structures optimized for multiband minimum Q. Rectangular regions $130 \times 65\,\text{mm}^2$ with fixed rectangular ground planes and antenna regions extending 20% (top row), 15% (middle row), and 10% (bottom row) of the entire structure area as depicted in Fig. 1. Fixed feeding edges are circled. Part of the ground plane is shaded.

ture area at one end in the ℓ direction. The feed has been placed at three fixed positions, all on the borderline between the ground plane and antenna region. These positions are the side, middle, and half way between side and middle in the w direction, *i.e.*, $y \approx 0.54, 16.8$, and $32\,\text{mm}$, respectively. The optimization algorithm has been run five times for each of the nine resulting combinations of antenna region size and feed position. The optimized antenna regions of the structures with the smallest objective function (4.4) per combination of antenna region size and feed position are depicted in Fig. 2.

The Q-factors (2.6) of the optimized structures depicted in Fig. 2 middle column are compared to the physical bounds [6–9] in Fig. 3 for electrical dimensions commonly accepted as small. These structures have the smallest objective function (3.1) compared to structures with the same size but different feeding positions. Simple matching networks are designed for the structures in Fig. 2 middle column using real component models in BetaMatch [2]. These networks, depicted in Fig. 4, allow matching to less than $-6.5\,\text{dB}$ reflection coefficient magnitude throughout all frequency bands.

5   Conclusions

A method of computing antenna Q from a single frequency current distribution [7, 9, 18] is used in a GA/MoM [13] scheme to optimize rectangular radiating structures for simultaneous multiple band minimum Q. A significant part of these structures is a fixed metallic ground plane such that these structures model in a simplified manner common wireless communication devices. The optimized antenna Q-factors have been compared to the physical bounds corresponding to the analyzed situations. This comparison shows that the suboptimal solutions perform close to the physical bounds. The optimized structures have been simulated in the commercial solver ESI-CEM [4]. The resulting input impedance data
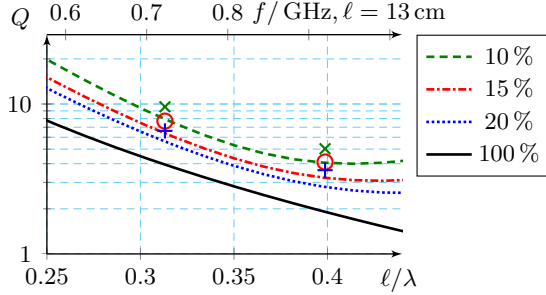
Figure 3: The Q-factors (2.6) of the structures with antenna regions depicted in Fig. 2 middle column (top row "+", middle row "○", and bottom row "×") compared to the physical bounds [7,9] for rectangular structures with antenna regions 20 %, 15 %, and respectively 10 % of the entire structure as in Fig. 1. The physical bound for structures limited to entire rectangular regions [8] is depicted in solid line (100 %). The frequency scale for an $\ell = 13$ cm structure is included.
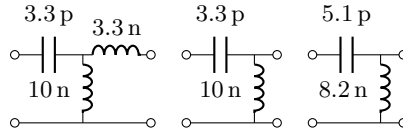
Figure 4: Matching networks for the structures with antenna regions depicted in Fig. 2 middle column, in SI units. From left to right the networks correspond to antenna regions extending 10%, 15% and respectively 20%.

has been used in BetaMatch [2] to design matching networks for the structures. These networks, designed with real component models, have less than three components and yield better than -6.5 dB matching in all considered bands.

The results presented in this paper suggest that the single frequency energy expressions (2.3), (2.4) and (2.5) may be useful for the design of antennas. The physical bounds described in [7, 9, 10] can be used to assess the feasibility of some designs.

Acknowledgment

References

[1] Antenna Standards Committee of the IEEE Antennas and Propagation Society. IEEE Standard Definitions of Terms for Antennas, 1993. IEEE Std 145-1993.

[2] MNW Scan, Singapore—BetaMatch, Software for antenna component matching. http://www.mnw-scan.com/.

[3] M. Cismasu and M. Gustafsson. Antenna Bandwidth Optimization with Single Frequency Simulation. *IEEE Trans. Antennas Propagat.*, **62**(3), 1304–1311, 2014.

[4] ESI Group, Paris, France—ESI Group's computational electromagnetic (CEM) solution. http://www.esi-group.com.

[5] W. Geyi. A method for the evaluation of small antenna Q. *IEEE Trans. Antennas Propagat.*, **51**(8), 2124–2129, 2003.

[6] M. Gustafsson, M. Cismasu, and S. Nordebo. Absorption efficiency and physical bounds on antennas. *International Journal of Antennas and Propagation*, **2010**(Article ID 946746), 1–7, 2010.

[7] M. Gustafsson and S. Nordebo. Optimal antenna currents for Q, superdirectivity, and radiation patterns using convex optimization. *IEEE Trans. Antennas Propagat.*, **61**(3), 1109–1118, 2013.

[8] M. Gustafsson, C. Sohl, and G. Kristensson. Illustrations of new physical bounds on linearly polarized antennas. *IEEE Trans. Antennas Propagat.*, **57**(5), 1319–1327, May 2009.

[9] M. Gustafsson, M. Cismasu, and B. L. G. Jonsson. Physical bounds and optimal currents on antennas. *IEEE Trans. Antennas Propagat.*, **60**(6), 2672–2681, 2012.

[10] M. Gustafsson and B. L. G. Jonsson. Stored electromagnetic energy and antenna Q. Technical Report LUTEDX/(TEAT-7222)/1–25/(2012), Lund University, Department of Electrical and Information Technology, P.O. Box 118, S-221 00 Lund, Sweden, 2012. http://www.eit.lth.se.

[11] R. F. Harrington. *Field Computation by Moment Methods*. Macmillan, New York, 1968.

[12] J. M. Jin. *Theory and Computation of Electromagnetic Fields*. Wiley, 2011.

[13] J. M. Johnson and Y. Rahmat-Samii. Genetic algorithms and method of moments GA/MOM for the design of integrated antennas. *IEEE Trans. Antennas Propagat.*, **47**(10), 1606–1614, oct 1999.

[14] J. R. Mosig and F. E. Gardiol. A dynamical radiation model for microstrip structures. In P. W. Hawkes, editor, *Advances in Electronics and Electron Physics*, volume 59, pages 139 – 237. Academic Press, 1982.

[15] A. F. Peterson, S. L. Ray, and R. Mittra. *Computational Methods for Electromagnetics*. IEEE Press, New York, 1998.

[16] Y. Rahmat-Samii and E. Michielssen. *Electromagnetic Optimization by Genetic Algorithms*. Wiley Series in Microwave and Optical Engineering. John Wiley & Sons, 1999.

[17] B. Thors, H. Steyskal, and H. Holter. Broad-band fragmented aperture phased array element design using genetic algorithms. *IEEE Trans. Antennas Propagat.*, **53**(10), 3280 − 3287, oct. 2005.

[18] G. A. E. Vandenbosch. Reactive energies, impedance, and Q factor of radiating structures. *IEEE Trans. Antennas Propagat.*, **58**(4), 1112–1127, 2010.

[19] A. D. Yaghjian and S. R. Best. Impedance, bandwidth, and Q of antennas. *IEEE Trans. Antennas Propagat.*, **53**(4), 1298–1324, 2005.

Stored Energy Based 3D Antenna Analysis and Design

Marius Cismasu, Doruk Tayli, and Mats Gustafsson

Paper III

Abstract

A method to estimate $Q_{Z'}$ of antennas from a single frequency current distribution is introduced. Three-dimensional (3D) antennas are studied using this single-frequency method and previous results on single-frequency Q-factor estimation and current optimization. Physical bounds on the D/Q-ratio are derived using the concept of optimum antenna current distribution in the studied situations. These bounds are used for an antenna placement analysis applied to a wireless device model. Furthermore, the performance of antennas optimized using a genetic algorithm is compared with physical bounds customized for each analyzed situation. A combination of antenna Q and $Q_{Z'}$ is used as optimization objective for a 3D radiating structure.

1 Introduction

Antenna Q can be computed from a single frequency current distribution on a radiating structure using the method presented in [12] and [10]; see also [13]. This method is based on expressing the electric and magnetic energies stored in the fields created, and the power radiated by an antenna in terms of the current [25]. The Q-factor estimation method is applied in a genetic algorithm and method of moments (GA/MoM), [17, 23], optimization procedure in [5, 6]. The concept of optimum antenna current distribution, [10], is used to assess the performance of GA-optimized radiating structures in [5, 6]. An ant colony optimization method generates antennas whose performance is compared with physical bounds in [24]. "Corner connections," a typical characteristic of metallic-patch-based genetically optimized antennas, can be avoided using methods such as random geometry refinement, [20], patch overlapping, [16], faulty-gene purging, [6], *etc.*

Here we extend the single-frequency Q-factor estimation concept to $Q_{Z'}$, a parameter introduced in [28]. A 3D structure is used to show that this parameter can have small values, *e.g.*, $Q_{Z'} \ll 1$ although $Q > 1$. The energy-based single-frequency antenna Q estimation method is applied to the single-band Q-factor optimization of 3D radiating structures with rectangular ground planes. These structures represent simplified models of common wireless communication terminals, more realistic compared to the planar models analyzed in [5, 6]. A GA/MoM, [17, 23], procedure optimizes antennas of such 3D structures for minimum Q-factor. This procedure uses an in-house MoM solver with variable change for integrating $1/R$ singularities [18]. The commercial electromagnetic solver ESI-CEM [7] is used to compute the input impedance of the optimized structures. A single resonance, [9, 28], or multiple resonance Brune synthesis model, [27], is employed to evaluate the Q-factor of the structures from their input impedance. The Q-factors obtained using the in-house and commercial solver agree to a large extent.

Optimum current densities, [10], in the sense of their D/Q ratio, are derived for the 3D structures studied in this paper. The D/Q ratio of an optimum

antenna current, realizable or not, gives the physical bound on D/Q for a real structure, *i.e.*, having a physical current density. The Q-factors of genetically optimized antennas are compared with Q-factors of optimum currents. The same conditions, *e.g.*, geometry, optimization region, dimensions, *etc.*, are used both in genetic optimization and current optimization. In this way the bounds are customized for the analyzed situation. Customized bounds and optimum currents are used in an antenna placement in wireless device study. The objective of this study is to determine the antenna location that maximizes the performance of the device, measured as D/Q-ratio or Q-factor.

The paper is organized as follows. A summary of the theory presented in [5, 10, 12] on the use of stored energies for antenna analysis and design is included in Section 2.1. The single frequency $Q_{Z'}$ estimation method is presented in Section 2.2. The convex optimization formulation used to derive physical bounds on D/Q and D/Q-optimum currents is described in Section 2.3. Section 3 presents the numerical simulations performed in this paper and their results. Section 3.1 describes the general simulation setup. The performance and examples of GA/MoM optimized 3D structures are presented and compared with optimum-current performance in Section 3.2. Section 3.3 illustrates the fact that some antennas can have $Q_{Z'} \ll 1$ even though $Q > 1$. An antenna placement situation is investigated using optimum currents and physical limitations in Section 3.4. The paper ends with conclusions in Section 4.

2 Stored Energies and Physical Bounds for Antenna Analysis and Design

2.1 Stored Energies

Practical antenna analysis and design is usually performed using numerical techniques that solve differential and/or integral equations describing an electromagnetic problem. Examples and details of numerical techniques for electromagnetics can be found in text books such as [15, 21], *etc.*, and references therein. Such techniques are based, in general, on a discretized computation domain. The method of moments (MoM) is a numerical method particularly appropriate for antenna analysis due to the fact that the discretized domain is the surface of the spatially finite radiating structure, [15]. We consider a structure discretized for analysis using an electric field integral equation (EFIE)-based MoM solver. The current density $\boldsymbol{J}$ excited on the surface of the structure is approximated in terms of the local basis functions $\boldsymbol{\psi}_p$ as

$$\boldsymbol{J}(\boldsymbol{r}) \approx \sum_{n=1}^{N} J_n \boldsymbol{\psi}_n(\boldsymbol{r}), \qquad (2.1)$$

where $\boldsymbol{r}$ is the position vector, $\mathbf{J} = (J_1, J_2, \ldots, J_N)^{\mathrm{T}}$ is a column vector of complex, surface-current, expansion coefficients, and N is the number of basis functions used to approximate the current. The expansion coefficients are usually determined from the system of equations

$$\mathbf{ZJ} = \mathbf{V}, \tag{2.2}$$

where $\mathbf{V}$ is a column vector describing the feeding of the structure, and $\mathbf{Z}$ is the impedance matrix describing the structure, [14, 15, 21].

The electric and magnetic energies stored in the fields created by a radiating structure, [25], are approximated in terms of the discrete current density $\mathbf{J}$ as the quadratic forms, [10],

$$W_{\mathrm{e}} \approx \frac{1}{4\omega} \mathbf{J}^{\mathrm{H}} \mathbf{X}_{\mathrm{e}} \mathbf{J} \tag{2.3}$$

and

$$W_{\mathrm{m}} \approx \frac{1}{4\omega} \mathbf{J}^{\mathrm{H}} \mathbf{X}_{\mathrm{m}} \mathbf{J}, \tag{2.4}$$

where ω is the angular frequency, and $\mathbf{X}_{\mathrm{e}}$ and $\mathbf{X}_{\mathrm{m}}$ are the electric and magnetic reactance matrices, respectively. The power radiated by an antenna is, [8, 13, 22, 25],

$$P_{\mathrm{r}} \approx \frac{1}{2} \mathbf{J}^{\mathrm{H}} \mathbf{R}_{\mathrm{r}} \mathbf{J}, \tag{2.5}$$

where $\mathbf{R}_{\mathrm{r}}$ is the radiation resistance matrix. Equations (2.3), (2.4) and (2.5) can be used to compute the Q-factor of a lossless resonant or non-resonant antenna as, [5, 28],

$$Q = \frac{2\omega \max\{W_{\mathrm{e}}, W_{\mathrm{m}}\}}{P_{\mathrm{r}}} \approx \frac{\max\{\mathbf{J}^{\mathrm{H}} \mathbf{X}_{\mathrm{e}} \mathbf{J}, \mathbf{J}^{\mathrm{H}} \mathbf{X}_{\mathrm{m}} \mathbf{J}\}}{\mathbf{J}^{\mathrm{H}} \mathbf{R}_{\mathrm{r}} \mathbf{J}}. \tag{2.6}$$

The definition in the first part of (2.6) is equivalent to that in [1] for resonant antennas. An overview of expressions for the Q-factor of antennas can be found in [26]. Equation (2.6) expresses the Q-factor of an antenna in terms of the current density computed for a single frequency. The bandwidth of an antenna can be estimated using a single frequency simulation, [5], based on the inverse proportionality between the bandwidth and Q in a single resonance model, [9, 28]. Quadratic forms similar to those in (2.5) have been employed for antenna array optimization in free space in [14].

The expressions for $\mathbf{X}_{\mathrm{e}}$, $\mathbf{X}_{\mathrm{m}}$ and $\mathbf{R}_{\mathrm{r}}$ resemble the expression for the EFIE-based impedance matrix, $\mathbf{Z}$, commonly computed by MoM solvers [5, 10, 12]. An MoM algorithm with Galerkin's method, [14, 21], applied to a mixed-potential EFIE formulation computes the impedance-matrix elements, [15, 21],

$$Z_{mn} = \mathrm{j}\eta_0 \int_{\partial V} \int_{\partial V} \left(k\boldsymbol{\psi}_{m1} \cdot \boldsymbol{\psi}_{n2} - \frac{1}{k}\nabla_1 \cdot \boldsymbol{\psi}_{m1} \nabla_2 \cdot \boldsymbol{\psi}_{n2} \right) \frac{\mathrm{e}^{-\mathrm{j}kR_{12}}}{4\pi R_{12}} \, \mathrm{dS}_1 \, \mathrm{dS}_2, \tag{2.7}$$

where η_0 is the free space impedance, $k = \omega/\mathrm{c}_0$ is the wave number, c_0 is the speed of light in free space, R_{12} is the distance between the integration points in the two

integration domains, and V is the the volume occupied by the antenna, bounded by the surface ∂V. Note that due to the inner product operation performed in the MoM, *i.e.*, one integration over the surface ∂V, the SI unit for Z_{mn} is Ωm^2 and for the right-hand-side $\mathbf{V}$—Vm. The resemblance of $\mathbf{X}_{\text{e}}$ and $\mathbf{Z}$ is illustrated by expressing the elements of the electric reactance matrix [10, 25]

$$
X_{\text{e},mn} = \eta_0 \int_{\partial V} \int_{\partial V} \nabla_1 \cdot \boldsymbol{\psi}_{m1} \nabla_2 \cdot \boldsymbol{\psi}_{n2} \frac{\cos(kR_{12})}{4\pi k R_{12}}
$$
$$
- \left(k^2 \boldsymbol{\psi}_{m1} \cdot \boldsymbol{\psi}_{n2} - \nabla_1 \cdot \boldsymbol{\psi}_{m1} \nabla_2 \cdot \boldsymbol{\psi}_{n2} \right) \frac{\sin(kR_{12})}{8\pi} \, \text{dS}_1 \, \text{dS}_2. \quad (2.8)
$$

Similarly, $\mathbf{X}_{\text{m}}$ and $\mathbf{R}_{\text{r}}$ resemble $\mathbf{Z}$ as (2.8) resembles (2.7) [5, 10]. These similarities allow integrating the computation of $\mathbf{X}_{\text{e}}$, $\mathbf{X}_{\text{m}}$ and $\mathbf{R}_{\text{r}}$ in EFIE-based MoM solvers with little computational effort.

The MoM matrices, $\mathbf{Z}$, $\mathbf{X}_{\text{e}}$, *etc.*, are intrinsically suitable for some global optimization algorithms such as GA/MoM optimization, [17, 23], current optimization, [10], *etc.* In such algorithms the optimization time of some antenna parameters, *e.g.*, the bandwidth, may be reduced using the single frequency expression (2.6) for Q. In addition these matrices are suitable for current optimization [10] used to derive physical limitations.

2.2 Single Frequency $Q_{\text{Z}'}$ Computation

Consider an antenna having the input impedance

$$
Z_{\text{in}}(k) = R_{\text{in}}(k) + \text{j}X_{\text{in}}(k). \quad (2.9)
$$

This antenna is tuned to achieve resonance at the wave number k_0 using a series-connected, ideal, lumped inductor or capacitor, as in [28]. The input impedance of the tuned antenna becomes

$$
Z_{\text{in,t}}(k) = Z_{\text{in}}(k) + \text{j}X_{\text{t}}(k), \quad (2.10)
$$

where

$$
X_{\text{t}}(k) = \begin{cases} \dfrac{-kX_{\text{in}}(k_0)}{k_0} & X_{\text{in}}(k_0) < 0 \\[2mm] \dfrac{-k_0 X_{\text{in}}(k_0)}{k} & X_{\text{in}}(k_0) > 0 \end{cases} . \quad (2.11)
$$

At the resonance frequency the input impedance has only the real part, *i.e.*,

$$
Z_{\text{in,t}}(k_0) = R_{\text{in}}(k_0). \quad (2.12)
$$

The Q-factor of the antenna tuned to resonance, in a single-resonance model, can be approximated as [28]

$$
Q_{\text{Z}'}(k_0) \approx \frac{k_0 \left| Z'_{\text{in,t}}(k_0) \right|}{2R_{\text{in}}(k_0)}, \quad (2.13)
$$

where prime denotes first derivative with respect to wave number. Note the change of variables $k = \omega/c_0$, performed in order for Z_{in} to be expressed in terms of the same frequency variable as $\mathbf{Z}$, whose elements are (2.7). If the single resonance assumption does not hold, the derivative of the input impedance may approach zero such that $Q_{\mathrm{Z}'} \approx 0$.

We express $Q_{\mathrm{Z}'}$ in terms of the frequency derivative of the impedance matrix, $\mathbf{Z}'$, whose elements are given by

$$
\frac{k \partial Z_{mn}}{\eta_0 \partial k} = \int_V \int_V \mathrm{j} \left(k^2 \boldsymbol{\psi}_{m1} \cdot \boldsymbol{\psi}_{n2} + \nabla_1 \cdot \boldsymbol{\psi}_{m1} \nabla_2 \cdot \boldsymbol{\psi}_{n2} \right) \frac{\mathrm{e}^{-\mathrm{j} k R_{12}}}{4 \pi k R_{12}}
$$
$$
+ \left(k^2 \boldsymbol{\psi}_{m1} \cdot \boldsymbol{\psi}_{n2} - \nabla_1 \cdot \boldsymbol{\psi}_{m1} \nabla_2 \cdot \boldsymbol{\psi}_{n2} \right) \frac{\mathrm{e}^{-\mathrm{j} k R_{12}}}{4 \pi} \, \mathrm{d}V_1 \, \mathrm{d}V_2. \quad (2.14)
$$

Replace (2.10) and (2.11) in (2.13) to obtain

$$
Q_{\mathrm{Z}'}(k_0) \approx \left| \frac{k_0 Z_{\mathrm{in}}'(k_0)}{2 R_{\mathrm{in}}(k_0)} + \mathrm{j} \frac{|X_{\mathrm{in}}(k_0)|}{2 R_{\mathrm{in}}(k_0)} \right|. \quad (2.15)
$$

An MoM solver gives all quantities needed to evaluate (2.15) except Z_{in}'. This quantity is traditionally computed using a numerical approximation based on evaluating Z_{in} for two closely spaced frequencies. An alternative to this approach is presented in the following.

The input impedance derivative is expressed in terms of the input admittance. The admittance matrix is given by:

$$
\mathbf{J} = \mathbf{Y}\mathbf{V} = \mathbf{Z}^{-1}\mathbf{V}. \quad (2.16)
$$

This matrix defines the input impedance of the antenna using a voltage gap model of feeding edge elements:

$$
Y_{\mathrm{in}} = \frac{\mathbf{V}^{\mathrm{T}} \mathbf{Y} \mathbf{V}}{V_{\mathrm{in}}^2}, \quad (2.17)
$$

where V_{in} is the voltage applied across the gap. Note that in an EFIE mixed-potential formulation with Galerkin testing and basis functions defined on pairs of adjacent rectangular mesh elements, [15, 19, 21], we have: $V_f = V_{\mathrm{in}} \ell_f$, where a voltage gap is applied along basis function f, and ℓ_f is the length of the edge common to the two rectangles where $\boldsymbol{\psi}_f \neq \mathbf{0}$. We consider that the source is real-valued and frequency independent, $i.e.$, $\mathbf{V}' = \mathbf{0}$. The input impedance derivative becomes

$$
Z_{\mathrm{in}}' = \left(\frac{1}{Y_{\mathrm{in}}} \right)' = -\frac{Y_{\mathrm{in}}'}{Y_{\mathrm{in}}^2} = -\frac{\left(\mathbf{V}^{\mathrm{T}} \mathbf{Y} \mathbf{V} \right)'}{V_{\mathrm{in}}^2 Y_{\mathrm{in}}^2} = -\frac{\mathbf{V}^{\mathrm{T}} \mathbf{Y}' \mathbf{V}}{V_{\mathrm{in}}^2 Y_{\mathrm{in}}^2}. \quad (2.18)
$$

Consider the following equation:

$$
\mathbf{0} = \left(\mathbf{Z}^{-1} \mathbf{Z} \right)' = \left(\mathbf{Z}^{-1} \right)' \mathbf{Z} + \mathbf{Z}^{-1} \mathbf{Z}'. \quad (2.19)
$$

Multiplication from the right by $\mathbf{Z}^{-1}$ gives

$$\mathbf{Y}' = -\mathbf{Z}^{-1}\mathbf{Z}'\mathbf{Z}^{-1} = -\mathbf{Y}\mathbf{Z}'\mathbf{Y}, \tag{2.20}$$

such that the input impedance derivative is

$$Z'_{\text{in}} = \frac{\mathbf{J}^{\text{T}}\mathbf{Z}'\mathbf{J}}{V_{\text{in}}^2 Y_{\text{in}}^2}, \tag{2.21}$$

where the fact that $\mathbf{Z}$ and $\mathbf{Y}$ are symmetric matrices has been used. Replace (2.21) in (2.15) to obtain

$$Q_{\text{Z}'}(k_0) \approx \left| \frac{k_0 Z_{\text{in}}^2(k_0)\mathbf{J}^{\text{T}}\mathbf{Z}'\mathbf{J}}{2R_{\text{in}}(k_0)V_{\text{in}}^2} + \mathrm{j}\frac{|X_{\text{in}}(k_0)|}{2R_{\text{in}}(k_0)} \right|, \tag{2.22}$$

where the first derivative with respect to wave number of the impedance matrix, $\mathbf{Z}'$, is computed for the wave number k_0. The corresponding expression for $Q_{\text{Z}'}$ in [4] differs from (2.22) as the former includes frequency derivatives of the current density and complex conjugates. An expression similar to (2.22) can be derived using a parallel tuning susceptance.

2.3   Physical Bounds

Physical bounds customized for the antennas analyzed can be derived by formulating appropriate optimization problems for antenna parameters [10]. These problems determine optimum antenna current densities in the sense of the parameter(s) of interest. Optimum antenna currents may or may not be physically realizable, *i.e.*, there may or may not exist a feeding scheme of the antenna that produces the optimum current. However, optimum currents give an upper bound on the performance a physical structure can achieve. One of the advantages of current optimization is the fact that customized bounds are derived without restrictive assumptions, *e.g.*, bounding geometry, electrical size, *etc.*

We use a convex optimization formulation for maximizing the partial directivity Q-factor ratio, D/Q, of radiating structures. This formulation is obtained by relaxation of, [10],

$$\begin{aligned} \text{minimize}_{\mathbf{J}} \quad & \max\{\mathbf{J}^{\text{H}}\mathbf{X}_{\text{e}}\mathbf{J}, \mathbf{J}^{\text{H}}\mathbf{X}_{\text{m}}\mathbf{J}\} \\ \text{subject to} \quad & \mathbf{F}^{\text{H}}\mathbf{J} = -\mathrm{j}, \end{aligned} \tag{2.23}$$

to the dual problem, [3],

$$\begin{aligned} \text{minimize}_{\mathbf{J}} \quad & \mathbf{J}^{\text{H}}\left(\alpha\mathbf{X}_{\text{e}} + (1-\alpha)\mathbf{X}_{\text{m}}\right)\mathbf{J} \\ \text{subject to} \quad & \mathbf{F}^{\text{H}}\mathbf{J} = -\mathrm{j}, \end{aligned} \tag{2.24}$$

over $0 \leqslant \alpha \leqslant 1$. The solution of (2.24) for a fixed α is

$$\mathbf{J} = \frac{-\mathrm{j}\left(\alpha\mathbf{X}_{\text{e}} + (1-\alpha)\mathbf{X}_{\text{m}}\right)^{-1}\mathbf{F}}{\mathbf{F}^{\text{H}}\left(\alpha\mathbf{X}_{\text{e}} + (1-\alpha)\mathbf{X}_{\text{m}}\right)^{-1}\mathbf{F}}, \tag{2.25}$$

with appropriate scaling of $\mathbf{J}$ such that $\mathbf{F}^{\mathrm{H}}\mathbf{J}$ is dimensionless. The $N \times 1$ matrix $\mathbf{F}$, with the elements

$$F_n^* = \frac{-\mathrm{j}k\eta_0}{4\pi} \int_V \hat{\boldsymbol{e}}^* \cdot \boldsymbol{\psi}_n(\boldsymbol{r}) \mathrm{e}^{\mathrm{j}k\hat{\boldsymbol{k}}\cdot\boldsymbol{r}}\,\mathrm{dV}, \tag{2.26}$$

is used to approximate the far field, $\boldsymbol{F}$, in the fixed direction $\hat{\boldsymbol{k}}$, projected on the polarization vector, $\hat{\boldsymbol{e}}$, as

$$\hat{\boldsymbol{e}}^* \cdot \boldsymbol{F}(\hat{\boldsymbol{k}}) \approx \mathbf{F}^{\mathrm{H}}\mathbf{J}. \tag{2.27}$$

Formulation (2.24) minimizes the energy stored in the fields created by a radiating structure for a fixed partial radiation intensity in a specific direction. Current densities optimum in the sense of (2.24) give the physical limitation on D/Q. The Q-factors of these currents, (2.6), may not be optimum in the sense of the Q-factor, $i.e.$, there may exist current densities producing smaller Q values. One advantage of formulation (2.24) and its solution (2.25) is the fact that there exist algorithms that solve (2.24) fast and efficiently even for large matrices and multiple directions and polarizations. For example the MATLAB function `fminbnd` can be used to solve (2.24).

3   Results

3.1   Simulation Setup

An in-house EFIE-based MoM solver computes the matrices $\mathbf{Z}$, $\mathbf{X}_{\mathrm{e}}$, $\mathbf{X}_{\mathrm{m}}$ and $\mathbf{R}_{\mathrm{r}}$ that describe the antennas studied. These matrices are used in GA/MoM as mother matrices [17], and for current optimization [10].

The in-house MoM-solver is based on Galerkin's method and a mixed potential EFIE-formulation [14, 15, 21]. The basis and testing functions have a "rooftop" profile on pairs of adjacent rectangular mesh elements, $i.e.$, rectangles sharing a common edge [19], as illustrated in Fig. 1. Such a function has the amplitude linearly increasing toward the common edge and the direction from the first to the second rectangle (numbered according to a fixed mesh element numbering rule). The change of variable described in [18] is used to integrate the $1/R$ singularity for identical and closely spaced mesh elements.

An in-house genetic algorithm [5, 6] is employed for searching realistic structures with performance close to physical limitations. An initially-random, 200-individual, antenna population is improved according to evolutionary principles in steps. At each step 80 randomly chosen individuals compete to become one of two breeding parents. The resulting two offspring are affected by two-point cross-over (which happens 80 % of the time) and single-gene mutation (20 % probability). These offspring are placed in the population, which is enlarged by two. The antennas in this expanded population are ranked according to their fitness. The two least-fit antennas are removed from the population. Fitness is evaluated
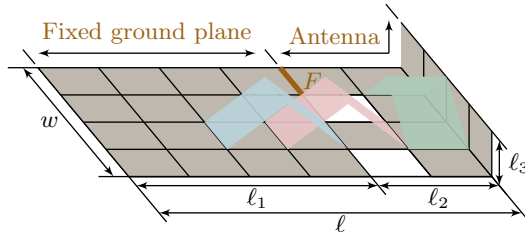
Figure 1: Illustration of rectangular mesh element discretization and "rooftop" basis function amplitude for a three-dimensional radiating structure. Metal areas are depicted in gray shading. The amplitudes of three of the total $7 \times 3 + 6 \times 4 - 4 - 3$ basis functions are depicted in blue, pink and green shading. The feeding edge is marked F.

as an objective (cost) function that is minimized during optimization. This function is a combination of antenna parameters with different weights. After 300 consecutive steps without population improvement the algorithm enters a phase where the offspring produced always have up to 4 genes mutated. This phase is meant to reduce the solution time of the GA (however, this time improvement has not been studied). Once improvement is observed, the algorithm returns to "natural" conditions, single-gene mutation with 20 % probability. The optimization is stopped after $2\ 10^5$ steps or when genetic stability during $2\ 10^4$ steps is observed.

The commercial electromagnetic solver ESI-CEM [7] is used to verify the results obtained using the in-house solver through genetic optimization. This commercial solver uses a triangular element mesh for discretizing the surfaces of analyzed structures. The results of a GA/MoM-optimized antenna ESI-CEM simulation are used to calculate the cost function for that antenna. In this way a comparison between the results obtained using the in-house solver and the commercial solver ESI-CEM is possible.

3.2   Bent-End Simple Phone Model

We consider infinitely-thin, lossless, perfect-electrical-conductor (PEC) structures in vacuum. The analyzed structures are spatially confined to three rectangular regions connected together as illustrated in Fig. 1. The first region has the length ℓ_1 and width $w = 7\,\mathrm{cm}$. This region is the fixed ground plane, [5, 6]. The second and third rectangular regions, with the lengths ℓ_2 and $\ell_3 = 0.7\,\mathrm{cm}$, respectively, and width w, represent the antenna region, [5, 6]. The lengths ℓ_1 and ℓ_2 are chosen such that $\ell_1 + \ell_2 = \ell = 14\,\mathrm{cm}$. The region with the length ℓ_3 extends in a direction perpendicular to the common plane of the other two regions. This arrangement models, in a simplified manner, some common mobile terminals.

Three situations of the above arrangement are considered. The structures

corresponding to these situations have $\ell_2 = 0.7$ cm, 1.4 cm and 2.8 cm, *i.e.*, 5%, 10% and 20% of ℓ, respectively. The ground plane is fixed and metallic (PEC). The antenna region is used for current optimization—to derive physical limitations, and for genetic optimization—to find realistic structures approaching their physical limitations. Physical limitations are derived using convex optimization formulation (2.24) for the D/Q-ratio for each situation, [10]. Antennas are optimized for minimum Q through the GA/MoM optimization procedure, [17, 23].

The mother structure, [17, 23], corresponding to the arrangement described above consists of three infinitely thin PEC rectangular surfaces with the lengths ℓ_1, ℓ_2 and ℓ_3, and width w arranged as in Fig. 1. This structure is discretized with a non-uniform mesh, finer in the antenna region than in the ground plane for all situations considered. The first 11.2 cm in the ℓ-direction from the left in Fig. 1 are divided in 40 mesh elements (and 25 in the w-direction). The remaining 2.8 cm in the ℓ-direction are divided in 20 mesh elements (and 50 in the w-direction). The bent region is divided in 5 by 50 mesh elements in the ℓ_3 and w directions, respectively. This particular choice of discretization results in square mesh elements with the side 1.4 mm in the antenna region and 2.8 mm in the ground plane. A row of overlapping basis functions in the ℓ-direction at the place of the discontinuity in the mesh size couples electrically the regions with different discretizations.

The mother matrices, *i.e.*, the matrices $\mathbf{Z}$, $\mathbf{X}_e$, *etc.*, describing the mother structure, are square with 4435 rows. A block matrix decomposition is applied to these matrices, [17]. This decomposition reduces the sizes of the matrices manipulated repetitively during the GA/MoM optimization. These latter matrices are square with 990, 1485 and 2475 rows respectively for $\ell_2 = 0.7$ cm, 1.4 cm and 2.8 cm.

The genetic optimization of antenna Q has been run for five frequencies, given by $\ell/\lambda = 0.1$, 0.2, 0.3, 0.4, and 0.5. Five optimized structures have been generated by the GA for each combination of ℓ_2 and frequency. The smallest optimized-structure Q-factor (2.6) of the five corresponding to each combination of ℓ_2 and frequency is labeled "Pred." in Fig. 2. The optimized structures with these smallest Q-factors (of which six are depicted in Fig. 3) have been simulated using the commercial solver ESI-CEM, [7]. The input impedance of these structures is used to obtain the Q-factors labeled "Sim." in Fig. 2. These Q-factors agree to a large extent with those obtained using the in-house MoM solver and the discrete expressions (2.3)–(2.6) (less than 6% deviation relative to the former Q values). The single-resonance model described in [9, 28], (2.13), is employed to compute the Q-factor for $\ell/\lambda = 0.1$ and 0.2. The Q-factors for the other frequencies are computed using the multiple-resonance, Brune-synthesis model, [27]. The single-frequency $Q_{Z'}$ (2.22) has been applied to the structures having the smallest Q-factors mentioned above. The $Q_{Z'}$ values in these cases have less than 5% difference relative to corresponding $Q_{Z'}$ values computed using (2.13).

The Q-factors obtained in optimization and simulation are compared to Q-factors given by optimum antenna current distributions, labeled "Opt." in Fig. 2.
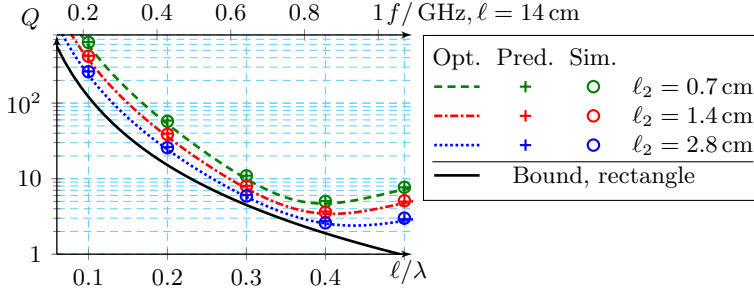
Figure 2: The Q-factors of antennas optimized using a genetic algorithm ("+") compared to corresponding Q-factors of D/Q-optimum current densities, [10], for the bent-end model illustrated in Fig. 1 with $\ell_2 = 0.7\,\mathrm{cm}$, $1.4\,\mathrm{cm}$ and $2.8\,\mathrm{cm}$ and $\ell = 14\,\mathrm{cm}$. The input impedance of the GA-optimized structures, computed by ESI-CEM, [7], has been used to calculate the Q-factors "∘" using a resonance model [9, 27, 28]. The physical bound on Q for a rectangular PEC surface $14 \times 7\,\mathrm{cm}^2$, [11], is depicted in solid black line.
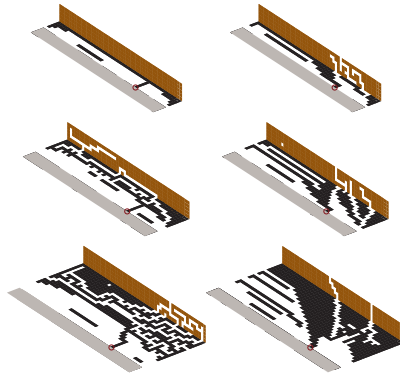
Figure 3: Example of genetic algorithm optimized structures (gray shading—part of the ground plane, black—antenna region part coplanar with the ground plane, bronze—antenna region part normal to the ground plane) with Q-factors depicted in Fig. 2 for $\ell/\lambda = 0.1$ (left column) and $\ell/\lambda = 0.5$ (right column), and $\ell_2 = 0.7\,\mathrm{cm}$ (top row), $1.4\,\mathrm{cm}$ (middle row), and $2.8\,\mathrm{cm}$ (bottom row). Feeding edges are circled.

These distributions are obtained using the convex optimization formulation (2.24) for the D/Q-quotient, [10]. The matrices involved in these formulations are square with 990, 1485 and 2475 rows respectively for $\ell_2 = 0.7$ cm, 1.4 cm and 2.8 cm. These matrices are obtained using a uniform, 1.4 mm-side square mesh element discretization of the mother structure—same mother structure as that considered for GA optimization. The physical bound on the Q-factor of a rectangular PEC region with the dimensions 14×7 cm^2 computed using the results in [11] is included for illustration. It is observed in Fig. 2 that the optimized-structure Q-factors are close to those achieved by optimum antenna currents (less than 13% deviation relative to the optimum-current Q-factors). Note that the current distributions used to compute the curves labeled "Opt." in Fig. 2 are optimum in the sense of D/Q. However, the Q-factors computed from these distributions may not be optimum in the sense of the Q-factor. This may result in structures that are on the "wrong side" of the D/Q-optimum current Q-factor, $e.g.$, below the curves in Fig. 2. The D/Q-quotient of such structures is on the "right side" of the physical bound.

3.3   Bent-End Simple Phone Model—Optimization for $Q_{Z'}$

The bent-end model with $\ell_1 = 12.6$ cm and $\ell_2 = 1.4$ cm, described in Sec. 3.2, has been optimized using the GA for operation between 700 MHz and 960 MHz. This frequency band is divided in two sub-bands with the center frequencies $f_{c,1} = 759.5$ MHz and $f_{c,2} = 889.5$ MHz, The fractional bandwidths of the two sub-bands are equal, FBW$_{1,2} \approx 15.8\%$. The matrices $\mathbf{Z}$, $\mathbf{X}_\mathrm{e}$, $\mathbf{X}_\mathrm{m}$ and $\mathbf{R}_\mathrm{r}$ are computed for the center frequencies. Two extra impedance matrices are computed for the frequencies $1.001 f_{c,1,2}$ in order to evaluate $Q_{Z'}$ at $f_{c,1,2}$ using (2.13). The cost function minimized by the genetic algorithm is

$$F_\mathrm{C} = \alpha_{\mathrm{Q,M}} \max\left\{ \frac{Q_1}{7} + \frac{Q_2}{7} \right\} + \alpha_{\mathrm{Q,S}} \left(\frac{Q_1}{7} + \frac{Q_2}{7} \right)$$
$$+ \alpha_{\mathrm{Q_{Z'},M}} \max\left\{ Q_{Z',1} + Q_{Z',2} \right\} + \alpha_{\mathrm{Q_{Z'},S}} \left(Q_{Z',1} + Q_{Z',2} \right), \quad (3.1)$$

where the indices 1 and 2 denote the sub-band, Q is the energy-based antenna-Q (2.6), $Q_{Z'}$ is the single-resonance input-impedance-derivative antenna-Q (2.13), and the weights α define the optimization target. The normalization values for Q, 7, ensure less than -6 dB reflection coefficient magnitude at the antenna input for the targeted FBW, under the assumption of single-resonance. The $Q_{Z'}$ values are not normalized because some applications target as low $Q_{Z'}$ as possible, $i.e.$, little variation of the input impedance in the operation band.

The GA has been run five times for each optimization target whose α-values are listed in Table 1. The Q-factors of the four GA-optimized structures depicted in Fig. 4 (of the total 15 structures) are presented in the same table. The structures corresponding to rows 1, 2 and 3 have the minimum cost function. The structure whose Q-factors are listed on row 4 has been optimized for simultaneous

Target	$\alpha_{Q,}$		$\alpha_{Q_{Z'},}$		Q_1	Q_2	$Q_{Z',1}$	$Q_{Z',2}$
	M	S	M	S				
1 min Q	1	0.1	0	0	4.6	3.7	2.9	0.3
2 min $Q_{Z'}$	0	0	1	0.1	8.2	8.9	0.01	0.01
3 min Q & $Q_{Z'}$	1	0.1	1	0.1	8.7	6.8	0.08	0.08
4					6.5	5.5	1.1	1.1

Table 1: GA cost function parameters and results for different optimization objectives
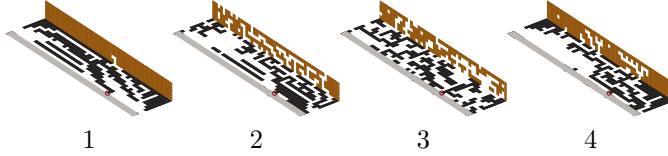
Figure 4: GA-optimized structures whose Q-factors are listed in Table 1. Gray shading—part of the ground plane, black—antenna region part coplanar with the ground plane, bronze—antenna region part normal to the ground plane. Feeding edges are circled.

minimum Q and $Q_{Z'}$, does not have the minimum cost function, but has minimum Q on both sub-bands (out of the total 5 GA-optimized structures with this target). The values for $Q_{Z'}$ listed in Table 1 are evaluated with (2.13). These values agree to a large extent with the same values reevaluated at the center frequencies with (2.22). The four structures of Fig. 4 have been simulated in ESI-CEM [7]. The magnitudes of the reflection coefficients at the inputs of these structures are depicted in Fig. 5. Matching networks that yield less than -6 dB reflection coefficient in the entire band have been designed using BetaMatch [2]. These networks are depicted in Fig. 6 and the resulting S_{11} magnitudes in Fig. 5. Real component models of surface-mount device (SMD) lumped elements, including losses, have been used for matching.

3.4   Wireless Terminal Antenna Placement Analysis Using Optimum Currents

Optimum antenna currents can be employed for evaluation and comparison of the performance achievable by a device with antennas placed at different locations. For illustration, we would like to determine the position and shape of the antenna region, [5, 6], that has the smallest Q-factor in the frequency range of Fig. 2. The nine 3D simplified models of common hand-held wireless terminals depicted in Fig. 7 are analyzed. These models are limited to a rectangular parallelepiped with the dimensions $\ell \times w \times h = 14 \times 7 \times 0.7 \, \text{cm}^3$ (*i.e.*, length × width × height). Note that limiting the structures to a parallelepiped is introduced for illustration purpose and does not restrict the applicability of the procedure exemplified here.
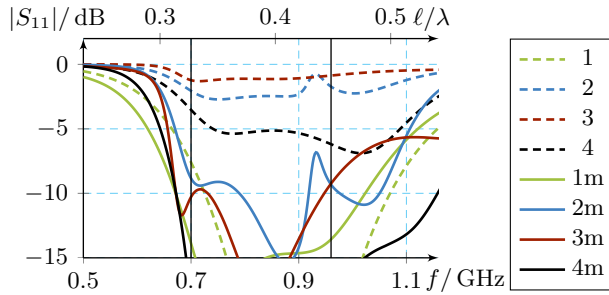
Figure 5: Magnitude of S_{11} at the input of the structures depicted in Fig. 4 without matching network, the curves labeled 1, 2, 3 and 4, and with the matching networks sketched in Fig. 6, the curves labeled 1m, 2m, 3m and 4m.
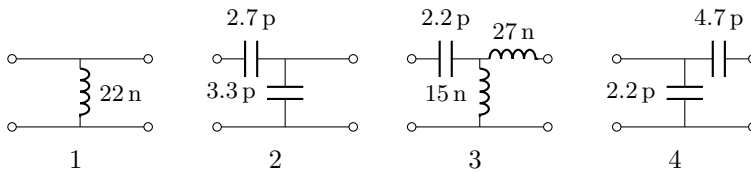
Figure 6: Matching networks designed for the structures depicted in Fig. 4 to yield less than $-6\,\mathrm{dB}$ reflection coefficient magnitude between $700 \ldots 960\,\mathrm{MHz}$ (solid curves in Fig. 5). Component values in SI units. Matching networks numbered as structures in Fig. 4—left to right and top to bottom.

Struct.	a	b	c	d	e, f	g	h	i
N	7584	8256	7568	7584	8256	8256	10830	7584
N_{AR}	1936	2608	1928	1944	2616	2612	5168	1992

Table 2: Dimensions of MoM matrices for the structures of Fig. 7

Each model is drawn in Fig. 7 to scale in three side views from the ℓ, w and h-directions (except for Fig. 7h where an h-side view and two sections through the symmetry planes are depicted). Gray and black represent the ground plane and antenna region, respectively. The thickness of the infinitely thin PEC material is exaggerated.

The ground plane, [5, 6], consists of an infinitely thin planar PEC sheet that covers 90 % of the area of one $\ell \times w$ face of the parallelepiped bounding the antenna. The remaining 10 % of that face represents the support of the antenna region, which may be continuous or divided in more sub-regions. Here, a maximum of two sub-regions have been used. The structures in the antenna regions are limited to infinitely thin PEC sheets placed on faces of the 3D shape of the antenna region. This shape is obtained by translating the 10 % of the $\ell \times w$-face area reserved for the antenna region a distance h perpendicularly to the ground plane (*i.e.*, by extruding the 10 % in the h-direction to the opposed face). The shapes resulting in the antenna region are made of rectangular parallelepipeds. These parallelepipeds are covered with PEC sheets on the four largest-area faces (in the case depicted in Fig. 7h there are four openings adjacent to the ground plane corners in the $w \times h$-plane; these are one mesh-element wide and extend the entire h-dimension).

The antenna region placement situations introduced above are discretized using a uniform mesh of $1.75 \times 1.75 \, \mathrm{mm}^2$ rectangular elements. The total number of basis functions, N, resulting for the structures depicted in Fig. 7 are presented in Table 2 (*i.e.*, the number of rows and columns, where applicable, of $\mathbf{Z}$, $\mathbf{Z}'$, $\mathbf{X}_{\mathrm{e}}$, $\mathbf{X}_{\mathrm{m}}$, $\mathbf{R}_{\mathrm{r}}$, and $\mathbf{F}$). The same table presents the number of rows, and columns where applicable, N_{AR}, of the blocks, [17], corresponding to the $10 \, \%$-$\ell \times w$-area antenna region [5, 6]. These blocks are computed for the matrices involved in the convex optimization formulation (2.24).

The bounds on D/Q using formulation (2.24) for the simplified models of Fig. 7 are depicted in Fig. 8. Linear polarization along the length and directivity in the direction of the height of the parallelepiped bounding the models are considered. The bound computed using the results in [11][1] for a rectangular, infinitely thin, $14 \times 7 \, \mathrm{cm}^2$ PEC sheet is labeled "R" in Fig. 8. The D/Q-optimum current distributions giving the physical bounds in Fig. 8 are used to compute the Q-factors (2.6) depicted in Fig. 9. The physical bound on Q for a rectangular $14 \times 7 \, \mathrm{cm}^2$ PEC sheet, [11], is labeled "R" in Fig. 9. The ring structure depicted in Fig. 7h outperforms all other structures in the figure in terms of D/Q and Q,

---

[1]http://www.mathworks.se/matlabcentral/fileexchange/26806-antennaq
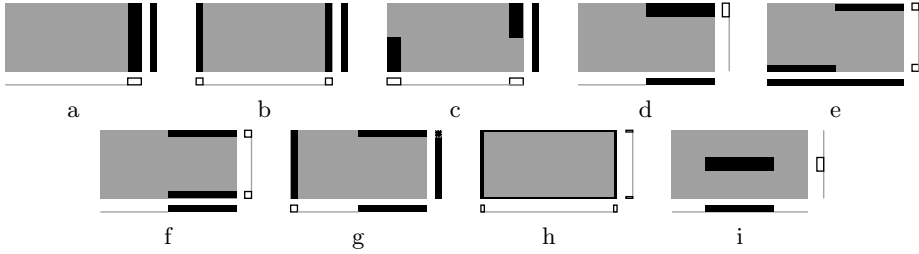
Figure 7: Nine simplified wireless-device models limited to a parallelepiped, consisting of a planar ground region extending 90% of one length×width face, and an antenna region occupying 10% of the parallelepiped volume. Three side views are depicted for a-g and i, *i.e.*, structures as seen along the length, width and height. A side view along the height and two sections at the symmetry planes are depicted for h. Gray shading—ground plane; black—antenna region, [5, 6].

except for a frequency region around $\ell/\lambda \approx 0.1$ where the structure in Fig. 7b has a greater D/Q. We also note that around $\ell/\lambda \approx 0.37$ a few of the structures in Fig. 7 reach close to the D/Q bound of a rectangular region and the structure in Fig. 7h has a D/Q value greater than that of a rectangular region. The optimum-current Q-factors do not reach as close to the physical bound on Q for a rectangular region as the D/Q-values.

4   Conclusions

A method to estimate $Q_{Z'}$ of antennas from the current distribution computed for a single-frequency is introduced. This method and other previous results are applied to three analysis and design situations of three-dimensional radiating structures. These applications suggest that customized physical bounds, optimum currents, and single-frequency expressions such as (2.6), (2.22), are tools that may be useful for antenna design, *e.g.*, to stop an optimization process, assess realizability of specifications, assess performance of antenna locations, *etc.*

The first situation mentioned above is global optimization of 3D antennas with knowledge of physical bounds pertaining the radiating structure as it is, without assumptions such as electrical size, bounding geometry, *etc.* The results presented here suggest that single-frequency estimations such as (2.6) and (2.22) can reduce the optimization time of some antenna parameters, *e.g.*, antenna bandwidth, Q. Furthermore, carefully integrated physical bounds can be used for physical-limitation aware optimization, *i.e.*, to stop an optimization process when the target is achieved with a certain margin.

The second situation is a non-exhaustive study of optimizing antennas for Q versus $Q_{Z'}$, or both. Four examples illustrate values for Q and $Q_{Z'}$ obtained by antennas optimized genetically for Q, (2.6), $Q_{Z'}$, (2.13), and both. The three
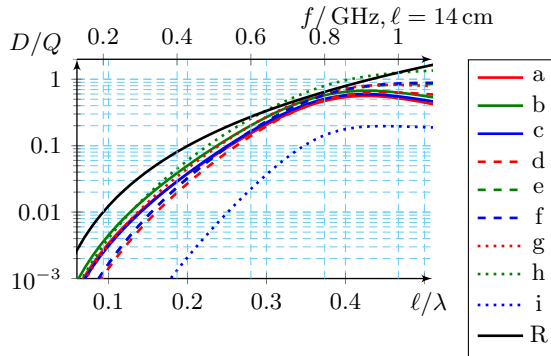
Figure 8: Physical bounds on D/Q for the structures depicted in Fig. 7 obtained using the convex optimization formulation (2.24), [10], when only the antenna region (black in Fig. 7) is optimized. The physical bound on D/Q for a rectangular PEC surface $14 \times 7\,\text{cm}^2$, [11], is depicted in solid black line and labeled "R."
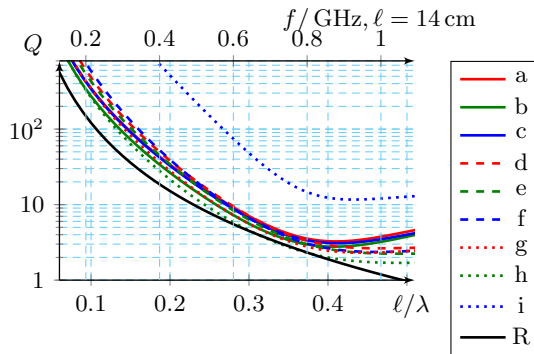
Figure 9: The Q-factors (2.6) achieved by the currents that give the optimum D/Q-values depicted in Fig. 8. The Q-factor of a $14 \times 7\,\text{cm}^2$ PEC rectangle, [11], is labeled "R."

targets include simultaneous operation on two different frequencies. The different frequencies can be centers of adjacent (as here) or separated frequency bands.

The third situation is the use of optimum antenna currents for determining the optimum position of an antenna in a wireless device. Nine simplified device models are analyzed, in which the antenna/antennas may occupy 10 % of the device volume. These models can be generated manually (as is the case here) or by an optimization process.

References

[1] Antenna Standards Committee of the IEEE Antennas and Propagation Society. IEEE Standard Definitions of Terms for Antennas, 1993. IEEE Std 145-1993.

[2] MNW Scan, Singapore—BetaMatch, Software for antenna component matching. http://www.mnw-scan.com/.

[3] S. P. Boyd and L. Vandenberghe. *Convex Optimization*. Cambridge Univ Pr, 2004.

[4] M. Capek, L. Jelinek, P. Hazdra, and J. Eichler. The Measurable Q Factor and Observable Energies of Radiating Structures. *IEEE Trans. Antennas Propagat.*, **62**(1), 311–318, Jan 2014.

[5] M. Cismasu and M. Gustafsson. Antenna Bandwidth Optimization with Single Frequency Simulation. *IEEE Trans. Antennas Propagat.*, **62**(3), 1304–1311, 2014.

[6] M. Cismasu and M. Gustafsson. Multiband Antenna Q Optimization using Stored Energy Expressions. *IEEE Antennas and Wireless Propagation Letters*, **13**(2014), 646–649, 2014.

[7] ESI Group, Paris, France—ESI Group's computational electromagnetic (CEM) solution. http://www.esi-group.com.

[8] W. Geyi. *Foundations of Applied Electrodynamics*. John Wiley & Sons, 2011.

[9] M. Gustafsson and S. Nordebo. Bandwidth, Q-factor, and resonance models of antennas. *Progress in Electromagnetics Research*, **62**, 1–20, 2006.

[10] M. Gustafsson and S. Nordebo. Optimal antenna currents for Q, superdirectivity, and radiation patterns using convex optimization. *IEEE Trans. Antennas Propagat.*, **61**(3), 1109–1118, 2013.

[11] M. Gustafsson, C. Sohl, and G. Kristensson. Illustrations of new physical bounds on linearly polarized antennas. *IEEE Trans. Antennas Propagat.*, **57**(5), 1319–1327, May 2009.

[12] M. Gustafsson, M. Cismasu, and B. L. G. Jonsson. Physical bounds and optimal currents on antennas. *IEEE Trans. Antennas Propagat.*, **60**(6), 2672–2681, 2012.

[13] M. Gustafsson and B. L. G. Jonsson. Stored electromagnetic energy and antenna Q. Technical Report LUTEDX/(TEAT-7222)/1–25/(2012), Lund University, Department of Electrical and Information Technology, P.O. Box 118, S-221 00 Lund, Sweden, 2012. http://www.eit.lth.se.

[14] R. F. Harrington. *Field Computation by Moment Methods*. Macmillan, New York, 1968.

[15] J. M. Jin. *Theory and Computation of Electromagnetic Fields*. Wiley, 2011.

[16] M. John and M. Ammann. Wideband Printed Monopole Design Using a Genetic Algorithm. *Antennas and Wireless Propagation Letters, IEEE*, **6**, 447–449, 2007.

[17] J. M. Johnson and Y. Rahmat-Samii. Genetic algorithms and method of moments GA/MOM for the design of integrated antennas. *IEEE Trans. Antennas Propagat.*, **47**(10), 1606–1614, oct 1999.

[18] M. A. Khayat and D. R. Wilton. Numerical evaluation of singular and near-singular potential integrals. *IEEE Trans. Antennas Propagat.*, **53**(10), 3180–3190, October 2005.

[19] J. R. Mosig and F. E. Gardiol. A dynamical radiation model for microstrip structures. In P. W. Hawkes, editor, *Advances in Electronics and Electron Physics*, volume 59, pages 139 – 237. Academic Press, 1982.

[20] M. Ohira, H. Deguchi, M. Tsuji, and H. Shigesawa. Multiband single-layer frequency selective surface designed by combination of genetic algorithm and geometry-refinement technique. *IEEE Trans. Antennas Propagat.*, **52**(11), 2925–2931, Nov 2004.

[21] A. F. Peterson, S. L. Ray, and R. Mittra. *Computational Methods for Electromagnetics*. IEEE Press, New York, 1998.

[22] D. M. Pozar. Considerations for millimeter wave printed antennas. *IEEE Trans. Antennas Propagat.*, **31**(5), 740–747, September 1983.

[23] Y. Rahmat-Samii and E. Michielssen. *Electromagnetic Optimization by Genetic Algorithms*. Wiley Series in Microwave and Optical Engineering. John Wiley & Sons, 1999.

[24] M. Shahpari, D. Thiel, and A. Lewis. An Investigation Into the Gustafsson Limit for Small Planar Antennas Using Optimization. *IEEE Trans. Antennas Propagat.*, **62**(2), 950–955, Feb 2014.

[25] G. A. E. Vandenbosch. Reactive energies, impedance, and Q factor of radiating structures. *IEEE Trans. Antennas Propagat.*, **58**(4), 1112–1127, 2010.

[26] J. Volakis, C. C. Chen, and K. Fujimoto. *Small Antennas: Miniaturization Techniques & Applications.* McGraw-Hill, New York, 2010.

[27] O. Wing. *Classical Circuit Theory.* Springer, New York, 2008.

[28] A. D. Yaghjian and S. R. Best. Impedance, bandwidth, and Q of antennas. *IEEE Trans. Antennas Propagat.*, **53**(4), 1298–1324, 2005.

Physical Bounds and Optimal Currents on Antennas

Mats Gustafsson, Marius Cismasu, B. L. G. Jonsson

Paper IV

Abstract

Physical bounds on the directivity Q-factor quotient and optimal current distributions are determined for antennas of arbitrary shape and size using an optimization formulation. A variational approach offers closed form solutions for small antennas expressed in the polarizability of the antenna structure. Finite sized antennas are solved using Lagrangian parameters in a method of moments formulation. It is also shown that the optimal charge density for a small antenna can be generated by several current densities. Numerical examples for small and large antennas are used to illustrate the results.

1   Introduction

Chu used spherical waves to express the stored and radiated energies outside the smallest circumscribing sphere of an antenna structure [3]. This approach has dominated the research on small antennas and offers many results on the Q-factor, and the directivity Q-factor quotient, D/Q, see [23] for an overview. The physical bounds on D/Q were generalized to arbitrary shapes using the forward scattering sum rule in [5, 7, 8]. Yaghjian and Stuart derived bounds on the Q-factor in the limit of small antennas $ka \ll 1$, see [25]. In [22], Vandenbosch determines analogous bounds on Q for non-magnetic antennas. The results in [5, 7, 8, 22, 25] are similar for the case of small dipole antennas composed of non-magnetic materials.

In this paper, new bounds on D/Q are derived using the expression for the stored energy given by Geyi [4] for small antennas and generalized to finite size by Vandenbosch [21]. Closed form solutions are presented in the limit of small antennas, where it is shown that it is sufficient to consider surface currents and the minimization problem separates for electric dipoles, magnetic dipoles and their combinations. Moreover, the bounds for the electric dipole case are identical to the bounds in [5, 7, 8], in this limit. The combined bound also resembles the combined TE and TM bound by Thal [18] for spherical geometries.

Antennas are often considered as small if $ka \leqslant 1$ or $ka \leqslant 1/2$, which is a range of many interesting antennas. It is, hence, important to analyze the antenna performance for ka in this range. Here, a Lagrangian formulation is used to solve the D/Q optimization problem for finite ka. We show that this maximization problem has large similarities with solving the classical integral equations in electromagnetics using the method of moments (MoM). The maximizing currents are obtained by solving a linear system. This makes the approach attractive as it determines the optimal current distribution as well as the upper bounds on D/Q.

The theoretical results are illustrated by numerical examples. The spherical region is used to illustrate that there are several optimal current densities that have identical charge densities. The considered current densities are similar to the current densities on folded spherical dipoles, capped spherical dipoles [17],

and folded spherical helix [2] antennas. Planar structures are analyzed in detail and the obtained bounds are similar to the bounds in [5, 7–9, 13]. It is shown that the self-resonant strip dipole antenna has a current density that is close to the optimal current density and also performs close to the bound. Moreover, numerical simulations show that an array of capacitively loaded dipoles performs close to the bound.

The expressions for the stored energies in [21] are very useful and produce similar bounds as in [5, 7, 8]. However, it is illustrated that the stored electric energy can be indefinite and explicit results are presented for divergence free loop type currents that have a negative stored electric energy for objects of the size $ka \approx 3/2$. It is shown that this problem can be mitigated by a Helmholtz decomposition of the current.

This paper is organized as follows. The optimization formulation for D/Q in the current density is introduced in Sec. 2. Closed form solutions in the limit of small antennas are derived using a variational formulation in Sec. 3. In Sec. 4, the D/Q bound is solved with a Lagrangian formulation for finite size antennas. Numerical examples for a spherical region, strip dipole antennas and two dipole arrays are presented in Sec. 5. Sec. 6 contains the conclusions. In App. A, explicit examples are given that illustrates that the considered stored electric energy is negative for some divergence free loop type currents.

2   Physical Bounds on the Directivity Q-factor Quotient

We consider antennas that are confined to a bounded volume V, see Fig. 1. It is assumed that the antenna structure is composed of non-magnetic materials. The electromagnetic fields are generated by the current densities, $\boldsymbol{J}$, flowing on the antenna.

To determine the directivity Q-factor quotient, D/Q, we express these quantities in terms of the definitions [1]. The partial directivity, $D(\hat{\boldsymbol{k}}, \hat{\boldsymbol{e}})$, characterizes the radiation properties of the antenna. It is defined as

$$D(\hat{\boldsymbol{k}}, \hat{\boldsymbol{e}}) = 4\pi \frac{P(\hat{\boldsymbol{k}}, \hat{\boldsymbol{e}})}{P_{\text{rad}}}, \tag{2.1}$$

where $P(\hat{\boldsymbol{k}}, \hat{\boldsymbol{e}})$ denotes the radiation intensity in the direction $\hat{\boldsymbol{k}}$ with polarization $\hat{\boldsymbol{e}}$ and P_{rad} is the total radiated power. The quality factor, Q, is defined as

$$Q = \frac{2\omega W}{P_{\text{rad}}} = \frac{2\text{c}_0 kW}{P_{\text{rad}}}, \tag{2.2}$$

where $W = \max\{W_{\text{e}}, W_{\text{m}}\}$ denotes the maximum of the stored electric and magnetic energies, ω is the angular frequency, k the wave number, and c_0 the speed
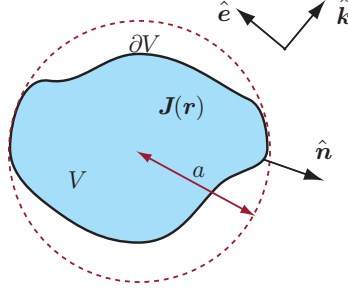
Figure 1: Illustration of the object geometry V, with boundary ∂V and with outward normal unit vector $\hat{n}$ and current density $J(r)$. The radiated far field is evaluated in the $\hat{k}$-direction for the polarization $\hat{e}$ in free space. The object is circumscribed by a sphere with radius a.

of light in free space. Combine (2.1) and (2.2) to express the directivity Q-factor quotient as

$$\frac{D(\hat{k}, \hat{e})}{Q} = \frac{2\pi P(\hat{k}, \hat{e})}{c_0 k W}. \tag{2.3}$$

We now express D/Q in terms of the electric current density J in the antenna volume V. Note that there are no magnetic currents due to the assumption of non-magnetic materials. The radiation intensity from the current density J in the direction $\hat{k}$ and polarization $\hat{e}$ is

$$P(\hat{k}, \hat{e}) = \frac{\zeta_0 k^2}{32\pi^2} \left| \int_V \hat{e}^* \cdot J(r) e^{jk\hat{k}\cdot r} \, dV \right|^2, \tag{2.4}$$

where $\hat{k} \cdot \hat{e} = 0$ is used, ζ_0 denotes the free space impedance, the superscript, $*$, denotes the complex conjugate, and the time convention $e^{j\omega t}$ is used.

The aim of this paper is to determine an upper bound on D/Q. It is not clear how to decompose the energy in its radiated and stored parts, see *e.g.*, [3, 4, 21, 26]. Similarly to the discussion in [22] we only use the vacuum terms of the stored energies, see also [24]. Here, we use the results by Vandenbosch [21], and write the free space part of the stored electric energy as $W_e = \mu_0/(16\pi k^2) w^{(e)}$, where

$$w^{(e)} = \int_V \int_V \nabla_1 \cdot J_1 \nabla_2 \cdot J_2^* \frac{\cos(kR_{12})}{R_{12}} - \frac{k}{2} \big(k^2 J_1 \cdot J_2^* $$
$$- \nabla_1 \cdot J_1 \nabla_2 \cdot J_2^* \big) \sin(kR_{12}) \, dV_1 \, dV_2, \tag{2.5}$$

and $J_1 = J(r_1)$, $J_2 = J(r_2)$, $R_{12} = |r_1 - r_2|$ and μ_0 is the permeability of free space. The corresponding stored magnetic energy is $W_m = \mu_0/(16\pi k^2) w^{(m)}$,

where

$$w^{(\mathrm{m})} = \int_V \int_V k^2 \boldsymbol{J}_1 \cdot \boldsymbol{J}_2^* \frac{\cos(kR_{12})}{R_{12}} - \frac{k}{2} \big(k^2 \boldsymbol{J}_1 \cdot \boldsymbol{J}_2^* $$
$$- \nabla_1 \cdot \boldsymbol{J}_1 \nabla_2 \cdot \boldsymbol{J}_2^* \big) \sin(kR_{12}) \,\mathrm{dV}_1 \,\mathrm{dV}_2. \quad (2.6)$$

We now have an explicit expression for D/Q in the current density $\boldsymbol{J}$, $i.e.$,

$$\frac{D(\hat{\boldsymbol{k}}, \hat{\boldsymbol{e}})}{Q} = k^3 \frac{\left| \int_V \hat{\boldsymbol{e}}^* \cdot \boldsymbol{J}(\boldsymbol{r}) \mathrm{e}^{\mathrm{j} k \hat{\boldsymbol{k}} \cdot \boldsymbol{r}} \,\mathrm{d}V \right|^2}{\max\{w^{(\mathrm{e})}(\boldsymbol{J}), w^{(\mathrm{m})}(\boldsymbol{J})\}}, \quad (2.7)$$

where $w^{(\mathrm{e})}(\boldsymbol{J})$ and $w^{(\mathrm{m})}(\boldsymbol{J})$ are defined in (2.5) and (2.6). The D/Q quotient is maximized to produce physical bounds, $i.e.$,

$$\frac{D(\hat{\boldsymbol{k}}, \hat{\boldsymbol{e}})}{Q} \leqslant \max_{\boldsymbol{J}} k^3 \frac{\left| \int_V \hat{\boldsymbol{e}}^* \cdot \boldsymbol{J}(\boldsymbol{r}) \mathrm{e}^{\mathrm{j} k \hat{\boldsymbol{k}} \cdot \boldsymbol{r}} \,\mathrm{d}V \right|^2}{\max\{w^{(\mathrm{e})}(\boldsymbol{J}), w^{(\mathrm{m})}(\boldsymbol{J})\}}, \quad (2.8)$$

where $\boldsymbol{J}$ are all the admissible current densities in V. The continuity of the normal component requires that $\hat{\boldsymbol{n}} \cdot \boldsymbol{J}(\boldsymbol{r}) = 0$ for $\boldsymbol{r} \in \partial V$, where $\hat{\boldsymbol{n}}$ is the outward unit normal of the antenna volume V, see Fig. 1.

Note that (2.8) is invariant for amplitude scalings $\boldsymbol{J} \to \alpha \boldsymbol{J}$, and if $\boldsymbol{J}_0$ is a solution to the maximization problem, then $\boldsymbol{J}_1 = \boldsymbol{J}_0 / \int \hat{\boldsymbol{e}}^* \cdot \boldsymbol{J}_0 \mathrm{e}^{\mathrm{j} k \hat{\boldsymbol{k}} \cdot \boldsymbol{r}} \,\mathrm{d}V$ is another solution to it. This property is used repeatedly in the upcoming sections to reformulate the optimization problem and to determine the maximizing current density.

We first analyze electrically small antennas to find closed form solutions of the D/Q-bound in Sec. 3, $i.e.$, the current expressions are analyzed in the limit $ka \to 0$, where a denotes the radius of the smallest sphere that circumscribes the antenna volume V. The general case with finite ka is considered in Sec. 4.

3 Electrically Small Antennas

The radiation intensity (2.4) and stored electric (2.5) and magnetic (2.6) energies simplify in the low-frequency limit, $k \to 0$ for fixed a. We use the expansions $\mathrm{e}^{\mathrm{j} k \hat{\boldsymbol{k}} \cdot \boldsymbol{r}} = 1 + \mathrm{j} k \hat{\boldsymbol{k}} \cdot \boldsymbol{r} + \mathcal{O}(k^2)$ and $\boldsymbol{J} = \boldsymbol{J}^{(0)} + k \boldsymbol{J}^{(1)} + o(k)$ as $k \to 0$, where $\nabla \cdot \boldsymbol{J}^{(0)} = 0$ and $\nabla \cdot \boldsymbol{J}^{(1)} = -\mathrm{j}\rho$ follow from the continuity equation. Note that the charge density in SI-units is given by $\rho_{\mathrm{SI}} = \rho/c_0$. The radiation intensity (2.4) is expanded as

$$\int_V \boldsymbol{J}(\boldsymbol{r}) \mathrm{e}^{\mathrm{j} k \hat{\boldsymbol{k}} \cdot \boldsymbol{r}} \,\mathrm{dV} = \int_V \boldsymbol{J}^{(0)}(\boldsymbol{r}) + k \boldsymbol{J}^{(1)}(\boldsymbol{r}) + \mathrm{j} k \hat{\boldsymbol{k}} \cdot \boldsymbol{r} \boldsymbol{J}^{(0)}(\boldsymbol{r}) + \mathcal{O}(k^2) \,\mathrm{dV}$$
$$= -k \int_V \boldsymbol{r} \nabla \cdot \boldsymbol{J}^{(1)}(\boldsymbol{r}) + \frac{\mathrm{j}}{2} \hat{\boldsymbol{k}} \times (\boldsymbol{r} \times \boldsymbol{J}^{(0)}(\boldsymbol{r})) \,\mathrm{dV} + \mathcal{O}(k^2), \quad (3.1)$$

as $k \to 0$, see [20]. We observe that the first term corresponds to an electric dipole and the second term to a magnetic dipole. The stored electric (2.5) and magnetic (2.6) energies have the low-frequency expansions [4, 21, 22]

$$w^{(\mathrm{e})} = k^2 \int_V \int_V \frac{\rho(\boldsymbol{r}_1)\rho^*(\boldsymbol{r}_2)}{|\boldsymbol{r}_1 - \boldsymbol{r}_2|} \, \mathrm{d}V_1 \, \mathrm{d}V_2 \tag{3.2}$$

and

$$w^{(\mathrm{m})} = k^2 \int_V \int_V \frac{\boldsymbol{J}^{(0)}(\boldsymbol{r}_1) \cdot \boldsymbol{J}^{(0)*}(\boldsymbol{r}_2)}{|\boldsymbol{r}_1 - \boldsymbol{r}_2|} \, \mathrm{d}V_1 \, \mathrm{d}V_2, \tag{3.3}$$

respectively. Insert the last three expressions into (2.8) to get the bound

$$\frac{D}{Q} \leqslant \max_{\rho, \boldsymbol{J}^{(0)}} \frac{k^3 \left| \int_V \hat{\boldsymbol{e}}^* \cdot \boldsymbol{r}\rho(\boldsymbol{r}) + \frac{1}{2}\hat{\boldsymbol{h}}^* \times \boldsymbol{r} \cdot \boldsymbol{J}^{(0)}(\boldsymbol{r}) \, \mathrm{d}V \right|^2}{\max\left\{ \iint_V \frac{\rho_1 \rho_2^*}{R_{12}} \, \mathrm{d}V_1 \, \mathrm{d}V_2, \iint_V \frac{\boldsymbol{J}_1^{(0)} \cdot \boldsymbol{J}_2^{(0)*}}{R_{12}} \, \mathrm{d}V_1 \, \mathrm{d}V_2 \right\}}, \tag{3.4}$$

where we have used the magnetic polarization $\hat{\boldsymbol{h}} = \hat{\boldsymbol{k}} \times \hat{\boldsymbol{e}}$ and the notation $\rho_n = \rho(\boldsymbol{r}_n)$ and $\boldsymbol{J}_n^{(0)} = \boldsymbol{J}^{(0)}(\boldsymbol{r}_n)$, $n = 1, 2$. We observe that the optimization decouples in ρ and $\boldsymbol{J}^{(0)}$, see [10]. The case with $\boldsymbol{J}^{(0)} = \boldsymbol{0}$ corresponds to an antenna radiating as an electric dipole and it is analyzed in Sec. 3.1. The case with $\rho = 0$ corresponds to an antenna radiating as a magnetic dipole and it is analyzed in Sec. 3.2. In general, both quantities can be non-zero and this case is discussed in Sec. 3.3.

3.1 Electric Dipole

A small antenna that radiates as an electric dipole, *i.e.*, $\boldsymbol{J}^{(0)} = \boldsymbol{0}$ in (3.4), gives the maximization problem:

$$\frac{D_{\mathrm{e}}}{Q_{\mathrm{e}}} \leqslant \max_{\rho} \frac{k^3}{4\pi} \frac{\left| \int_V \hat{\boldsymbol{e}}^* \cdot \boldsymbol{r}\rho(\boldsymbol{r}) \, \mathrm{d}V \right|^2}{\int_V \int_V \frac{\rho(\boldsymbol{r}_1)\rho^*(\boldsymbol{r}_2)}{4\pi|\boldsymbol{r}_1 - \boldsymbol{r}_2|} \, \mathrm{d}V_1 \, \mathrm{d}V_2}. \tag{3.5}$$

The term 4π is included to simplify the identification with the free space Green's function.

Consider the optimization problem:

$$\text{maximize}_{\rho} \frac{\left| \int_V \hat{\boldsymbol{e}}^* \cdot \boldsymbol{r}\rho(\boldsymbol{r}) \, \mathrm{d}V \right|^2}{\int_V \int_V \frac{\rho(\boldsymbol{r}_1)\rho^*(\boldsymbol{r}_2)}{4\pi|\boldsymbol{r}_1 - \boldsymbol{r}_2|} \, \mathrm{d}V_1 \, \mathrm{d}V_2}, \tag{3.6}$$

subject to the constraint $\int_V \rho \, \mathrm{dV} = -\mathrm{j} \int_{\partial V} \hat{\boldsymbol{n}} \cdot \boldsymbol{J}^{(1)} \, \mathrm{dS} = 0$ that follows from the continuity of the normal component of the current density, *i.e.*, $\hat{\boldsymbol{n}} \cdot \boldsymbol{J}^{(1)} = 0$ at the boundary. We note that this maximization problem is homogeneous for scalings $\rho \to \alpha\rho$ and, if ρ_a is a solution to (3.6), then $\rho_b = \rho_a / \int \hat{\boldsymbol{e}}^* \cdot \boldsymbol{r} \rho_a \, \mathrm{dV}$ is another solution to it. Thus, (3.6) can be rewritten as

$$\text{minimize}_\rho \int_V \int_V \frac{\rho(\boldsymbol{r}_1)\rho^*(\boldsymbol{r}_2)}{4\pi|\boldsymbol{r}_1 - \boldsymbol{r}_2|} \, \mathrm{dV}_1 \, \mathrm{dV}_2, \qquad (3.7)$$

subject to the scaling invariant constraints $\int \hat{\boldsymbol{e}}^* \cdot \boldsymbol{r}\rho(\boldsymbol{r}) \, \mathrm{dV} = E_0\gamma$ and the charge conservation constraint $\int \rho(\boldsymbol{r}) \, \mathrm{dV} = 0$, where $E_0 \in \mathbb{C}$ and $\gamma \in \mathbb{R}$ are constants. This is a standard minimization problem that is easily solved by introducing basis functions for ρ and using Lagrange multipliers [16]. We can also write the solution as an integral equation using a variational formulation, see also [22] for a corresponding variational approach to minimize the Q-value. The minimum of (3.7) is stationary with respect to variations $\rho \to \rho + \delta\rho'$ as $\delta \to 0$. To the first order in δ, we get

$$\int_V \rho'(\boldsymbol{r}_2) \int_V \frac{\rho^*(\boldsymbol{r}_1)}{4\pi|\boldsymbol{r}_1 - \boldsymbol{r}_2|} \, \mathrm{dV}_1 \, \mathrm{dV}_2 = 0, \qquad (3.8)$$

together with

$$\int_V \hat{\boldsymbol{e}}^* \cdot \boldsymbol{r}\rho'(\boldsymbol{r}) \, \mathrm{dV} = 0 \quad \text{and} \quad \int_V \rho'(\boldsymbol{r}) \, \mathrm{dV} = 0, \qquad (3.9)$$

for all $\rho'(\boldsymbol{r})$. This shows that ρ satisfies the volume integral equation

$$\int_V \frac{\rho(\boldsymbol{r}_1)}{4\pi|\boldsymbol{r}_1 - \boldsymbol{r}_2|} \, \mathrm{dV}_1 = E_0\hat{\boldsymbol{e}} \cdot \boldsymbol{r}_2 + C \quad \text{for } \boldsymbol{r}_2 \in V, \qquad (3.10)$$

where E_0 is the constant introduced above and the constant C is determined from the condition $\int \rho(\boldsymbol{r}) \, \mathrm{dV} = 0$. This is an integral equation for the region V with constant potential and zero total charge in a homogeneous exterior electric field $E_0\hat{\boldsymbol{e}}$. Applying ∇^2 to (3.10) shows that $\rho(\boldsymbol{r}_2) = 0$ for $\boldsymbol{r}_2 \in V \setminus \partial V$. The solution is hence given by the surface charge density ρ_s, determined from the boundary integral equation

$$\int_{\partial V} \frac{\rho_\mathrm{s}(\boldsymbol{r}_1)}{4\pi|\boldsymbol{r}_1 - \boldsymbol{r}_2|} \, \mathrm{dS}_1 = E_0\hat{\boldsymbol{e}} \cdot \boldsymbol{r}_2 + C \quad \text{for } \boldsymbol{r}_2 \in \partial V. \qquad (3.11)$$

This is the integral equation for the charge density used in the computation of the high-contrast polarizability dyadics [14]. Rewriting (3.5) by making use of the previous results, we get

$$\frac{D_\mathrm{e}}{Q_\mathrm{e}} \leqslant \frac{k^3}{4\pi} \frac{|E_0|^2\gamma^2}{\displaystyle\int_{\partial V} \int_{\partial V} \frac{\rho_\mathrm{s}(\boldsymbol{r}_1)\rho_\mathrm{s}^*(\boldsymbol{r}_2)}{4\pi|\boldsymbol{r}_1 - \boldsymbol{r}_2|} \, \mathrm{dS}_1 \, \mathrm{dS}_2} = \frac{k^3}{4\pi}\gamma. \qquad (3.12)$$
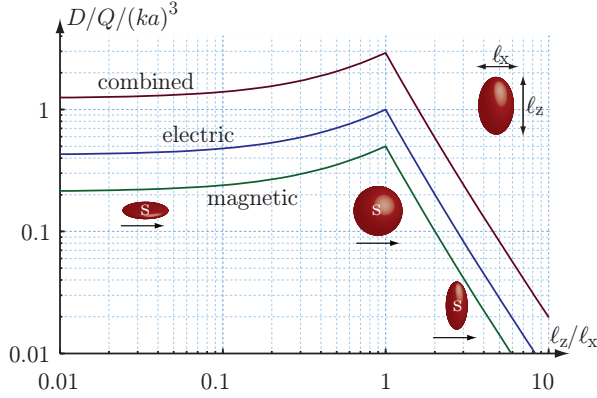
Figure 2: Bounds on $D/(Qk^3a^3)$ for a spheroid with height ℓ_z, width ℓ_x, electric polarization $\hat{e} = \hat{x}$, and $a = \max\{\ell_x, \ell_z\}/2$.

Using the high-contrast polarizability dyadic of the region V,

$$\gamma = \hat{e}^* \cdot \boldsymbol{\gamma}_\infty \cdot \hat{e} = \frac{1}{E_0} \int_{\partial V} \hat{e}^* \cdot \boldsymbol{r} \rho_s(\boldsymbol{r}) \, \mathrm{dS}, \qquad (3.13)$$

we obtain the final bound

$$\frac{D_e(\hat{\boldsymbol{k}}, \hat{e})}{Q_e} \leqslant \frac{k^3}{4\pi} \hat{e}^* \cdot \boldsymbol{\gamma}_\infty \cdot \hat{e}. \qquad (3.14)$$

The bound (3.12) is identical to the bound in [7,8] for the generalized absorption efficiency $\eta = 1/2$. This verifies that $\eta = 1/2$ for small dipole antennas as shown in [5]. It is also observed that $\eta \approx 1/2$ for many narrow band, $Q \gg 1$, minimum scattering antennas, *i.e.*, it is not required that $ka \to 0$ for the bound in [7,8] to hold.

The bound (3.14) is illustrated in Fig. 2 for a spheroid with height ℓ_z, width ℓ_x, and polarization $\hat{e} = \hat{x}$, see [10] for details[1]. It is observed that $D_e/Q_e \leqslant k^3a^3$ for a sphere $\ell_x = \ell_z$. This can also be written $Q_e \geqslant 3/(2k^3a^3)$ as $D = 3/2$ for small dipole antennas. This is identical to the bound by Thal [18]. The bound approaches $D_e/Q_e \leqslant 4k^3a^3/(3\pi)$ and $Q_e \geqslant 9\pi/(8k^3a^3)$ in the limit of a circular disc $\ell_z = 0$, see also [7–9, 25].

---

[1]see also http://www.mathworks.com/matlabcentral/fileexchange/26806-antennaq

3.2   Magnetic Dipole

The corresponding magnetic dipole radiator is obtained when $\rho = 0$ in (3.4) and its D/Q performance is bounded by

$$\frac{D_{\mathrm{m}}}{Q_{\mathrm{m}}} \leqslant \frac{k^3}{4\pi} \max_{\boldsymbol{J}^{(0)}} \frac{\left| \int_V \frac{1}{2} \hat{\boldsymbol{h}}^* \times \boldsymbol{r} \cdot \boldsymbol{J}^{(0)}(\boldsymbol{r}) \, \mathrm{d}V \right|^2}{\int_V \int_V \frac{\boldsymbol{J}^{(0)}(\boldsymbol{r}_1) \cdot \boldsymbol{J}^{(0)*}(\boldsymbol{r}_2)}{4\pi |\boldsymbol{r}_1 - \boldsymbol{r}_2|} \, \mathrm{d}V_1 \, \mathrm{d}V_2}, \qquad (3.15)$$

where $\hat{\boldsymbol{h}} = \hat{\boldsymbol{k}} \times \hat{\boldsymbol{e}}$. We use the amplitude scaling invariance to rewrite the minimization problem as

$$\text{minimize}_{\boldsymbol{J}^{(0)}} \int_V \int_V \frac{\boldsymbol{J}^{(0)}(\boldsymbol{r}_1) \cdot \boldsymbol{J}^{(0)*}(\boldsymbol{r}_2)}{4\pi |\boldsymbol{r}_1 - \boldsymbol{r}_2|} \, \mathrm{d}V_1 \, \mathrm{d}V_2, \qquad (3.16)$$

subject to the constraints $\nabla \cdot \boldsymbol{J}^{(0)} = 0$ and $\frac{1}{2} \int_V \hat{\boldsymbol{h}}^* \times \boldsymbol{r} \cdot \boldsymbol{J}^{(0)}(\boldsymbol{r}) \, \mathrm{d}V = H_0 \nu$, where $H_0 \in \mathbb{C}$ and $\nu \in \mathbb{R}$ are constants. The perturbation $\boldsymbol{J}^{(0)} \to \boldsymbol{J}^{(0)} + \delta \boldsymbol{J}^{(0)'}$ shows that

$$\int_V \boldsymbol{J}^{(0)'}(\boldsymbol{r}_2) \cdot \int_V \frac{\boldsymbol{J}^{(0)*}(\boldsymbol{r}_1)}{4\pi |\boldsymbol{r}_1 - \boldsymbol{r}_2|} \, \mathrm{d}V_1 \, \mathrm{d}V_2 = 0, \qquad (3.17)$$

$$\int_V \hat{\boldsymbol{h}}^* \times \boldsymbol{r} \cdot \boldsymbol{J}^{(0)'}(\boldsymbol{r}) \, \mathrm{d}V = 0, \qquad (3.18)$$

and $\nabla \cdot \boldsymbol{J}^{(0)'} = 0$. Thus, the solution satisfies the following volume integral equation:

$$\int_V \frac{\boldsymbol{J}^{(0)}(\boldsymbol{r}_1)}{4\pi |\boldsymbol{r}_1 - \boldsymbol{r}_2|} \, \mathrm{d}V_1 = \frac{H_0}{2} \hat{\boldsymbol{h}} \times \boldsymbol{r}_2 + \nabla \psi(\boldsymbol{r}_2) \quad \text{for } \boldsymbol{r}_2 \in V, \qquad (3.19)$$

where $\psi(\boldsymbol{r}_2)$ is an arbitrary function to account for the constraint $\nabla \cdot \boldsymbol{J}^{(0)} = 0$, assuming sufficient constraint on the regularity of the domain (*e.g.*, Lipschitz) and functions that Green's formula hold see *e.g.*, [15]. Taking the divergence of the above equation and using $\hat{\boldsymbol{n}}(\boldsymbol{r}) \cdot \boldsymbol{J}^{(0)}(\boldsymbol{r}) = 0$ for $\boldsymbol{r} \in \partial V$, shows that $\nabla^2 \psi(\boldsymbol{r}_2) = 0$ for $\boldsymbol{r}_2 \in V$. Applying $\nabla \times \nabla \times \cdot$ to (3.19) implies that $\boldsymbol{J}^{(0)}(\boldsymbol{r}_2) = \boldsymbol{0}$ for $\boldsymbol{r}_2 \in V \backslash \partial V$. This gives the boundary integral equation for the surface current density $\boldsymbol{J}_{\mathrm{s}}^{(0)}(\boldsymbol{r}_1)$ as:

$$\hat{\boldsymbol{n}} \times \int_{\partial V} \frac{\boldsymbol{J}_{\mathrm{s}}^{(0)}(\boldsymbol{r}_1)}{4\pi |\boldsymbol{r}_1 - \boldsymbol{r}_2|} \, \mathrm{d}S_1 = \frac{H_0}{2} \hat{\boldsymbol{n}} \times (\hat{\boldsymbol{h}} \times \boldsymbol{r}_2) + \hat{\boldsymbol{n}} \times \nabla \psi(\boldsymbol{r}_2) \quad \text{for } \boldsymbol{r}_2 \in \partial V. \ (3.20)$$

Note that the restrictions to the tangential components follow from the vanishing normal component of the current density at the boundary, *i.e.*, $\hat{\boldsymbol{n}} \cdot \boldsymbol{J}^{(0)'}(\boldsymbol{r}_2) = 0$ for $\boldsymbol{r}_2 \in \partial V$ in (3.17).

The bound for the optimizing $\boldsymbol{J}_{\mathrm{s}}$ (3.15) becomes

$$\frac{D_{\mathrm{m}}}{Q_{\mathrm{m}}} \leqslant \frac{k^3}{4\pi} \frac{|H_0|^2 \nu^2}{\displaystyle\int_{\partial V} \int_{\partial V} \frac{\boldsymbol{J}_{\mathrm{s}}^{(0)}(\boldsymbol{r}_1) \cdot \boldsymbol{J}_{\mathrm{s}}^{(0)*}(\boldsymbol{r}_2)}{4\pi |\boldsymbol{r}_1 - \boldsymbol{r}_2|} \, \mathrm{dS}_1 \, \mathrm{dS}_2} = \frac{k^3}{4\pi} \nu. \qquad (3.21)$$

where we identify ν as the $\hat{\boldsymbol{h}}$-component of the magnetic moment.

The bound for a spheroid with $\hat{\boldsymbol{h}} = \hat{\boldsymbol{z}}$ and surface currents $\boldsymbol{J} = J_\phi \hat{\boldsymbol{\phi}}$ is depicted in Fig. 2. It is observed that $D_{\mathrm{m}}/Q_{\mathrm{m}} = D_{\mathrm{e}}/(2Q_{\mathrm{e}})$ for this case, see also [10]. In particular this gives $D_{\mathrm{m}}/Q_{\mathrm{m}} \leqslant k^3 a^3/2$ and $D_{\mathrm{m}}/Q_{\mathrm{m}} \leqslant k^3 a^3 8/3$ for spheres and discs, respectively.

3.3   Combined Electric and Magnetic Dipoles

Maximization of (3.4) is given by the combination of the electric and magnetic dipole cases. It is first observed that

$$\max_{a,b} \frac{|\alpha a + \beta b|^2}{\max\{|a|^2, |b|^2\}} = (\alpha + \beta)^2, \qquad (3.22)$$

for $\alpha \geqslant 0$ and $\beta \geqslant 0$, see [10]. Replace α and β with the electric (3.12) and magnetic (3.15) cases, i.e., $\alpha = \sqrt{D_{\mathrm{e}}/Q_{\mathrm{e}}}$ and $\beta = \sqrt{D_{\mathrm{m}}/Q_{\mathrm{m}}}$ to obtain the bound for combined electric and magnetic dipole radiators:

$$\frac{D}{Q} \leqslant \left(\sqrt{\frac{D_{\mathrm{e}}}{Q_{\mathrm{e}}}} + \sqrt{\frac{D_{\mathrm{m}}}{Q_{\mathrm{m}}}} \right)^2 . \qquad (3.23)$$

The combined bound (3.23) is depicted in Fig. 2 for a sphere with polarization $\hat{\boldsymbol{e}} = \hat{\boldsymbol{x}}$. It is seen that $D/Q \leqslant (1 + \sqrt{1/2})^2 k^3 a^3 \approx 2.9 k^3 a^3$ for this case. For an electrically small, spherical radiator, the bound reads $D/Q \leqslant 2.9 k_0^3 a^3$. Note that the bound in [7, 8] is sharper than (3.23) for linearly polarized antennas; see also [6] for the circular polarization case.

The upper bound (3.23) requires that the electric and magnetic dipoles contribute equally and have the polarization $\hat{\boldsymbol{e}}$. This gives the partial directivity $D = 3$ and implies that $Q \geqslant 3/2.9 (ka)^{-3}$ for a spherical region. This is similar to the combined TE and TM bound in [19].

4   Non Electrically Small Antennas

The general expression (2.8) offers the possibility to analyze D/Q in terms of the current, $\boldsymbol{J}$, that flows on the antenna. It also offers the possibility to optimize an antenna with respect to its D/Q performance. In order to increase the D/Q ratio, we make the assumption that either the stored electric or magnetic energy is greater than the other.

4.1   Optimization Formulation for D/Q

We illustrate the maximization of (2.8) assuming that the stored electric energy is greater than the stored magnetic energy. Thus, using the amplitude scaling invariance in (2.8), the maximization problem can be reformulated as the following minimization problem:

$$
\text{minimize}_{\boldsymbol{J}} \int_V \int_V \nabla_1 \cdot \boldsymbol{J}_1 \nabla_2 \cdot \boldsymbol{J}_2^* \frac{\cos(kR_{12})}{R_{12}}
$$
$$
- \frac{k}{2} \big(k^2 \boldsymbol{J}_1 \cdot \boldsymbol{J}_2^* - \nabla_1 \cdot \boldsymbol{J}_1 \nabla_2 \cdot \boldsymbol{J}_2^* \big) \sin(kR_{12}) \, \mathrm{dV}_1 \, \mathrm{dV}_2, \quad (4.1)
$$

subject to the constraint

$$
\left| \int_V \hat{\boldsymbol{e}}^* \cdot \boldsymbol{J}(\boldsymbol{r}) \mathrm{e}^{\mathrm{j}k\hat{\boldsymbol{k}}\cdot\boldsymbol{r}} \, \mathrm{d}V \right| = 1. \tag{4.2}
$$

To account for the appropriate class of admissible current densities we also impose the condition

$$
\hat{\boldsymbol{n}} \cdot \boldsymbol{J}(\boldsymbol{r}) = 0 \quad \text{for } \boldsymbol{r} \in \partial V. \tag{4.3}
$$

The first constraint can be reduced to

$$
\int_V \hat{\boldsymbol{e}}^* \cdot \boldsymbol{J}(\boldsymbol{r}) \mathrm{e}^{\mathrm{j}k\hat{\boldsymbol{k}}\cdot\boldsymbol{r}} \, \mathrm{d}V = 1, \tag{4.4}
$$

using the amplitude scale invariance in (2.8), see Sec. 2.

An alternative technique to the variational method of Sec. 3 for obtaining the optimal currents is described in the following. We represent the current densities in appropriate basis functions $\boldsymbol{\psi}_m$,

$$
\boldsymbol{J}(\boldsymbol{r}) = \sum_{m=1}^M J_m \boldsymbol{\psi}_m(\boldsymbol{r}), \tag{4.5}
$$

and denote $\mathbf{J} = (J_1, J_2, \ldots, J_M)^\mathrm{T}$. Introduce the matrix $\mathbf{C}$ with elements

$$
C_{mn} = \int_V \int_V \nabla_1 \cdot \boldsymbol{\psi}_m(\boldsymbol{r}_1) \nabla_2 \cdot \boldsymbol{\psi}_n(\boldsymbol{r}_2) \frac{\cos(k|\boldsymbol{r}_1 - \boldsymbol{r}_2|)}{|\boldsymbol{r}_1 - \boldsymbol{r}_2|}
$$
$$
- \frac{k}{2} \big(k^2 \boldsymbol{\psi}_m(\boldsymbol{r}_1) \cdot \boldsymbol{\psi}_n(\boldsymbol{r}_2) - \nabla_1 \cdot \boldsymbol{\psi}_m(\boldsymbol{r}_1) \nabla_2 \cdot \boldsymbol{\psi}_n(\boldsymbol{r}_2) \big) \sin(k|\boldsymbol{r}_1 - \boldsymbol{r}_2|) \, \mathrm{dV}_1 \, \mathrm{dV}_2
$$
$$
\tag{4.6}
$$

for $m, n = 1, 2, ..., M$. The equivalent minimization problem in this basis representation takes the form

$$
\min_{J_m} \sum_{m=1}^M \sum_{n=1}^M J_m^* C_{mn} J_n = \min_{\mathbf{J}} \mathbf{J}^\mathrm{H} \mathbf{C} \mathbf{J}, \tag{4.7}
$$

subject to the constraints

$$\sum_{m=1}^{M} J_m \int \hat{\boldsymbol{e}}^* \cdot \boldsymbol{\psi}_m(\boldsymbol{r}) \mathrm{e}^{\mathrm{j}k\hat{\boldsymbol{k}}\cdot\boldsymbol{r}} \, \mathrm{d}V = \sum_{m=1}^{M} A_{m,1}^* J_m = 1 \qquad (4.8)$$

and

$$\hat{\boldsymbol{n}} \cdot \boldsymbol{\psi}_m(\boldsymbol{r}) = 0 \quad \text{for } \boldsymbol{r} \in \partial V. \qquad (4.9)$$

In matrix notation $\mathbf{A}^{\mathrm{H}}\mathbf{J} = \mathbf{f}$, where: $A_{m,1}^* = \int \hat{\boldsymbol{e}}^* \cdot \boldsymbol{\psi}_m(\boldsymbol{r}) \mathrm{e}^{\mathrm{j}k\hat{\boldsymbol{k}}\cdot\boldsymbol{r}} \, \mathrm{d}V$, and $\mathbf{f} = 1$.

The optimization problem (4.7) to (4.9) is solvable using Lagrange multipliers $\boldsymbol{\nu}$, [16], resulting in the linear system

$$\begin{pmatrix} \mathbf{C} & \mathbf{A} \\ \mathbf{A}^{\mathrm{H}} & \mathbf{0} \end{pmatrix} \begin{pmatrix} \mathbf{J} \\ \boldsymbol{\nu} \end{pmatrix} = \begin{pmatrix} \mathbf{0} \\ \mathbf{f} \end{pmatrix}. \qquad (4.10)$$

Note that the constraint (4.9) can be included in the basis functions $\boldsymbol{\psi}_m$. Returning to the matrix $\mathbf{C}$ with elements given in (4.6), note that we can represent the first kernel with cosines as $\mathrm{Re}(G)$ where G is the Green's function corresponding to the scalar Helmholtz equation. Thus, with minor modifications on *e.g.*, a method of moments solver, we can implement the above outlined optimization problem. Below we illustrate the solutions of the optimization for planar rectangular structures.

4.2   Planar Rectangular Structures

Consider a planar rectangle in the xz-plane and broad side radiation $\hat{\boldsymbol{k}} = \hat{\boldsymbol{y}}$ with linear polarization $\hat{\boldsymbol{e}} = \hat{\boldsymbol{x}}$. A Helmholtz decomposition [15] of the surface current $\boldsymbol{J} = \nabla_{\mathrm{t}} J^{(\mathrm{g})} + \nabla_{\mathrm{t}} \times \boldsymbol{J}^{(\mathrm{c})}$ simplifies the corresponding electric energy (2.5) (and equivalently the matrix $\mathbf{C}$ in (4.6)), where ∇_{t} denotes the transverse part of ∇. It is seen that the radiation in the $\hat{\boldsymbol{y}}$-direction is independent of $\boldsymbol{J}^{(\mathrm{c})}$. This reduces the optimization problem (4.10) to the irrotational part of the current density, *i.e.*, we use $\boldsymbol{J}^{(\mathrm{c})} = \mathbf{0}$.

Optimization of the D/Q-ratio (2.8) using (4.10) yields the result shown in Fig. 3. The bound is depicted for $k\ell_{\mathrm{x}} = \{0, 0.1, 1, 2, 3\}$ and normalized with the electrical size $k^3 a^3$ to decrease the dependence on ka, where $a = (\ell_{\mathrm{x}}^2 + \ell_{\mathrm{z}}^2)^{1/2}$. It is observed that it is not possible to distinguish the $k\ell_{\mathrm{x}} = \{0, 0.1, 1\}$ cases in the figure and that the bound increases slightly for the $k\ell_{\mathrm{x}} = \{2, 3\}$ cases. The results for $k\ell_{\mathrm{x}} = \{2, 3\}$ are only shown when their corresponding Q-factors are sufficiently large, see the corresponding Q-values in Fig. 4. This means that there are no severe bounds on Q for these rather large structures. Note that $ka \approx 10$ for $k\ell_{\mathrm{x}} = 2$ and $\ell_{\mathrm{z}}/\ell_{\mathrm{x}} = 20$. The figures also contain the asymptotic expressions in [10] where it is assumed that the current is of the form $\boldsymbol{J} = J_{\mathrm{x}}(x)\hat{\boldsymbol{x}}$ and $k\ell_{\mathrm{z}} \gg 1$.
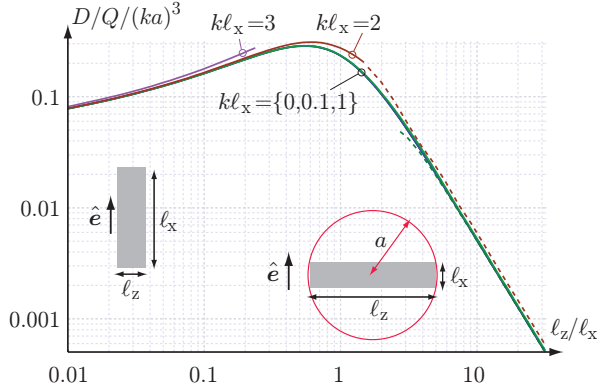
Figure 3: Bound on D/Q for a planar rectangle with sides ℓ_x and ℓ_z for $k\ell_x = \{0, 0.1, 1, 2, 3\}$ and $\hat{\boldsymbol{k}} = \hat{\boldsymbol{y}}$ normal to the rectangle and $\hat{\boldsymbol{e}} = \hat{\boldsymbol{x}}$. The solid curves show the bounds determined for irrotational surface currents, $\nabla_t \times \boldsymbol{J} = \boldsymbol{0}$, using (4.10). The dashed curves show the corresponding asymptotic results in [10].
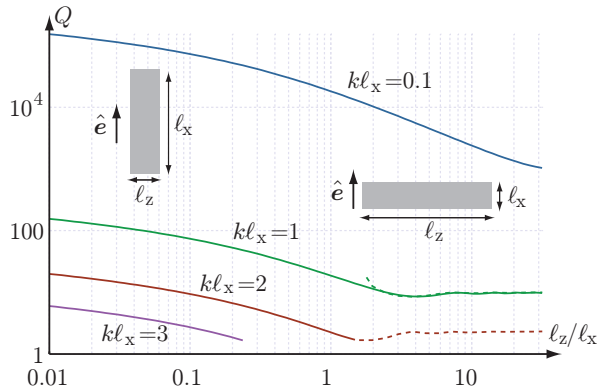
Figure 4: Resulting Q factors for planar rectangles with sides ℓ_x and ℓ_z for $k\ell_x = \{0, 0.1, 1, 2, 3\}$ and $\hat{\boldsymbol{k}} = \hat{\boldsymbol{y}}$ normal to the rectangle and $\hat{\boldsymbol{e}} = \hat{\boldsymbol{x}}$ from the D/Q bound in Fig. 3. The solid and dashed curves show the results for arbitrary irrotational surface currents, $\nabla_t \times \boldsymbol{J} = \boldsymbol{0}$, using (4.10) and the asymptotic expression in [10], respectively.

5 Numerical examples

We illustrate the theoretical results with numerical examples of some current distributions on spherical regions, current distributions and bounds on strip dipoles, and planar rectangular array antennas.

5.1 Spherical Region

It is observed that the currents that generate the optimal D/Q-ratios are not unique. We illustrate this for a simple electric case, in the limit of small ka so that we can use the variational formulation in (3.5). Consider a spherical volume of radius a and electric polarization $\hat{e} = \hat{z}$. The optimal charge distribution determined from (3.11) is of the form $\rho(\theta, \phi) = \rho_0 \cos \theta$. The corresponding surface current density satisfies $\nabla \cdot \boldsymbol{J} = -\mathrm{j}k\rho$ (recall $\rho_{\mathrm{SI}} = \rho/c_0$) on the surface of the sphere. This gives

$$\frac{\partial}{\partial \theta}\big(\sin \theta J_\theta\big) + \frac{\partial J_\phi}{\partial \phi} = \frac{-\mathrm{j}ka\rho_0 \sin(2\theta)}{2} \tag{5.1}$$

This equation has many solutions, *e.g.*, all the functions of the form

$$\boldsymbol{J} = J_{\theta 0}\hat{\boldsymbol{\theta}}\big(\sin \theta - \frac{\beta}{\sin \theta}\big) + \frac{1}{\sin \theta}\frac{\partial A}{\partial \phi}\hat{\boldsymbol{\theta}} - \frac{\partial A}{\partial \theta}\hat{\boldsymbol{\phi}} \tag{5.2}$$

where $J_{\theta 0} = -\mathrm{j}ka\rho_0$, β is a constant, and $A = A(\theta, \phi)$.

The simplest solution to (5.1) is a rotationally symmetric current density in the $\hat{\boldsymbol{\theta}}$-direction that vanishes as $\theta = 0$ and $\theta = \pi$, *i.e.*, $\boldsymbol{J} = \hat{\boldsymbol{\theta}}J_{\theta 0} \sin \theta$. This is a surface current density that generates a single spherical TM mode. It is noted that the surface current density on a folded spherical dipole has this form, see Fig. 5a. An alternative solution is obtained by the requirement that the current density vanishes at $\theta = \pi/2$. This gives the solution $\boldsymbol{J} = J_{\theta 0}\hat{\boldsymbol{\theta}}(\sin \theta - 1/\sin \theta)$, see Fig. 5b. This surface current density is infinite at $\theta = 0$ and $\theta = \pi$ and resembles the current density on a capped spherical dipole [17]. A third solution is offered by $\beta = 0$ and $A = A(\theta)$. In particular, we consider the surface current density $\boldsymbol{J} = J_{\theta 0}\big(0.15\hat{\boldsymbol{\theta}} \sin \theta - \hat{\boldsymbol{\phi}} \operatorname{sign}(\cos \theta) \sin^2 \theta\big)$, as this solution is similar to the current density on a spherical folded helix, see Fig. 5c.

5.2 Strip Dipole Antennas

The optimal current distributions are determined for rectangles with side lengths $\ell_{\mathrm{y}} = \xi\ell_{\mathrm{x}}$ with $\xi = \{0.1, 0.01, 0.001\}$ using (4.10) for $ka \leqslant 2$. The surface current in the center $\boldsymbol{J}(x, 0) = J_{\mathrm{x}}(x)\hat{\boldsymbol{x}}$ is depicted in Fig. 6 for the half-wave antenna, *i.e.*, $ka \approx 1.5$, where $a = (\ell_{\mathrm{x}}^2 + \ell_{\mathrm{y}}^2)^{1/2}/2$. It is observed that the currents resemble the commonly assumed $\cos(\pi x/\ell_{\mathrm{x}})$ shape.

The corresponding bound on D/Q normalized with $(ka)^3$ is shown in Fig. 7. Here it is seen that the performance improves with the width of the rectangle.
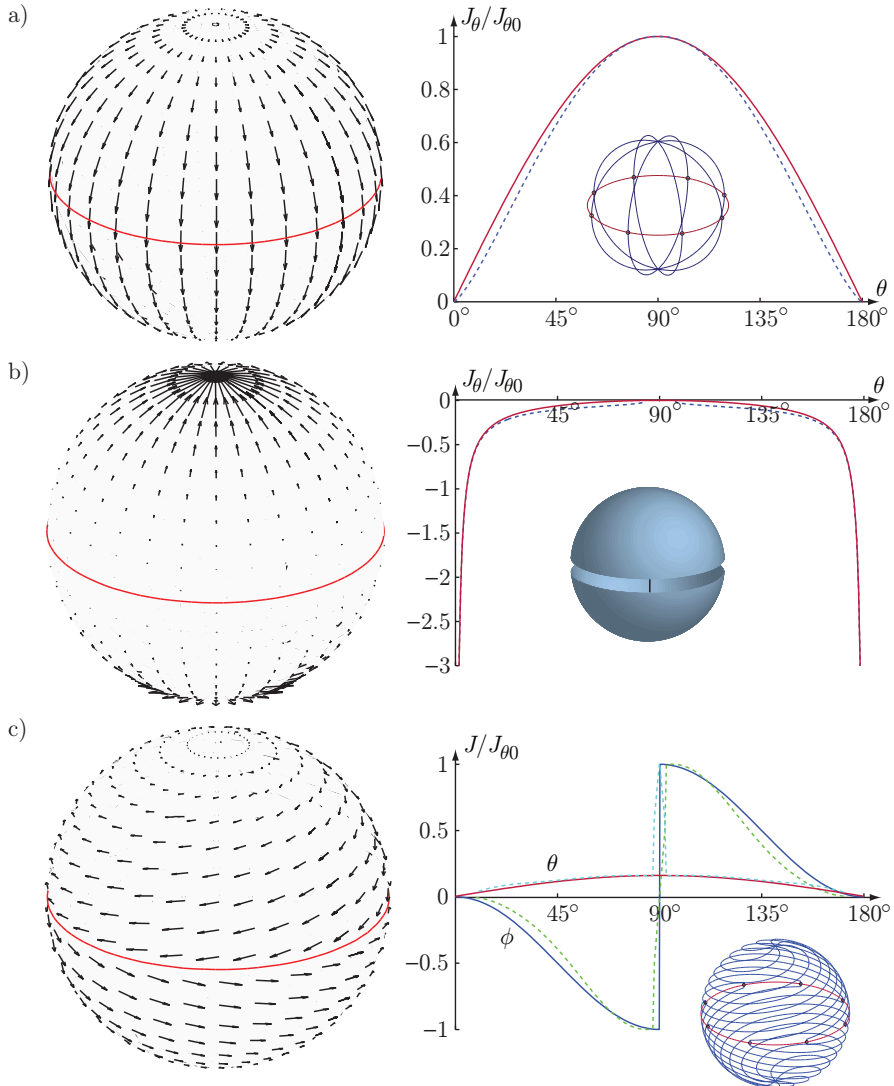
Figure 5: Examples of surface current distributions on spheres with the surface charge density $\rho = \rho_0 \cos\theta$. a) folded spherical dipole with $\boldsymbol{J} \approx J_{\theta 0}\hat{\boldsymbol{\theta}}\sin\theta$. b) capped spherical dipole with $\boldsymbol{J} \approx J_{\theta 0}\hat{\boldsymbol{\theta}}(\sin\theta - 1/\sin\theta)$. c) folded spherical helix with $\boldsymbol{J} \approx J_{\theta 0}\big(0.15\hat{\boldsymbol{\theta}}\sin\theta - \hat{\boldsymbol{\phi}}\,\mathrm{sign}(\cos\theta)\sin^2\theta\big)$.
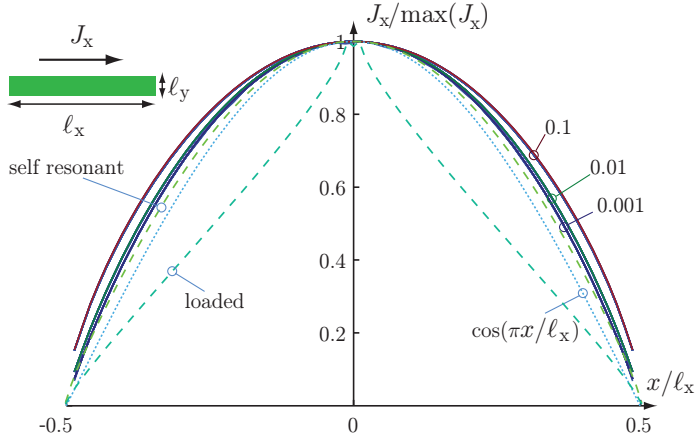
Figure 6: Optimal current distribution (4.10) for planar rectangles with side lengths $\ell_y = \xi \ell_x$ with $\xi = \{0.1, 0.01, 0.001\}$ and $ka = 1.5$ (solid curves). Simulated currents on a strip dipole for the inductively loaded and self-resonant case respectively with $\ell_y = 0.01\ell_x$ for $ka \approx \{0.28, 1.49\}$ (dashed curves). Theoretical current distribution, $\cos(\pi x/\ell_x)$(dotted curve)

Moreover, $D/(Qk^3a^3)$ is nearly independent of the electrical size of the structure for $ka \leqslant 1.5$.

The resulting Q-factor is computed from the current distribution using the radiated power in [21], see Fig. 8. It is observed that Q decreases with the increase of the width of the strip. The directivity D is depicted in Fig. 9. Here, it is seen that the directivity increases with the electrical size of the object.

The bounds are compared with numerical results for a center fed strip dipole with $\ell_y = 0.01\ell_x$. The dipole is self-resonant for $ka \approx 1.49$ with the directivity $D \approx 1.63$. The Q-factor is estimated to $Q \approx 6$ using the differentiation of the impedance [11, 26]. These results are indicated with stars at $ka \approx 1.49$ in Figs 7 to 9. The corresponding current density is also depicted in Fig. 6. It is observed that the self-resonant dipole has a current distribution that resembles the optimal current distribution. The estimated values of D/Q, D, and Q are also close to the corresponding optimal values.

It is also illustrative to consider an inductively loaded strip dipole with the same dimensions. The loading decreases the resonance wave number to $ka \approx 0.28$ and the parameters are estimated to $D \approx 1.5$, $Q \approx 1250$, and $D/(Qk^3a^3) \approx 0.054$, see the stars at $ka \approx 0.28$ in Figs 7 to 9. It is observed that the performance of the loaded dipole is farther away from the optimum than the performance of the unloaded dipole. This is also seen from the shape of the current distribution in Fig. 6.
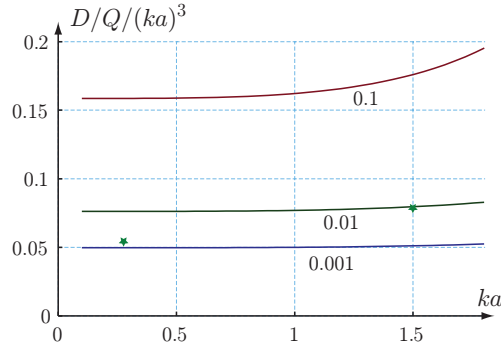
Figure 7: Bound on D/Q normalized with $k^3 a^3$ for a planar rectangle with side lengths $\ell_y = \xi \ell_x$ where $\xi = \{0.1, 0.01, 0.001\}$. The numerical results for strip dipoles with $\xi = 0.01$ and $ka \approx \{0.28, 1.49\}$ are indicated by the stars.
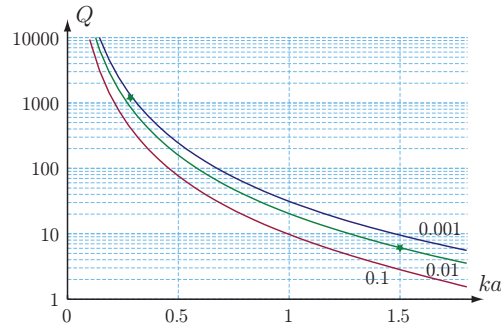
Figure 8: Q factor for the optimal current distributions corresponding to the D/Q bound in Fig. 7. The numerical results for strip dipoles with $\xi = 0.01$ and $ka \approx \{0.28, 1.49\}$ are indicated by the stars.
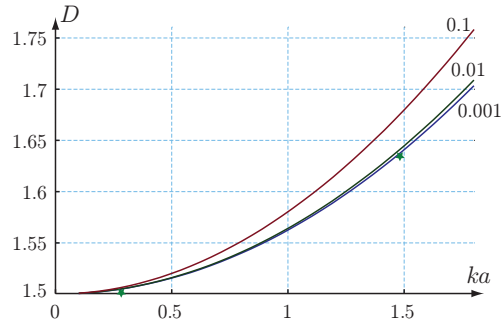
Figure 9: Directivity for the optimal current distributions corresponding to the D/Q bound in Fig. 7. The numerical results for strip dipoles with $\xi = 0.01$ and $ka \approx \{0.28, 1.49\}$ are indicated by the stars.
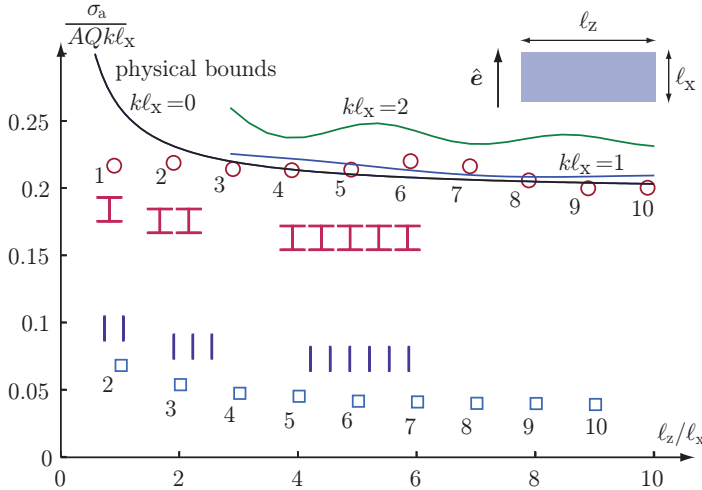
Figure 10: Illustrations of the physical bounds on the effective antenna aperture, σ_a, of planar rectangular circumscribing regions with height ℓ_x, width ℓ_z, and physical area $A = \ell_x \ell_z$.

5.3   Array Antennas

The performances of linear arrays are illustrated with numerical results using the method of moments (MoM) for dipole and capacitively loaded dipole elements. The one-dimensional dipole array consists of n elements with the length ℓ_x and the width $\Delta = \ell_x/50$ and inter-element spacing ℓ_x. This gives approximately arrays with half a wavelength, $\lambda_0/2$, spacing. The array is modeled as perfectly conducting with a gap feed model. The passive array is analyzed, where identical lumped resistances, R_0, are placed in the feed gaps. The resistance R_0 is determined by maximizing the effective antenna aperture at the first resonance frequency, see [13] for details.

The dipole array is compared with the physical bounds for antennas confined to rectangular regions, see Fig. 3. The electric polarization of the arrays is aligned with the ℓ_x-direction. The arrays with n elements are circumscribed by rectangles with height ℓ_x and width $\ell_z = (n-1)\ell_x + \ell_x/50$ for $n = 1, ..., 10$. The corresponding results are shown in Fig. 10, where the effective antenna aperture, σ_a, (absorption cross section) is normalized with the physical area, A. The physical bound is drawn for $k\ell_x = 0$ and the asymptotic result in [10] for $k\ell_x = \{1, 2\}$. It is observed that the performances of the capacitively loaded dipoles are close to the physical bound. The dipole array is a factor of $1/15$ below the physical bound. Using the polarization interpretation on the array of [13] we see that this is due to the reduction of polarizability of the dipole as compared with the rectangle.

6   Conclusions

Upper bounds on the directivity antenna Q quotient, D/Q, are derived based on a quadratic optimization problem. The D/Q quotient is formulated in the current density on the antenna structure as given from the radiation intensity and the expressions of the stored energies in [4, 21, 22]. The expression is not bases on a small antenna limit assumption opening the possibility to analyze electrically large structures. The optimization problem is solved analytically in the limit of small antennas and numerically using Lagrange parameters for arbitrary size antennas. The upper bounds are useful as they show how the shape and size of the antenna geometry affect the antenna performance [5, 7, 8]. They can also be used as a priori estimates of what can be expected from an antenna in a given geometry.

The closed form solution for small antennas expresses the bounds in the polarizability of the antenna structure. The bound on non-magnetic antenna structures is identical to the bound in [5, 7, 8] and agrees with the results in [25] for the directivity $D = 3/2$. In [22], Vandenbosch considered the corresponding bound on Q for small antennas using a line search optimization algorithm. In contrast, the results presented here are for D/Q where the bound can be solved analytically. This formulation distinguishes between the polarizations (linear, in different directions as well as circular). It is also shown that it is sufficient to consider surface currents in this small ka-limit. Moreover, the case with combined electric and magnetic dipoles is analyzed, where it is noted that the results resemble the mixed TE and TM bound in [18] for spherical regions.

We also illustrate that there are several current densities for a given charge density. The explicit solutions for a spherical region include current distributions that resemble the current on folded spherical dipoles, capped spherical dipoles, and folded spherical helices.

Lagrange multipliers are used to solve the D/Q optimization problem for finite size antennas. This reformulates the problem of obtaining the optimal current densities as a linear system that has many similarities with standard method of moments solvers. It is shown that the bound performs well for fairly large antennas with high directivity. It is illustrated that the stored electric energy in [21] can be negative for certain kinds of loop type currents on planar structures. Although this stored energy corresponds to a case that can cause numerical problems this can be mitigated with a Helmholtz decomposition of the current density.

Appendix A   Negative stored Electric Energy

In Sec. 4.2, we removed the loop-currents $\boldsymbol{J}^{(c)}$ through the observation that they do not contribute to the radiation in the normal direction. If the numerical optimization is done with these currents, it is observed that they may cause a
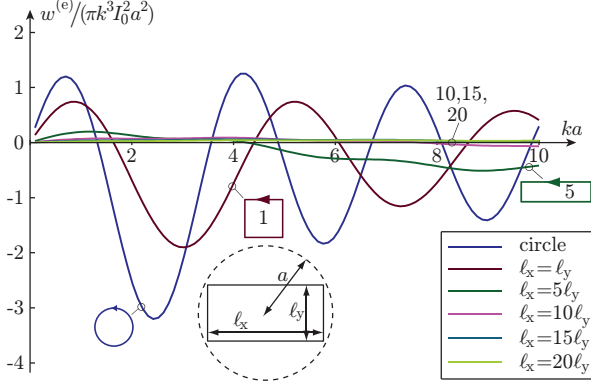
Figure 11: Stored electric energy for circular (A.1) and rectangular loop currents.

negative stored electric energy (2.5). This behavior of the stored electric energy is illustrated here using simple examples.

Consider first the following divergence free *i.e.*, $\nabla \cdot \boldsymbol{J} = 0$, current density $\boldsymbol{J}(\boldsymbol{r}) = I_0\delta(\varrho - a)\delta(z)\hat{\boldsymbol{\phi}}$, where δ denotes the Dirac delta distribution, I_0 is a constant that depends on the source of current, and the cylindrical coordinates (ϱ, ϕ, z) are used. In this case, the stored electric energy (2.5) reduces to

$$w^{(\mathrm{e})} = -\pi k^3 a^2 I_0^2 \int_0^{2\pi} \cos\phi \sin\left(2ka\sin\frac{\phi}{2}\right)\mathrm{d}\phi. \qquad (\mathrm{A.1})$$

Numerical integration shows that $w^{(\mathrm{e})}$ is positive for $ka < 1.5$, see Fig. 11. When the electric size of the structure increases, the electric energy becomes negative for some objects. It is noted that the corresponding stored magnetic energy is infinite for the considered current.

For a rectangular surface of dimensions $\ell_\mathrm{x}, \ell_\mathrm{y}$ we use the current density $\boldsymbol{J} = I_0\delta(z)\big((\delta(y + \ell_\mathrm{y}/2) - \delta(y - \ell_\mathrm{y}/2))\hat{\boldsymbol{x}} + (\delta(x - \ell_\mathrm{x}/2) - \delta(x + \ell_\mathrm{x}/2))\hat{\boldsymbol{y}}\big)$. The corresponding stored electrical energy is shown in Fig. 11.

It is important to note that the current used in (A.1) contains no phase or amplitude variation and it is a mathematical construction with the purpose of illustrating that direct optimization of (4.7) can be difficult. The total electric energy defined as the integral of $|\boldsymbol{E}|^2$ is also positive.

In Sec. 4, we used a Helmholtz decomposition to reduce the problem with the indefinite stored electric energy. This decomposition is motivated by the energy expressions for small antennas in Sec. 3, where it is observed that the stored magnetic energy dominates over the stored electric energy for divergence free

current densities, $\nabla \cdot \boldsymbol{J} = 0$. Moreover, the identity

$$\int_{\mathbb{R}^3} \int_{\mathbb{R}^3} \left((\nabla_1 \times \boldsymbol{J}_1) \cdot (\nabla_2 \times \boldsymbol{J}_2^*) + (\nabla_1 \cdot \boldsymbol{J}_1)(\nabla_2 \cdot \boldsymbol{J}_2^*) - k^2 \boldsymbol{J}_1 \cdot \boldsymbol{J}_2^*\right) \frac{\cos(kR_{12})}{R_{12}} \, \mathrm{dV}_1 \, \mathrm{dV}_2$$
$$= 4\pi \int_{\mathbb{R}^3} |\boldsymbol{J}|^2 \, \mathrm{dV} \quad \text{(A.2)}$$

for all smooth current densities $\boldsymbol{J}$ supported in a bounded region show that

$$w^{(\mathrm{e})} - w^{(\mathrm{m})} = 4\pi \int_{\mathbb{R}^3} |\boldsymbol{J}|^2 \, \mathrm{dV} \geqslant 0 \quad \text{(A.3)}$$

if $\nabla \times \boldsymbol{J} = \boldsymbol{0}$. This suggests that the Helmholtz decomposition [15] $\boldsymbol{J} = \nabla J^{(\mathrm{g})} + \nabla \times \boldsymbol{J}^{(\mathrm{c})}$ can be used to separate the currents into the dominantly electric and magnetic parts $\nabla J^{(\mathrm{g})}$ and $\nabla \times \boldsymbol{J}^{(\mathrm{c})}$, respectively. It is also noted that the decomposition into spherical TE and TM modes in [12] is based on a similar factorization.

References

[1] Antenna Standards Committee of the IEEE Antennas and Propagation Society. IEEE Standard Definitions of Terms for Antennas, 1993. IEEE Std 145-1993.

[2] S. R. Best. Low Q electrically small linear and elliptical polarized spherical dipole antennas. *IEEE Trans. Antennas Propagat.*, **53**(3), 1047–1053, 2005.

[3] L. J. Chu. Physical Limitations of Omnidirectional Antennas. *J. Appl. Phys.*, **19**, 1163–1175, 1948.

[4] W. Geyi. A method for the evaluation of small antenna Q. *IEEE Trans. Antennas Propagat.*, **51**(8), 2124–2129, 2003.

[5] M. Gustafsson, M. Cismasu, and S. Nordebo. Absorption efficiency and physical bounds on antennas. *International Journal of Antennas and Propagation*, **2010**(Article ID 946746), 1–7, 2010.

[6] M. Gustafsson and C. Sohl. New physical bounds on elliptically polarized antennas. In *Proceedings of the Third European Conference on Antennas and Propagation*, pages 400–402, Berlin, Germany, March 23–27 2009. The Institution of Engineering and Technology.

[7] M. Gustafsson, C. Sohl, and G. Kristensson. Physical limitations on antennas of arbitrary shape. *Proc. R. Soc. A*, **463**, 2589–2607, 2007.

[8] M. Gustafsson, C. Sohl, and G. Kristensson. Illustrations of new physical bounds on linearly polarized antennas. *IEEE Trans. Antennas Propagat.*, **57**(5), 1319–1327, May 2009.

[9] M. Gustafsson. Polarizability and physical bounds on antennas in cylindrical and rectangular geometries. Technical Report LUTEDX/(TEAT-7195)/1-11/(2010), Lund University, Department of Electrical and Information Technology, P.O. Box 118, S-221 00 Lund, Sweden, 2010. `http://www.eit.lth.se`.

[10] M. Gustafsson, M. Cismasu, and B. L. G. Jonsson. Physical bounds and optimal currents on antennas. Technical Report LUTEDX/(TEAT-7210)/1–22/(2011), Lund University, Department of Electrical and Information Technology, P.O. Box 118, S-221 00 Lund, Sweden, 2011.

[11] M. Gustafsson and S. Nordebo. Bandwidth, Q factor, and resonance models of antennas. *Progress in Electromagnetics Research*, **62**, 1–20, 2006.

[12] J. D. Jackson. *Classical Electrodynamics*. John Wiley & Sons, New York, third edition, 1999.

[13] B. L. G. Jonsson and M. Gustafsson. Limitations on the effective area and bandwidth product for array antennas. In *Proc. URSI Int Electromagnetic Theory (EMTS) Symp*, pages 711–714, 2010.

[14] R. E. Kleinman and T. B. A. Senior. Rayleigh scattering. In V. V. Varadan and V. K. Varadan, editors, *Low and high frequency asymptotics*, volume 2 of *Handbook on Acoustic, Electromagnetic and Elastic Wave Scattering*, chapter 1, pages 1–70. Elsevier Science Publishers, Amsterdam, 1986.

[15] M. Mitrea. Sharp Hodge decompositions, Maxwell's equations, and vector Poisson problems on nonsmooth, three-dimensional Riemannian manifolds. *Duke Mathematical Journal*, **125**(3), 467–547, 2004.

[16] G. Strang. *Introduction to applied mathematics*. Wellesley-Cambridge Press, Box 157, Wellesley MA 02181, 1986.

[17] H. R. Stuart. Eigenmode analysis of a two element segmented capped monopole antenna. *IEEE Trans. Antennas Propagat.*, **57**(10), 2980–2988, 2009.

[18] H. L. Thal. New Radiation Q Limits for Spherical Wire Antennas. *IEEE Trans. Antennas Propagat.*, **54**(10), 2757–2763, October 2006.

[19] H. Thal. Gain and Q Bounds for Coupled TM-TE Modes. *IEEE Trans. Antennas Propagat.*, **57**(7), 1879–1885, July 2009.

[20] J. G. Van Bladel. *Electromagnetic Fields*. IEEE Press, Piscataway, NJ, second edition, 2007.

[21] G. A. E. Vandenbosch. Reactive energies, impedance, and Q factor of radiating structures. *IEEE Trans. Antennas Propagat.*, **58**(4), 1112–1127, 2010.

[22] G. A. E. Vandenbosch. Simple procedure to derive lower bounds for radiation Q of electrically small devices of arbitrary topology. *IEEE Trans. Antennas Propagat.*, **59**(6), 2217–2225, 2011.

[23] J. Volakis, C. C. Chen, and K. Fujimoto. *Small Antennas: Miniaturization Techniques & Applications*. McGraw-Hill, New York, 2010.

[24] A. D. Yaghjian. Internal energy, Q-energy, Poynting's theorem, and the stress dyadic in dispersive material. *IEEE Trans. Antennas Propagat.*, **55**(6), 1495–1505, 2007.

[25] A. D. Yaghjian and H. R. Stuart. Lower bounds on the Q of electrically small dipole antennas. *IEEE Trans. Antennas Propagat.*, **58**(10), 3114–3121, 2010.

[26] A. D. Yaghjian and S. R. Best. Impedance, bandwidth, and Q of antennas. *IEEE Trans. Antennas Propagat.*, **53**(4), 1298–1324, 2005.

Absorption Efficiency and Physical Bounds on Antennas

Mats Gustafsson, Marius Cismasu and Sven Nordebo

Paper V

Abstract

The all spectrum absorption efficiency appears in the physical bounds on antennas expressed in the polarizability dyadics. Here, it is shown that this generalized absorption efficiency is close to $1/2$ for small idealized dipole antennas and for antennas with a dominant resonance in their absorption. Also, the usefulness of this parameter is analyzed for estimation of antenna performance. The results are illustrated with numerical data for several antennas.

1 Introduction

A new set of physical bounds on antennas was introduced in [4–7, 16]. These bounds relate the performance of the antenna to the electro- and magneto-static polarizability dyadics of a circumscribing geometry. This generalizes the classical bounds by Chu [3] for spherical geometries to geometries of arbitrary shape. The new bounds are valid for lossless and linearly polarized [4, 6, 7, 16] and elliptically polarized [5] antennas. Moreover, the approach can be used to estimate the performances of many small antennas if the polarizabilities of the antennas are used instead of the circumscribing geometries [4, 7, 16].

The only parameter in the bound that depends on the dynamic properties of the antenna is the generalized (or all spectrum) absorption efficiency, η. This is the generalization of the frequency dependent absorption efficiency analyzed in [1] given by integration of the absorbed and total power, independently, over all wavelengths.

In [4, 6, 7, 16], it is demonstrated that η is close to $1/2$ for many small antennas that are connected to a frequency independent resistive load and matched at their first resonance. This is motivated by the minimum scattering property that small matched antennas often possess, *i.e.*, they scatter as much power as they absorb at the resonance frequency giving an absorption efficiency of $1/2$ at the resonance frequency [1, 12]. Here, it is shown that small idealized dipole antennas with a dominant first single resonance have an all spectrum absorption efficiency $\eta \lesssim 1/2$. The region around the resonance is minimum scattering but the contributions from regions away from the resonance scatter slightly more power than is absorbed giving a generalized (all spectrum) absorption efficiency close to but less than $1/2$.

Minimum scattering is a property that many non electrically small resonant antennas also possess. Numerical simulation results of common antennas, both electrically small and not small, verify the theoretical results.

2 Absorption efficiency

The physical bounds analyzed in [4, 6, 7, 16] are derived for single port, linearly polarized, reciprocal, and lossless antennas with the reflection coefficient $\Gamma(k)$

and the directivity $D(k; \hat{\boldsymbol{k}}, \hat{\boldsymbol{e}})$, where k denotes the free space wave number, $\hat{\boldsymbol{k}}$ the direction, and $\hat{\boldsymbol{e}}$ the electric polarization. The forward scattering sum rule [6] gives the antenna identity

$$\int_0^\infty \frac{(1 - |\Gamma(k)|^2) D(k; \hat{\boldsymbol{k}}, \hat{\boldsymbol{e}})}{k^4} \, \mathrm{d}k = \frac{\eta}{2} \left(\hat{\boldsymbol{e}} \cdot \boldsymbol{\gamma}_\mathrm{e} \cdot \hat{\boldsymbol{e}} + (\hat{\boldsymbol{k}} \times \hat{\boldsymbol{e}}) \cdot \boldsymbol{\gamma}_\mathrm{m} \cdot (\hat{\boldsymbol{k}} \times \hat{\boldsymbol{e}}) \right), \quad (2.1)$$

where $\boldsymbol{\gamma}_\mathrm{e}$ and $\boldsymbol{\gamma}_\mathrm{m}$ are the electro- and magneto-static polarizability dyadics, respectively. The integral (2.1) is bounded in various ways to produce bounds for different applications, *e.g.*, resonant and constant partial-realized gain in [4, 6, 7] and ultra-wide band cases in [16]. The resonant case is applicable for antennas with a dominant first single resonance [7]. It is given by

$$\frac{D(k; \hat{\boldsymbol{k}}, \hat{\boldsymbol{e}})}{Q} \leqslant \frac{\eta k_0^3}{2\pi} \left(\hat{\boldsymbol{e}} \cdot \boldsymbol{\gamma}_\mathrm{e} \cdot \hat{\boldsymbol{e}} + (\hat{\boldsymbol{k}} \times \hat{\boldsymbol{e}}) \cdot \boldsymbol{\gamma}_\mathrm{m} \cdot (\hat{\boldsymbol{k}} \times \hat{\boldsymbol{e}}) \right), \quad (2.2)$$

where k_0 is the resonance wave number and Q denotes the Q-factor at the resonance, *i.e.*, it has the half-power fractional bandwidth $B \approx 2/Q$.

The polarizability dyadics in the right-hand sides of (2.1) and (2.2) are easily determined for the antenna or, as an upper bound, for an arbitrary circumscribing geometry[1] by the solution of the corresponding electro- and magneto-static equations [4, 6, 7, 16]. This leaves the generalized absorption efficiency, η, as the only quantity in the right-hand sides of (2.1) and (2.2) that depends on the dynamic properties of the antenna. It is an all spectrum measure of the absorption and scattering properties of the object, that is defined by

$$\eta = \frac{\int_0^\infty \frac{\sigma_\mathrm{a}(k)}{k^2} \, \mathrm{d}k}{\int_0^\infty \frac{\sigma_\mathrm{ext}(k)}{k^2} \, \mathrm{d}k} = \frac{\int_0^\infty \sigma_\mathrm{a}(2\pi/\lambda) \, \mathrm{d}\lambda}{\int_0^\infty \sigma_\mathrm{ext}(2\pi/\lambda) \, \mathrm{d}\lambda}, \quad (2.3)$$

where $\sigma_\mathrm{ext} = \sigma_\mathrm{a} + \sigma_\mathrm{s}$, σ_a, and σ_s denote the extinction, absorption, and scattering cross sections, respectively and $\lambda = 2\pi/k$ is the wavelength. It is clear that $0 \leqslant \eta < 1$ for all objects as $\sigma_\mathrm{a} \geqslant 0$ and $\sigma_\mathrm{s} \geqslant 0$. In [4, 7], it is observed that $\eta \approx 1/2$ for many small antennas that are matched at a dominant first resonance k_0. This is partly explained by the fact that the absorption efficiency $\sigma_\mathrm{a}(k_0)/\sigma_\mathrm{ext}(k_0) = 1/2$ for minimum scattering antennas, *i.e.*, small single mode antennas absorb and scatter the same amount of power at the resonance frequency [1, 12]. The weighting factor, k^{-2}, in (2.3) emphasizes the dynamics of the antenna for low wave numbers. Thus, the lower the resonance frequency, the closer η is to $1/2$ as the resonance region will dominate the integrals. As a consequence, the theory derived here is useful if the analyzed resonance has the lowest frequency. The contributions to η in (2.3) away from the resonance are small due to the fact

---

[1]http://www.mathworks.fr/matlabcentral/fileexchange/26806-antennaq

that scattering dominates the behavior of the antenna in the regions where the mismatch is high.

Here, the case with an idealized lossless antenna that radiates an electric dipole mode is considered to explicitly determine η and illustrate how $\sigma_{\text{ext}}(k)$ and $\sigma_{\text{a}}(k)$ depend on the wave number around the resonance. A spherical dipole mode at the radius a has the impedance [3] $Z_{\text{TM}} = 1/(\text{j}\omega C) + \text{j}\omega L/(1 + \text{j}\omega L/\eta_0)$, where $L = \mu_0 a$, $C = \epsilon_0 a$, $\omega = kc_0$, the time convention $\text{e}^{\text{j}\omega t}$ is used, and ϵ_0, μ_0, c_0, and η_0 denote the free space permittivity, permeability, speed of light, and impedance, respectively. The impedance is modified by the antenna. We consider an antenna with the input impedance obtained from the impedance of the dipole mode, Z_{TM}, tuned to be resonant at $\omega = \omega_0$ with a lumped inductance L_1, i.e.,

$$Z(\omega) = \text{j}\omega L_1 + \frac{1}{\text{j}\omega C} + \frac{\text{j}\omega L}{1 + \text{j}\omega L/R_1}. \tag{2.4}$$

The inductance L_1 is given by $L_1 = 1/(\omega_0^2 C) - L/(1 + \omega_0^2 L^2/\eta_0^2)$, and the radiation resistance at the resonance frequency is $R_0 = Z(\omega_0) = \omega_0^2 L^2 R_1/(R_1^2 + \omega_0^2 L^2)$, and $R_1 = \eta_0$, $L = \mu_0 a$, and $C = \epsilon_0 a$ in the idealized dipole case. The corresponding Q-factor at $\omega = \omega_0$ is determined to $Q = 1/(C^2 L R_1 \omega_0^3) + R_1/(L\omega_0)$ and the reflection coefficient, $\Gamma(\omega) = (Z(\omega) - R_0)/(Z(\omega) + R_0)$, has a single resonance with $\Gamma(\omega_0) = 0$, see Fig. 1. The absorption cross section (or effective antenna aperture) for lossless antennas is given by [15]

$$\sigma_{\text{a}}(k) = \frac{D(k)(1 - |\Gamma(kc_0)|^2)\pi}{k^2}, \tag{2.5}$$

where $D(k) = 3/2$ in the horizontal plane for the considered dipole mode.

Evaluation of η in (2.3) requires a model of the extinction cross section, $\sigma_{\text{ext}}(k)$, that is consistent with (2.4). Consider a single port antenna with incoming signal u and outgoing signal v. The electromagnetic field is expanded in incoming and outgoing spherical modes with coefficients $\boldsymbol{a}$ and $\boldsymbol{b}$, respectively. This gives the scattering matrix [11]

$$\begin{pmatrix} \Gamma & \boldsymbol{R} \\ \boldsymbol{T} & \mathbf{S} \end{pmatrix} \begin{pmatrix} u \\ \boldsymbol{a} \end{pmatrix} = \begin{pmatrix} v \\ \boldsymbol{b} \end{pmatrix}, \tag{2.6}$$

where Γ is the reflection coefficient, $\boldsymbol{R}$ is an $1 \times \infty$ matrix with elements R_n, $\boldsymbol{T}$ is an $\infty \times 1$ matrix with elements T_n, and $\mathbf{S}$ is an $\infty \times \infty$ matrix with elements S_{mn}.

For simplicity, order the modes such that the idealized dipole antenna radiates the first mode, i.e., $R_n = T_n = 0$ for $n > 1$. Conservation of energy shows that the amplitudes of the reflection coefficient and the scattering coefficient, S_{11}, are identical in this case, i.e.,

$$|\Gamma(kc_0)| = |S_{11}(k)| \tag{2.7}$$

for $k \in \mathbb{R}$. Moreover, the scattering matrix is non-causal, i.e., it increases as $\text{e}^{2\text{j}ka}$ as $k \to \infty$ with $|\arg(\text{j}k)| < \pi/2 - \alpha$, for some $\alpha > 0$ where a denotes
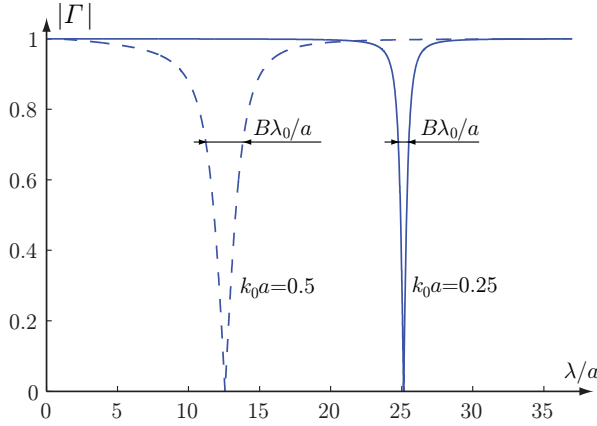
Figure 1: The reflection coefficient of the idealized dipole antenna (2.4) for $k_0 a = 1/2$ and $k_0 a = 1/4$ with $C = \epsilon_0 a$, $L = \mu_0 a$ and $R_1 = \eta_0$ as function of the normalized wavelength $\lambda/a = 2\pi c_0/(\omega a)$.

the radius of the smallest circumscribing sphere, see [9, 14]. As the amplitude of S_{11} is determined by the reflection coefficient (2.7) they can only differ by a function that has unit magnitude for $k \in \mathbb{R}$. Using rational functions, *i.e.*, Blaschke products [14], gives the model

$$S_{11}(k) = \mathrm{e}^{2\mathrm{j}ka} \frac{Z(kc_0) - R_0}{Z(kc_0) + R_0} \prod_n \frac{k_n - k}{k_n^* - k}, \tag{2.8}$$

where k_n denote the zeros of S_{11} in $\mathrm{Re}\{\mathrm{j}k\} > 0$.

The extinction cross section is often expressed in the transition matrix. It is related to the S-matrix in (2.6), **S**, via $\mathcal{T}_{mn} = (S_{mn} - 1)/2$. Consider an idealized dipole antenna that is resonant for $k_0 a \ll 1$. The scattering from higher order modes is negligible for $k_0 a \ll 1$ so the extinction cross section is well approximated with the dipole mode in this region. The extinction cross section from the dipole mode is hence approximated by

$$\sigma_{\mathrm{ext}}(k) \approx -\frac{6\pi \, \mathrm{Re}\,\{\mathcal{T}_{11}(k)\}}{k^2} \quad \text{and} \quad \sigma_{\mathrm{s}}(k) \approx \frac{6\pi |\mathcal{T}_{11}(k)|^2}{k^2}, \tag{2.9}$$

where $\mathcal{T}_{11}$ denotes the diagonal dipole element of the transition matrix [14]. Consider the simplest possible case with a single zero k_1. The value of k_1 is determined by (2.8) and (2.9) inserted into the low-frequency expansions [13] $\sigma_{\mathrm{ext}}(k) = \mathcal{O}(k^2)$ and $\sigma_{\mathrm{s}}(k) = \mathcal{O}(k^4)$ as $k \to 0$. This shows that $k_1 = \mathrm{j}/(a - CR_0 c_0)$, giving the model

$$S_{11}(k) = \mathrm{e}^{2\mathrm{j}ka} \frac{Z(kc_0) - R_0}{Z(kc_0) + R_0} \frac{1 - \mathrm{j}k(a - CR_0 c_0)}{1 + \mathrm{j}k(a - CR_0 c_0)}. \tag{2.10}$$
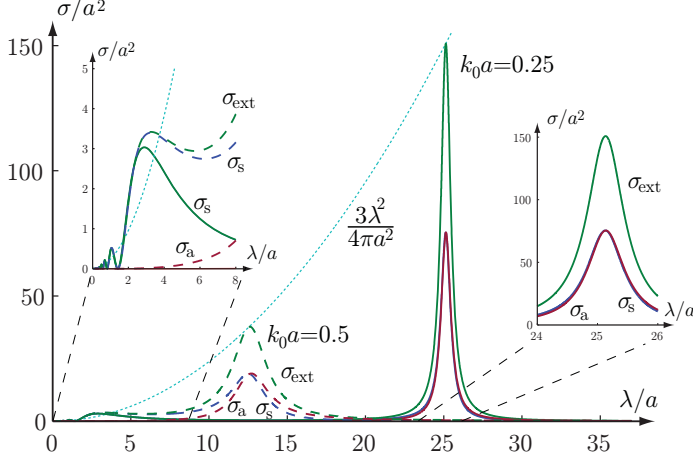
Figure 2: The extinction, σ_{ext}, absorption, σ_{a}, and scattering, σ_{s}, cross sections for the idealized dipole antenna (2.4), depicted in Fig. 1, and (2.10) as function of the normalized wavelength $\lambda/a = 2\pi/(ka)$.

The cross sections σ_{ext}, σ_{a}, and σ_{s} are depicted in Fig. 2 for the same cases as in Fig. 1. It is observed that the areas under the curves are concentrated to the resonances and that $\sigma_{\text{a}}(k) \approx \sigma_{\text{s}}(k)$ around the resonances for $k_0 a = 0.25$. For minimum scattering, $\operatorname{Re}\{\mathcal{T}_{11}(k)\} = -1/2$ in (2.9), we obtain the envelope $\sigma_{\text{ext}}(k)/a^2 \approx 3\pi/k^2a^2 = 3\lambda^2/4\pi a^2$, also plotted in Fig. 2. The more dominant a resonance, the closer the obtained value of the extinction cross section is to this envelope at the resonance frequency.

The generalized (all-spectrum) absorption efficiency (2.3) for the idealized dipole is finally determined by

$$\eta = \frac{\displaystyle\int_0^\infty \frac{(1-|\Gamma(k)|^2)D\pi}{k^4}\,\mathrm{d}k}{\displaystyle\int_0^\infty \frac{\sigma_{\text{ext}}(k)}{k^2}\,\mathrm{d}k} \approx \frac{\displaystyle\int_0^\infty \frac{1-|\Gamma(k)|^2}{k^4}\,\mathrm{d}k}{-4\displaystyle\int_0^\infty \frac{\operatorname{Re}\{\mathcal{T}_{11}(k)\}}{k^4}\,\mathrm{d}k}. \tag{2.11}$$

The generalized absorption efficiency η is evaluated for the idealized dipole model (2.4) and (2.10) as well as various other parameter values on C, L, and R_1 in Fig. 3. It is observed that $\eta \lesssim 1/2$ for $k_0 a \ll 1$. The deviation from $1/2$ is due to the region with small σ_{s} but negligible σ_{a} for $\lambda/a < 8$ as seen in Fig. 2.

The particular impedance (2.4) is not crucial for this result. It is sufficient that the contributions to the integrals in (2.3) are dominated by the region around the resonance k_0 and that σ_{a} and σ_{ext} have similar bandwidths and shapes. It is common to assume antennas with a single resonance structure [8] to relate the bandwidth with the antenna Q. Similarly, assume that the transition matrix element $\mathcal{T}_{11}(k)$ has a single resonance at k_0 and is minimum scattering, *i.e.*,
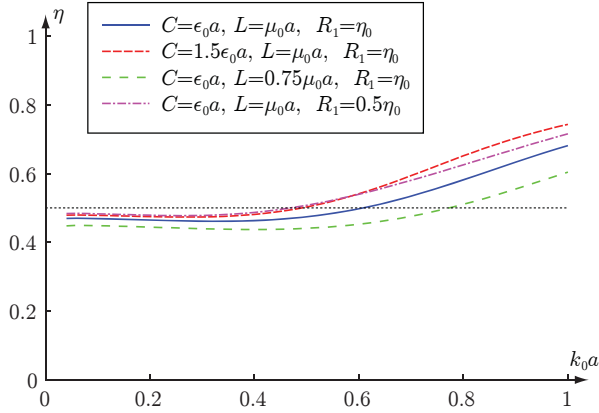
Figure 3: The generalized absorption efficiency for the idealized dipole antenna (2.4) and (2.10) and various values of $C, L,$ and R_1 as function of the normalized resonance wave number $k_0 a$.

$S_{11}(k_0) = 0$ implying $\mathcal{T}_{11}(k_0) = -1/2$. The resonance model has complex valued poles at $k \approx \pm k_0$ and the shape of the classical Lorentz or resonance circuit [8, 14] around the resonance, *i.e.*,

$$\mathcal{T}_{11}(k) = \frac{-\dfrac{1}{2}}{1 + \dfrac{\mathrm{j}}{\nu}\left(\dfrac{k}{k_0} - \dfrac{k_0}{k}\right)} = \frac{-\dfrac{\mathrm{j}\nu k}{2k_0}}{1 - \dfrac{k^2}{k_0^2} + \dfrac{\mathrm{j}\nu k}{k_0}} \tag{2.12}$$

with $0 < \nu \ll 1$. It satisfies

$$-\operatorname{Re}\{\mathcal{T}_{11}(k)\} = \frac{1/2}{1 + \dfrac{1}{\nu^2}\left(\dfrac{k}{k_0} - \dfrac{k_0}{k}\right)^2} = 2|\mathcal{T}_{11}(k)|^2 \tag{2.13}$$

for all $k \in \mathbb{R}$ showing that $\sigma_{\mathrm{ext}}(k) = 2\sigma_{\mathrm{s}}(k) = 2\sigma_{\mathrm{a}}(k)$ around the resonance wave number, see the $k_0 a = 1/4$ case in Fig. 2. For antennas with negligible σ_{a} away from the resonance, *e.g.*, the dipole model (2.4), the $\sigma_{\mathrm{ext}} \approx \sigma_{\mathrm{s}}$ contribution to the integral (2.3) away from the resonance gives $\eta \lesssim 1/2$.

3   Numerical Examples

The above theoretical results have been analyzed for a number of geometries by numerical simulations; the numerical results show very good agreement with the theory. For each of the examples the approach was the same; first we started
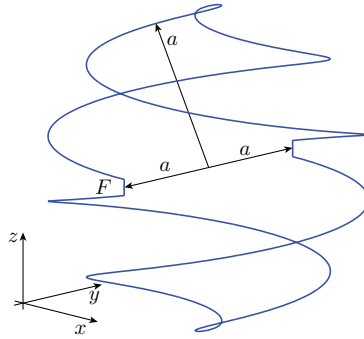
Figure 4: Geometry of the two arm spherical helix with circumscribing sphere radius $a = 62\,\mathrm{mm}$ and wire radius $R_\mathrm{w} = 2\,\mathrm{mm}$.
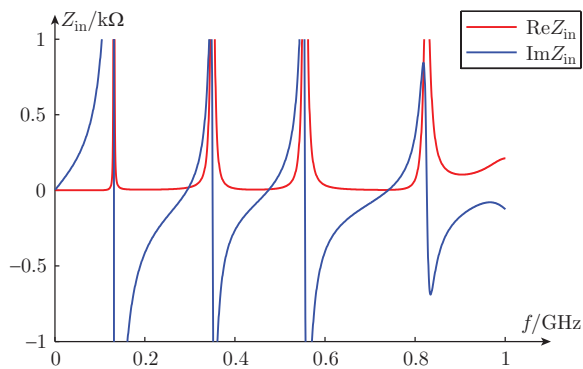
Figure 5: Input impedance of the spherical helix depicted in Fig. 4.
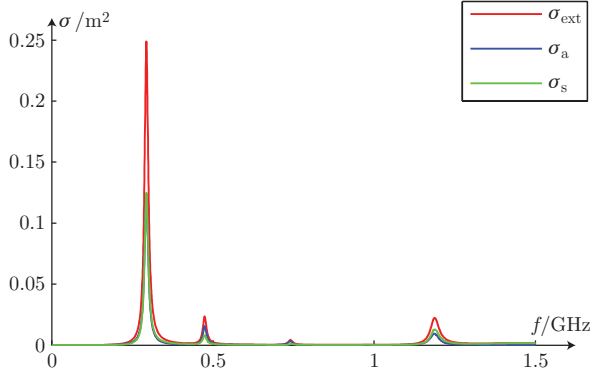
Figure 6: Extinction, absorption and scattering cross sections of the spherical helix depicted in Fig. 4.

with the design and simulation of a radiating structure using the Method of Moments (MoM) simulator in Efield[2]. Then the radiation resistance at the first resonance was used as a load at the feeding point in a forward scattering simulation, performed using the same software. The results of the antenna and scattering simulations have been used to numerically compute the theoretical parameters using Matlab. Note that not all the available digits are presented in the text as the numerical accuracy does not justify them. However the formulas are computed without truncation.

3.1   Folded Spherical Helix $-$ $D = 1.5$, $k_0 a = 0.38$

We first describe the results for the folded spherical helix [2] depicted in Fig. 4. It comprises a closed loop of perfectly electric conducting wire of radius $R_{\mathrm{w}} = 2\,\mathrm{mm}$ that is folded on the surface of a sphere of radius $58\,\mathrm{mm}$ thus obtaining a structure with the radius of the smallest circumscribing sphere $a = 62\,\mathrm{mm}$. The structure has two arms of equal length (approximately $l_{\mathrm{a}} = 646\,\mathrm{mm}$) symmetric with respect to the z axis.

The first step in the analysis is to simulate this structure with Efield. The antenna parameters are determined with an ideal voltage source connected at point F (see Fig. 4). The resulting input impedance is plotted in Fig. 5. The first interesting resonance from a practical point of view appears around $294\,\mathrm{MHz}$ with a radiation resistance of $17\,\Omega$. It is this resonance that is used to illustrate the physical bounds in [4, 6, 7, 16]. At this frequency the antenna radiates a z dipole type pattern. First we compute the $D/(Q k_0^3 a^3)$ value using the simulation data from Efield and the method proposed in [8, 18] to approximate the Q factor. The computed values $D = 1.5$, $Q = 43$ and $k_0 a = 0.38$ result in the quotient

---
[2]www.efieldsolutions.com
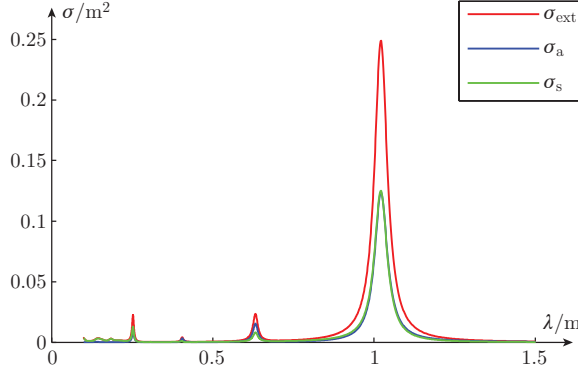
Figure 7: Extinction, absorption and scattering cross sections of the spherical helix depicted in Fig. 4 as function of wavelength, $\lambda = 2\pi/k = c_0/f$.

$D/(Qk_0^3 a^3) = 0.63$.

The second step is to evaluate the right hand side in (2.2). Here, the polarizability dyadics reduce to the high contrast polarizability dyadic of the perfect electric conductor which is computed using a MoM algorithm (see *e.g.*, [4]) that solves the electrostatic problem associated with the wire geometry. With $\hat{e} = \hat{z}$ and only high contrast electric material present $\hat{e} \cdot \boldsymbol{\gamma}_e \cdot \hat{e} + (\hat{k} \times \hat{e}) \cdot \boldsymbol{\gamma}_m \cdot (\hat{k} \times \hat{e})$ evaluates to:

$$\hat{z} \cdot \boldsymbol{\gamma}_\infty \cdot \hat{z} = 2 \cdot 10^{-3}\,\mathrm{m}^3.$$

The generalized absorption efficiency is computed from the Efield simulation data with (2.3) and the definitions of absorption and extinction cross sections from [7, 17]. After an integration of 5999 absorption and extinction cross sections samples taken equidistantly between $1\,\mathrm{MHz}$ and $3\,\mathrm{GHz}$ (see Fig. 6) we obtain $\eta \approx 0.51$ and write:

$$\frac{D}{Qk_0^3 a^3} \approx 0.63 \leqslant 0.67 \approx \frac{\eta}{2\pi a^3} \left(\hat{z} \cdot \boldsymbol{\gamma}_\infty \cdot \hat{z} \right).$$

This is a true relation showing that the antenna performs close to the D/Q bound of the wire structure.

Moreover, the integrated extinction cross section is related to the polarizability of the structure, as stated in [17] *i.e.*,

$$\frac{2}{\pi} \int_0^\infty \frac{\sigma_{\mathrm{ext}}(k)}{k^2}\,\mathrm{d}k = \frac{1}{\pi^2} \int_0^\infty \sigma_{\mathrm{ext}}(\lambda)\,\mathrm{d}\lambda \approx 1.99 \cdot 10^{-3}\,\mathrm{m}^3$$

which is approximately 1% away from the polarizability determined from the MoM simulation. This deviation can be attributed to the high frequecies (low wavelengths) which are missing in Fig. 7. The cross sections should show one dominant resonance and asymptotically tend to 0 for low frequencies.
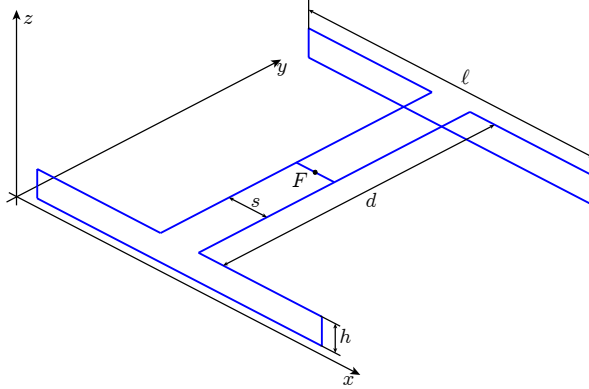
Figure 8: Two element array of folded dipoles with $\ell = 492.9\,\text{mm}$ and $d = 470\,\text{mm}$.

The physical bounds in (2.2) create a link between the dynamic properties of the radiating structure and its static properties described by the electric and magnetic polarizability dyadics. Because many common antennas have a generalized absorption efficiency of approximately $1/2$ obtaining the bounds for an antenna reduces to a static problem of computing the polarizability dyadics for the geometry, which is easily solved using a Method of Moments algorithm.

It is very important to distinguish the geometry of the radiating structure from its smallest circumscribing sphere. The antenna can be optimized in the limit given by its own polarizability, *e.g.*, the smallest circumscribing sphere of the helix in Fig. 4 has the radius $a = 62\,\text{mm}$, which gives $\hat{\boldsymbol{z}} \cdot \boldsymbol{\gamma}_\infty \cdot \hat{\boldsymbol{z}} = 4\pi a^3 \approx 3 \cdot 10^{-3}\,\text{m}^3$ thus the maximum attainable value for the D/Q quotient is: $D/(Qk_0^3 a^3) \leqslant 1$, whereas the wire structure simulated here has a maximum attainable value $D/(Qk_0^3 a^3) \leqslant 0.67$. The presence of the $(k_0 a)^3$ term allows radiating structures to be directly compared even though they do not have the same size. It can be stated that the wire structure of the helix in Fig. 4 can only reach 67% of the best attainable performance of an antenna circumscribed by a sphere with equal radius. Hence, it is neccesary to use a structure with high polarizability to improve the performance, *e.g.*, the polarizability of the spherical helix increases with the number of arms and with the wire radius.

3.2   Folded Dipole Array − $D = 2.6$, $k_0 a = 1.7$

The second considered structure is a folded dipole array [10]. The dimensions in Fig. 8 are the following: $\ell = 492.9\,\text{mm}$, $d = 470\,\text{mm}$, $h = 40\,\text{mm}$ and $s = 65.8\,\text{mm}$. The structure is assumed to be fed at point F with an ideal voltage source. All wires have a radius of $R_\text{w} = 4\,\text{mm}$ thus simulating one possible realization of a simple and common array design using the same type of conductor for all the elements. The smallest circumscribing sphere has the radius $a = 347\,\text{mm}$.

First we simulate the structure in transmission in order to obtain the imped-
ance behavior in the frequency range of interest, see Fig. 9. The first resonance
with practical relevance is close to 233 MHz and, at this frequency the antenna
has an input impedance of 59 Ω. We shall illustrate the bounds using the char-
acteristics of the structure at this frequency. The far field radiation pattern at
this resonance consists of two linearly polarized ($\hat{\boldsymbol{x}}$-direction) pencil beams in the
broad sides, with a maximum directivity $D = 2.6$. The quality factor of this res-
onance is $Q = 4.2$ and with $k_0 a = 1.7$ we obtain the quotient $D/(Qk_0^3 a^3) = 0.13$.

The high contrast polarizability for $\hat{\boldsymbol{e}} = \hat{\boldsymbol{x}}$ polarization has the value $\gamma_{\infty,11} =$
$67.4 \cdot 10^{-3}\,\mathrm{m}^3$. We note here that the structure is also highly polarizable on the
$\hat{\boldsymbol{y}}$-direction but the $\hat{\boldsymbol{y}}$-polarization does not contribute to the radiation because
of the choice of feeding.

We now turn to the analysis of the cross sections and use 5999 absorption and
extinction cross section samples from equidistantly spaced frequencies between
1 MHz and 3 GHz. The first and dominating resonance is shown in Fig. 10. The
array has a two band behavior; in either of the two bands it approximately absorbs
as much energy as it scatters. Besides these two resonances there is another
scattering resonance which contributes to the generalized absorption efficiency.
By comparing Fig. 6 with Fig. 10 we expect to have differences between the two
generalized absorption efficiencies but in fact $\eta \approx 0.48$. The reason for the small
deviation is the presence of the second resonance very close to the first one, and
with comparable values of the radiation resistance.

Gathering the results, we rewrite (2.2) in numbers as: $0.13 \leqslant 0.13$ thus
making this array a structure that is close to the optimal D/Q performance of
the wire structure. The perfect matching is explained by the deviation of the
structure from the assumed models for the Q-factor ($Q \gg 1$) and the first single
and dominant resonance. Compared with a smallest circumscribing sphere, the
array only reaches 13% of its D/Q performance. For evaluating the reliability
of the generalized absorption efficiency we integrate the extinction cross section
over the wavelength and obtain the value $66.8 \cdot 10^{-3}\,\mathrm{m}^3$ which is less than 1%
from the previous $\gamma_{\infty,11} = 67.4 \cdot 10^{-3}\,\mathrm{m}^3$; so the frequency interval is well chosen
as to not significantly deviate the resulted η from its correct value.

3.3   Other Structures

A number of other structures have been analyzed and the results are gathered
in Table 1. The first eight rows in the table correspond to planar geometries
circumscribed by different $l_1 \times l_2$ rectangles with l_1/l_2 respectively equal to: 500,
100, 25, 9, 3.6, 2, 1 and 0.5. The polarization is always directed along l_1. There
are two meander type antennas which differ by their aspect ratios and feeding
structure. The ninth and tenth rows correspond to the structures described
respectively in 3.1 and 3.2.

The eleventh and twelfth rows correspond to four element arrays fed in phase
to obtain two broadside pencil shaped lobes. For the first one the elements are
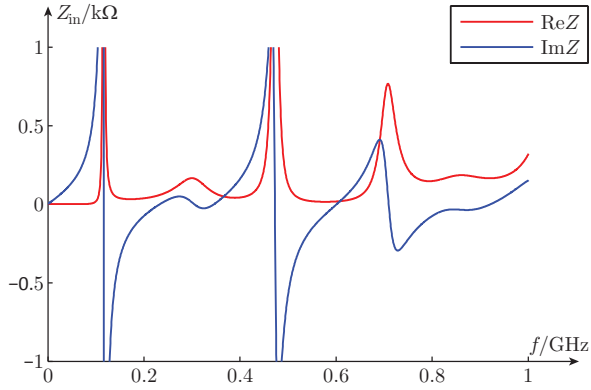
Figure 9: Input impedance of the array depicted in Fig. 8.
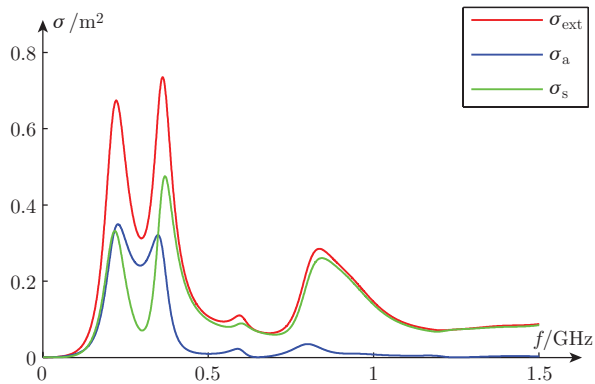
Figure 10: Extinction, absorption and scattering cross sections of the array depicted in Fig. 8.

represented by simple dipoles of length $\ell = 500\,\mathrm{mm}$ spaced at $d = 500\,\mathrm{mm}$ and wire radius $R_w = 1\,\mathrm{mm}$ and for the second the elements are folded dipoles with length $\ell = 502\,\mathrm{mm}$ and height $h = 6\,\mathrm{mm}$ spaced at $d = 470\,\mathrm{mm}$ and wire radius $R_w = 2\,\mathrm{mm}$. Both structures are fed through transmission lines made from the same wire as the radiating elements.

The last line corresponds to a two element array, each element being a Yagi antenna with a reflector ($l_r = 510\,\mathrm{mm}$), driven element ($l_f = 500\,\mathrm{mm}$) and director ($l_d = 420\,\mathrm{mm}$) spaced at $l_s = 200\,\mathrm{mm}$. The distance between the elements in the array is $d = 470\,\mathrm{mm}$ and the wire radius is $R_w = 5\,\mathrm{mm}$. Feeding is realized with a transmission line made from the same wire as the elements.

4 Conclusions

We demonstrate that $\eta \lesssim 1/2$ for small, $k_0 a \ll 1$, idealized dipole antennas and for minimum scattering antennas with a dominant first single resonance. As observed in [4, 7] this is also valid for several antennas that are of the order $k_0 a \approx 1$. Here, it is important to realize that the identity (2.1) is not restricted to electrically small antennas and that η in general cannot be replaced by $1/2$. Many antennas, *e.g.*, Yagi-Uda and reflector antennas have $\eta \ll 1/2$ and some, *e.g.*, the spiral antenna in [16], have $\eta > 1/2$.

Acknowledgments

References

[1] J. B. Andersen and A. Frandsen. Absorption efficiency of receiving antennas. *IEEE Trans. Antennas Propagat.*, **53**(9), 2843–2849, 2005.

[2] S. R. Best. The radiation properties of electrically small folded spherical helix antennas. *IEEE Trans. Antennas Propagat.*, **52**(4), 953–960, 2004.

[3] L. J. Chu. Physical Limitations of Omnidirectional Antennas. *J. Appl. Phys.*, **19**, 1163–1175, 1948.

[4] A. Derneryd, M. Gustafsson, G. Kristensson, and C. Sohl. Application of gain-bandwidth bounds on loaded dipoles. *IET Microwaves, Antennas & Propagation*, **3**(6), 959–966, 2009.

	D	Q	k_0a	$\frac{D}{Qk_0^3a^3}$	$\frac{\eta\gamma}{2\pi a^3}$	η	$\frac{\gamma}{a^3}$
	1.64	8	1.51	0.056	0.058	0.51	0.705
	1.64	6	1.49	0.078	0.079	0.52	0.962
	1.63	6	1.43	0.088	0.090	0.52	1.087
	1.64	3	1.44	0.173	0.155	0.50	1.944
	1.55	18	0.72	0.231	0.244	0.52	2.972
	1.54	57	0.48	0.246	0.287	0.54	3.309
	2.23	5	1.31	0.211	0.200	0.52	2.429
	3.04	5	1.92	0.095	0.089	0.51	1.085
	1.50	43	0.38	0.631	0.728	0.51	9.339
	2.63	4	1.69	0.130	0.130	0.48	1.698
	6.15	20	3.84	0.005	0.008	0.42	0.116
	6.30	7	4.08	0.013	0.013	0.41	0.194
	3.21	17	1.72	0.036	0.042	0.14	1.897

Table 1: Numerical results of the antennas in Sec. 3.3.

[5] M. Gustafsson and C. Sohl. New physical bounds on elliptically polarized antennas. In *Proceedings of the Third European Conference on Antennas and Propagation*, pages 400–402, Berlin, Germany, March 23–27 2009. The Institution of Engineering and Technology.

[6] M. Gustafsson, C. Sohl, and G. Kristensson. Physical limitations on antennas of arbitrary shape. *Proc. R. Soc. A*, **463**, 2589–2607, 2007.

[7] M. Gustafsson, C. Sohl, and G. Kristensson. Illustrations of new physical bounds on linearly polarized antennas. *IEEE Trans. Antennas Propagat.*, **57**(5), 1319–1327, May 2009.

[8] M. Gustafsson and S. Nordebo. Bandwidth, Q factor, and resonance models of antennas. *Progress in Electromagnetics Research*, **62**, 1–20, 2006.

[9] M. Gustafsson, C. Sohl, and S. Nordebo. Physical bounds on the antenna scattering matrix. In *IEEE International Symposium on Antennas and Propagation*. IEEE-AP, San Diego, July 5–12 2008.

[10] G. Hall et al. *The ARRL Antenna Book*. American Radio Relay League, 1984.

[11] J. E. Hansen, editor. *Spherical Near-Field Antenna Measurements*. Number 26 in IEE electromagnetic waves series. Peter Peregrinus Ltd., Stevenage, UK, 1988. ISBN: 0-86341-110-X.

[12] W. Kahn and H. Kurss. Minimum-scattering antennas. *IEEE Trans. Antennas Propagat.*, **13**(5), 671–675, 1965.

[13] R. E. Kleinman and T. B. A. Senior. Rayleigh scattering. In V. V. Varadan and V. K. Varadan, editors, *Low and high frequency asymptotics*, volume 2 of *Handbook on Acoustic, Electromagnetic and Elastic Wave Scattering*, chapter 1, pages 1–70. Elsevier Science Publishers, Amsterdam, 1986.

[14] H. M. Nussenzveig. *Causality and dispersion relations*. Academic Press, London, 1972.

[15] S. Silver. *Microwave Antenna Theory and Design*, volume 12 of *Radiation Laboratory Series*. McGraw-Hill, New York, 1949.

[16] C. Sohl and M. Gustafsson. A priori estimates on the partial realized gain of Ultra-Wideband (UWB) antennas. *Quart. J. Mech. Appl. Math.*, **61**(3), 415–430, 2008.

[17] C. Sohl, M. Gustafsson, and G. Kristensson. Physical limitations on broadband scattering by heterogeneous obstacles. *J. Phys. A: Math. Theor.*, **40**, 11165–11182, 2007.

[18] A. D. Yaghjian and S. R. Best. Impedance, bandwidth, and Q of antennas. *IEEE Trans. Antennas Propagat.*, **53**(4), 1298–1324, 2005.